Biofouling and Organic Fouling of Ultrafiltration and Reverse Osmosis Membranes: Quantification by Atomic Force Microscopy

A DISSERTATION SUBMITTED TO THE FACULTY OF UNIVERSITY OF MINNESOTA BY

Sara BinAhmed-Menzies

IN PARTIAL FULFILLMENT OF THE REQUIREMENTS FOR THE DEGREE OF DOCTOR OF PHILOSOPHY

Santiago Romero-Vargas Castrillón

Raymond M. Hozalski

December 2020

Copyright page

Dedication

To my best friend and spouse Khalil.

To Malik Bjorn and his sister to be.

To the blessings called family and friends.

Table of contents

List of tables

List of figures

Chapter 1: Introduction

Water scarcity

Water has always been a limited resource where only 2.5% of water on Earth is fresh[1] and 0.5% of the Earth's water is accessible to humans.[2] Moreover, the distribution of fresh water relative population and geographic areas is not equal. The number of people in water stressed areas is increasing and expected to reach two-thirds of human population by 2025.[3] In addition to increased population and pollution of some available resources[4–6] exacerbating the problem of water shortages, climate change is expected to increase the occurrence of droughts[7] and seawater intrusion.[6,8] Shortages of water supplies directly affects food security since agriculture consumes 70% of human water demand.[1] Kelley *et al*.[9] mention that the drought that Syria has endured between 2007 and 2010 was the worst in record and caused around 1.5 million people to internally migrate from rural agricultural areas to the suburbs of Syria's major cities.

Therefore, the need to supplement the fresh water supply is becoming increasingly important in order to avoid extreme water shortages and accompanying societal and health problems. Unconventional water sources such as brackish water and seawater[3,6] already provide some countries with over 38 billion m^3 of clean water per year.[3] Water recovered from wastewater effluent[10,11] can supplement water resources[12] through indirect use in agricultural and urban irrigation, cooling towers, and recharge of groundwater aquifers.[4]

Alternatives provided by membrane processes

Membrane separation processes provide the tools to produce potable water out of brackish, surface and seawater as well as treat industrial and wastewater effluents.[3,13,14] To enhance removal of pathogens and meet more stringent drinking water and wastewater discharge regulations, more facilities are using membranes processes as an alternative or complementary to conventional water and wastewater treatment.[15]

Microfiltration (MF) and ultrafiltration (UF) membranes are porous that use size exclusion to remove contaminants in water.[1,16] MF removes suspended particles and pathogens such as bacteria and *Giardia*.[16] UF membranes can be used for different applications like surface and wastewater treatment, and pretreatment for reverse osmosis (RO) membranes.[3,13,16] UF membranes are also used in many industries including food processing and dairy, electronics, textile, pharmaceuticals, electrocoat painting, and heavy machinery manufacturing.[17–21]

Reverse osmosis (RO) and forward osmosis (FO) are nonporous membranes that remove almost all ions present in water in addition to small uncharged contaminants (> 100 Da).[1,16] RO membranes use solution-diffusion mechanisms to transport water and solutes through the active layer. [1,16] The different molecules partition at the surface of the active layer, diffuse through its polymer network and then desorb at the other side of the selective layer in the permeate.[16] The solutes are transported at different rates depending on their solubilities and/or diffusivities in the selective layer of the membrane.[16] Reverse osmosis (RO) membranes are used for potable water production from brackish water and seawater in addition to water reclamation from secondary wastewater effluents.[22–24]

Nanofiltration (NF) on the other hand uses both size exclusion and solution–diffusion mechanisms to separate undesired components such as organic matter and toxic metals from the water.[16] NF and RO membranes yield higher removals of organic matter and pathogens especially viruses compared to the more cost effective UF membranes. [15]

Types of membrane fouling

Despite all the advances in the fabrication and modification of membranes, a major problem still affecting the performance of membrane processes is fouling.[6] Fouling is defined as the undesirable deposition of different substances present in the feed on the surface of membranes[3,25] and/or within the membrane pores of MF, UF, and NF membranes[16]. The formation of the fouling layer increases the pressure drop, and consequently the energy[6], required to produce the same permeate flow rate.[26] Additionally, fouling deteriorates the membrane's selectivity and permeability[3,16,26,27] which eventually shortens the membrane's lifetime[6,16,25,26] and adds additional operational as well as maintenance and cleaning costs.[3,6,16,25–27] There are different types of fouling: inorganic (scaling and colloidal), organic, and microbial or biofouling.[16,25–27]

Inorganic fouling is caused by the accumulation of salt deposits, silica and/or colloidal substances.[28,29] When salts such as $CaCO_3$ and $CaSO_4 \cdot 2H_2O$ present in the feed exceed their solubility limit, they precipitate on the surface of the membrane forming a scaling layer.[28,30]

Organic fouling of membranes is caused by both hydrophilic and hydrophobic components of organic matter.[1] Natural waters contain dissolved organic matter (DOM) while dissolved effluent organic matter (EfOM) is a major constituent of secondary effluent in wastewater

treatment plants.[31] EfOM comprises humic substances from the drinking water supply together with microbial products resulting from the biodegradation of human and industrial wastes.[32] Accordingly, feeds in both potable water and water recovery operations contain different molecular weight DOM composed partly or mainly of humic substances.[22,33] Humic acids (HA) and fulvic acids (FA) are the components of humic substances that are soluble at pH > 2, with humin making up the remainder.[32]

Biofouling is defined as the accumulation of microorganisms (bacteria, fungi, algae) on the surface of polymer membranes leading to the formation of a biofilm.[26,34–36] The presence of an organic fouling layer can change the surface properties of the surface of the membrane[37] and act as a conditioning layer that provides nutrients to bacteria and facilitate biofilm formation by promoting bacterial adhesion to the surface.[38,39]

Effect of the properties of the feed solution and membrane interfacial properties on organic fouling and biofouling

The characteristics of the feed solution (pH, ionic strength, temperature, and presence of organic matter and divalent ions especially Ca^{2+}) play a role in membrane fouling.[37,4037,41–44] For example, proteins cause the sharpest flux decline at pH values close to their isoelectric points (IEP).[29] Higher ionic strength or conductivity of the feed solution is expected to increase the fouling rate as electrostatic repulsion is reduced due to compression of the double layer.[19] Jin *et al*.[41] studied the effect of temperature (T = 15, 25, and 35 ºC) on organic fouling of NF and RO membranes using 7.5 mg L^{-1} humic acid and observed that the highest flux decline at 15 ºC while the rate of fouling was similar at 25 ºC and 35 ºC.

Membrane interfacial properties also affect the membrane's susceptibility for fouling.[37] Smoother and more hydrophilic surfaces are less prone to fouling. [1,45–48] The negative surface charge of membranes due to the presence of different functional groups at their surface, such as carboxyl groups on polyamide RO membranes, increases the severity of fouling by Ca^{2+} bridging between the membrane and the foulants.[16]

One common method to mitigate for organic and biofouling is modifying membrane surfaces to alter one or more if its physicochemical properties such as hydrophilicity, charge, and/or roughness to render it more resistant to fouling.[16,49] For example, binding zwitterionic polymer brush layer on the surface of RO membranes reduces organic fouling.[6,16]

Understanding fouling at intermolecular level using atomic force microscopy

Understanding intermolecular interactions between the foulant and the surface of the membrane under different experimental conditions can help predict fouling behavior. AFM is a powerful tool that can provide a deeper understanding of the mechanisms of early stages of adhesion which in turn would help develop membrane antifouling strategies. Depending on the setup, the AFM can quantify cell-cell and cell-substrate interactions (nN and pN range)[38,50–52], and even substrate-single molecule forces[34], to a high precision. Single cell force spectroscopy (SCFS) is an AFM technique where a single bacterial cell is immobilized to the end of a cantilever to measure adhesion forces in a liquid environment between the cell and substratum in the nN and pN range.[50,51] Unique patterns and The

magnitude of adhesion forces and unique patterns in resulting force-distance curves can provide information about the nature and elasticity of the macromolecules (e.g. proteins, and lipopolysaccharides) involved in the adhesion process.[53]

Colloidal probe force spectroscopy using atomic force microscopy (AFM) enables the measurement of interfacial adhesion forces at a nanoscale level between a spherical colloidal probe and a surface in an aqueous medium.[54,55] The foulant is deposited on the colloidal probe via adsorption[31,56] or electrostatic attraction on iron oxide coated colloidal particle[57–59]. Alternatively, a probe with chemical functionality similar to that of foulant is used such as carboxyl modified latex (CML) particles as surrogates to foulants rich in carboxylic functional groups like alginates[25,60,61] and humic acids[62]. Several researchers found that stronger adhesion forces between a colloidal probe and the surface of the membrane correlated with higher fouling propensity.[25,60,62,63]

Transport in RO membranes

Water and salt transport through an RO membrane is generally described by the solution diffusion model.[64] The water flux, J_w (L m^{-2} h^{-1}) through the membrane is calculated using equation (1.1) where A is the pure water permeability coefficient (L m^{-2} h^{-1} bar^{-1}), Δp is the applied trans-membrane hydraulic pressure (bar) and $\Delta\pi$ = trans-membrane osmotic pressure difference (bar).[41,65,66]

$$J_w = A(\Delta p - \Delta\pi) \qquad (1.1)$$

In the presence of salts (multi-component salt solution), the osmotic pressure of each of the feed (π_f) and permeate (π_p) is expressed using equations (1.2)[64,67] and (1.3)[68],

respectively, in order to calculate $\Delta\pi = \pi_f - \pi_p$. R is the ideal gas constant, T is the absolute temperature, and c_i is the concentration of each in feed (mol L^{-1}).

$$\pi_f = RT \sum c_i \quad (1.2)$$

$$\pi_p = \pi_f(1 - X_s) \quad (1.3)$$

X_s is the apparent salt rejection (%) calculated using equation (1.4) where c_f is the salt concentration in feed (mol L^{-1}) and c_p is the salt concentration in permeate (mol L^{-1}).[66]

$$\mathrm{X_s} = 1 - \frac{c_\mathrm{p}}{c_\mathrm{f}} \times 100 \quad (1.4)$$

The accumulation of the rejected salts near the surface of the membrane creates a concentration polarization (*CP*) layer.[67] The concentration of salts in the *CP* layer ($c_\mathrm{f,m}$) is higher than in the feed (c_f).[67] As a result, the intrinsic salt rejection, R_s, is different from X_s and can be calculated as described in equation (1.5).[41,65] Consequently, CP is expressed as in equation (1.6).[69]

$$R_\mathrm{s} = 1 - \frac{c_\mathrm{p}}{c_\mathrm{f,m}} \times 100 \quad (1.5)$$

$$CP = \frac{c_\mathrm{f}}{c_\mathrm{f,m}} = \left(1 - R_\mathrm{s} + R_\mathrm{s} \cdot exp\left(-\frac{J_\mathrm{w}}{k_\mathrm{s}}\right)\right)^{-1} \quad (1.6)$$

The solute mass transfer coefficient, k_s, depends on the Sherwood number (*Sh)*, solute diffusivity (*D*), and the hydraulic diameter of the crossflow chamber (d_H = 2·channel height).[69]

$$Sh = 1.85(ReSc\, d_\mathrm{H}/L)^{0.33} \quad (1.7)$$

$$k_s = \frac{ShD}{d_\mathrm{H}} \quad (1.8)$$

Sc is Schmidt number and *L* is the length of the channel.[69]

The osmotic pressure in the presence of *CP* and resulting water permeability coefficient, *A*, can be calculated using equation (1.9) and (1.10), respectively.[41,65]

$$\Delta\pi = RTc_{\mathrm{f,m}} - RTc_{\mathrm{p}} = RTR_{\mathrm{s}}c_{\mathrm{f,m}} \quad (1.9)$$

$$A = \frac{J_w}{\Delta p - RTR_s c_{f,m}} \quad (1.10)$$

In addition to its effect on water flux, *CP* results in higher trans-membrane osmotic pressure[67] and lower salt rejection[5] due to an increase in the force driving salt transport in the membrane.[67] Equation (1.11) relates the solute permeability coefficient, *B*, to the solute flux through the membrane, J_{s}.[66]

$$J_{\mathrm{s}} = B\Delta c_{\mathrm{s}} = B(c_{\mathrm{f,m}} - c_{\mathrm{p}}) \quad (1.11)$$

Scope of thesis

While there are numerous studies about the effect of different material properties and process conditions on formation of biofilms[71], little is understood about the initial stages of bacterial adhesion (bioadhesion). The goal of this research is to elucidate the mechanisms of initial bacterial adhesion to polymeric membrane surfaces under different environmental conditions and substratum interfacial properties. We employed the single cell force spectroscopy (SCFS) to measure the intermolecular interactions between the surface of polymeric membranes and a single bacterial cell (*P. fluorescens*). Since temperature is a poorly understood parameter in organic fouling, we extended our technique to colloidal probe force spectroscopy in order to measure the effect of temperature on foulant-membrane and foulant-foulant interactions using alginate as a

model foulant. A summary of the chapters and the contributions of each author in the published papers are described below.

The second chapter investigated the effect of UF membrane surface hydrophilicity on initial bacterial adhesion. The effect of membrane-bacterium contact time (0, 2, and 5 seconds) as well as the presence of natural organic matter (NOM; Upper Mississippi River) in solution and as a fouling layer on bioadhesion were also investigated. The results of this part of the research have been published in BinAhmed *et al*.[72] In this work, I developed a single-cell force spectroscopy (SCFS) protocol to include a robust set of steps to immobilize the *P. fluorescens* cell to the end of a tipless cantilever and to confirm that the bacterium was not dislocated or compromised during force measurements by fluorescence microscopy. In addition to surface characterization, I fabricated the polysulfone (PSF) UF membranes and modified them with polydopamine (PDA) to render their surfaces more hydrophilic.[73] I, also, performed the data analysis and prepared of the manuscript.

The second author, Anissa Hasane, was a visiting graduate student from Norwegian University of Science and Technology (NTNU, Norway). During our mentorship, I trained Anissa on the SCFS protocol which she helped refine. Anissa carried part of the SCFS experiments on the PSF and PDA coated membranes at different contact times. She also learned to fabricate the UF membranes and coat them with PDA. Anissa performed the permeability measurements and reviewed the manuscript.

Zhaoxing Wang and Aslan Mansurov, two undergraduate students at the time, participated in fouling the PSF membranes and carried out part of the SCFS experiments in the presence of NOM in solution and as a fouling layer.

The third chapter studied the effect of graphene oxide (GO) coatings on biofouling of UF membranes. GO nanosheets were edge-tethered to poly(acrylic acid) (PAA) brushes bound to polyethersulfone (PES) UF membranes. Then, SCFS was employed to show that *P. fluorescens* weaker adhesion forces to GO coated membranes. The results of this study were published in Wuolo-Journey *et al*.[74]

Karl Wuolo-Journey, a graduate student, completed the rigorous task of modifying the surface of the PES membranes to incorporate the GO nanosheets. Karl, also, carried out all the surface characterization experiments and analyzed the corresponding results. My role in this manuscript was to train Elise, an undergrad at Augsburg University at that time, and Karl on the SCFS protocol and AFM imaging. I also trained Karl on measuring the surface charge of the membranes and the contact angle using the captive bubble method. I analyzed all the SCFS data including WLC and FJC models, in addition to contributing to the writing and reviewing of the manuscript,

The fourth chapter studied the effect of temperature on the organic fouling of reverse (RO) membranes. This study investigated the effect of temperature (T =27, 35, and 40 °C) on alginate fouling of RO membranes at an intermolecular level using atomic force microscopy (AFM)-based colloidal force spectroscopy. The effect of feed water temperature on the transport properties and rate of organic fouling by sodium alginate of RO membranes was also examined using a bench-scale crossflow system. I performed all the experiments and analysis as well as the writing. This chapter has been compiled to be submitted to a peer reviewed journal.

The fifth chapter includes conclusions from the previous three chapters and recommendations for future research.

Chapter 2: Bacterial Adhesion to Ultrafiltration Membranes: Role of Hydrophilicity, Natural Organic Matter, and Cell-Surface Macromolecules

This chapter has been published in the Journal *Environmental Science and Technology*, and is cited as follows:

BinAhmed, S.; Hasane, A.; Wang, Z.; Mansurov, A.; Romero-Vargas Castrillón, S. Bacterial Adhesion to Ultrafiltration Membranes: Role of Hydrophilicity, Natural Organic Matter, and Cell-Surface Macromolecules. *Environ. Sci. Technol.* **2018**, *52* (1), 162–172. https://doi.org/10.1021/acs.est.7b03682.

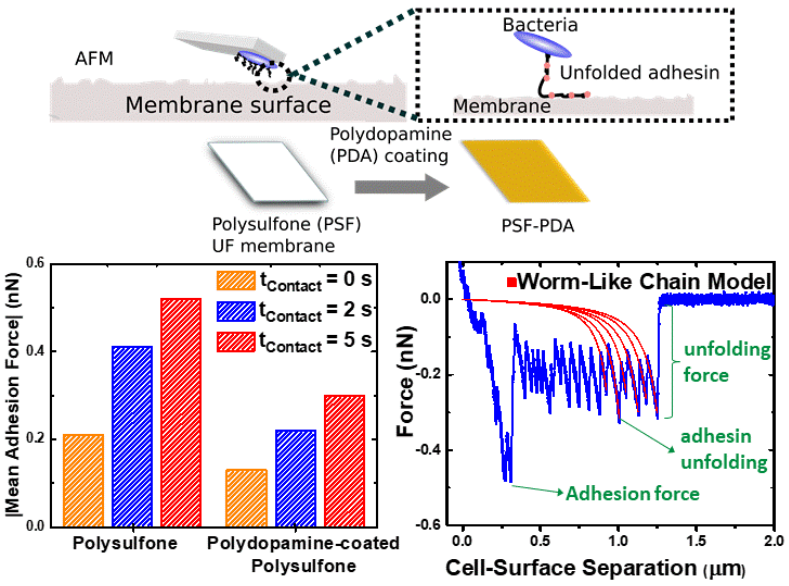

2.1 Summary

Insight into the mechanisms underlying bacterial adhesion is critical to the formulation of membrane biofouling control strategies. Using AFM-based single-cell force spectroscopy, we investigated the interaction between *Pseudomonas fluorescens*, a biofilm-forming bacterium, and polysulfone (PSF) ultrafiltration (UF) membranes to unravel the mechanisms underlying early-stage membrane biofouling. We show that hydrophilic polydopamine (PDA) coatings decrease bacterial adhesion forces at short bacterium-membrane contact times. Further, we find that adhesion forces are weakened by the presence of natural organic matter (NOM) conditioning films, owing to the hydrophilicity of NOM. Investigation of the effect of adhesion contact time revealed that PDA coatings are less effective at preventing bioadhesion when the contact time is prolonged to 2 – 5 s, or when the membranes are exposed to bacterial suspensions under stirring. These results therefore challenge the notion that simple hydrophilic surface coatings are effective as a biofouling control strategy. Finally, we present evidence that adhesion to the UF membrane surface is mediated by cell-surface macromolecules (likely to be outer membrane proteins and pili) which, upon contacting the membrane, undergo surface-induced unfolding.

2.2 Introduction

The presence of bacteria near interfaces is ubiquitous in natural and engineered aqueous environments. Near most surfaces, adhered bacteria will aggregate in a hydrated matrix of proteins and polysaccharides, known as biofilms[75]. These sessile communities are notoriously resistant to removal by biocides and disinfectants due to the protection provided by a matrix of predominantly self-produced extracellular polymeric substances

(EPS)[46,76–78]. Consequently, biofilm formation and biofouling constitute a major technical problem in membrane-based water treatment, leading to decreased permeance, selectivity, and membrane useful life[3,16,25–27,79]. The first step in biofilm formation and biofouling, termed bioadhesion, is the complex process of bacterial attachment to a substrate[38,39,80]. A variety of nonspecific interactions drive bioadhesion[50,51,80] including long-range electrostatic forces[39,81,82], and shorter ranged hydrophobic[39],van der Waals[39,81], and hydrogen bond interactions[81]. These interactions come into play through a host of bacterial cell membrane macromolecules (e.g., lipopolysaccharides, proteins[52]), as well as cell-surface adhesins (e.g., pili and flagella) that often determine bacterial adhesion to the substrate[83–86]. Cell appendages such as flagella and pili play a major role in overcoming repulsive double layer surface forces, initiating bacterial attachment[38,39,77], often at several μm from the substrate[50].

Given that bioadhesion interactions are reversible[87], insight into the mechanisms underlying early-stage bacterial attachment is essential to the formulation of biofouling-resistant membranes and biofouling prevention strategies. Nonetheless, given the myriad physical, chemical, and biological factors intervening, bioadhesion remains a poorly understood phenomenon, particularly for chemically heterogeneous interfaces such as membranes for water separations, which exist in contact with complex solution matrices[88]. Earlier studies on bioadhesion onto model polymeric (e.g., Teflon) and inorganic surfaces (glass, mica) have shown that attachment is enhanced by substrate hydrophobicity[50,89]. Several other interfacial properties influence bacterial adhesion, including nanoscale roughness and surface charge (zeta potential), as well as feed water composition (pH, ionic

strength, presence of divalent cations, organic matter properties), all of which are known to contribute to membrane fouling[3,38,39,78–80,90,91].

In addition, transport and deposition of bacterial polymers, natural organic matter (NOM), and other macromolecules at the substrate-water interface is thought to lead to the formation of a conditioning film mainly composed of organic matter[92] that may hinder[92–94], or promote[47,93,95] bacterial adhesion by providing support and nutrients for the foundation layer of a biofilm[38,39,83,96]. The role of NOM in bacterial and biocolloid adhesion is poorly understood, with previous studies reporting contradictory results[59,94,97–100]. Suwannee River (SR) NOM conditioning films decrease the attachment efficiency of MS2 virus particles to silica surfaces, possibly due to electrostatic repulsive forces that dominate at low ionic strength[94]. Conversely, at low ionic strengths, SRNOM was shown to accelerate the deposition kinetics of *C. parvum* oocysts on conditioned silica surfaces, compared to bare silica collectors[97]. Other studies focused on the effect of humic acid (HA), the main hydrophobic[98] constituent of NOM[99] in surface water[100]. HA had a minor influence on the attachment efficiency of *E. coli* cells to silica particles[98], while Suwannee River humic acid (SRHA) resulted in lower deposition of *E. coli* on quartz sand when present in suspension or as a coating film[99]. On the other hand, the effect of HA conditioning on *Pseudomonas aeruginosa* adhesion was found to be dependent on lipopolysaccarride (LPS) structure. Adhesion of *P. aeruginosa* AK 1401, having an A-band antigen in its LPS, exhibited similar adhesion forces to HA-coated silica particles as the bare silica surfaces. Conversely, *P. aeruginosa* PAO1 possesses an additional long antigen (B-band) that increased its adhesion to HA-coated silica[59].

Advanced surface analytical techniques, notably AFM-based single cell force spectroscopy (SCFS), have emerged in recent years to investigate the mechanisms underlying bacterial adhesion. In SCFS, an AFM cantilever is functionalized with a single bacterial cell, enabling measurement of the nanoscale forces between individual cells and a substrate in native aqueous environments[51,101]. In addition, SCFS can provide information on the mechanical response of cell adhesins as they contact a substrate[102,103].

In this study, we use SCFS to unravel the interactions between *Pseudomonas fluorescens*, a biofilm-forming bacterium[84,104], and polymeric ultrafiltration (UF) membranes. *P. fluorescens* is an aerobic gram negative bacterium found in soil, drinking and river water, plants, in addition to biomedical and industrial equipment[88,105–107]. We show that hydrophilic polydopamine (PDA) surface coatings significantly weaken the adhesion forces of *P. fluorescens*. While this observation underscores the importance of hydrophilicity in mitigating microbial adhesion, we also show that the antifouling properties of hydrophilic coatings are less effective for prolonged contact between the cell and the membrane surface. Further, we show that NOM conditioning films *weaken* cell-substrate adhesion forces. Finally, a significant fraction of the force measurements suggests that adhesion of *P. fluorescens* is mediated by cell surface appendages whose elastic response can be modeled via the worm-like chain (WLC) model. Our WLC analysis of adhesion forces suggests that unfolding of adhesins (pili and outer membrane proteins) is a determinant of cell attachment to membrane surfaces.

2.3 Materials and Methods

2.3.1 Membrane Fabrication and Characterization

We investigate bioadhesion on polysulfone UF membranes fabricated by non-solvent induced phase inversion[108]. Hydrophilic polydopamine[73] (PDA) surface coatings, which have been shown to be effective in the control of membrane organic fouling[49], are explored in this work as a surface modification strategy to mitigate bioadhesion[90]. Polydopamine is formed by the deposition of 3,4-dihydroxyphenylalanine (DOPA) from alkaline solution[73]. Hereinafter, we refer to PDA-coated polysulfone UF membranes as PSF-PDA, while the unmodified polysulfone control membranes are designated PSF membranes. In addition, the effect of NOM conditioning films is investigated by depositing Upper Mississippi River NOM (International Humic Substances Society, St. Paul, MN) on the membrane surfaces via pressure-driven filtration of 10 ppm NOM solution.

The interfacial properties (wettability, surface charge and nanoscale roughness) and water permeability coefficient of the PSF and PSF-PDA membranes were characterized. Detailed experimental procedures and characterization data are presented in Membrane Fabrication and Surface Modification and Membrane Characterization (Appendix A).

2.3.2 Single-Cell Force Spectroscopy (SCFS) Experiments

Bacterial Strain and Growth Conditions The strain of *P. fluorescens* used in our experiments, ATCC 13525, originates from pre-filter tanks[109]. As with other bacteria in the *Pseudomonas* genus, *P. fluorescens* has a high adaptation[110] and biofilm formation potential[104,111], possessing a variety of proteinaceous adhesins[112], such as flagella and pili, which are also fundamental to bacterial motility[105,113]. The small radius of pili (1-5 nm[114])

is believed to help *P. fluorescens* overcome electrostatic repulsive forces with the substrate[38,114]. Pili also promote *P. fluorescens* bioadhesion *via* hydrophobic interactions with hydrophobic substrates[114], due to the high content of hydrophobic amino acids in the constituent pilin proteins[115]. LPS[86,116,117] and outer membrane proteins (OMP)[39,59], such as LapA[83,84], also contribute to adhesion of *P. fluorescens.* Experimental details on bacterial culture preparation and growth conditions are provided in the Bacterial Culture Preparation and Growth Conditions (Appendix A).

Membrane sample and cantilever preparation A UF membrane coupon (~3×3 mm^2) was glued using epoxy (3M Quick Set Epoxy Adhesive) to a piranha-cleaned and UV/O_3-treated glass disc, and allowed to set for 10 minutes. Subsequently, a 20-µL droplet of bacterial suspension was deposited directly on the glass next to the membrane coupon, allowing the droplet to stand for 30 minutes to permit bacterial attachment to the glass surface. The glass disk was rinsed with 2.5 mL PBS to remove unattached bacteria, avoiding contact between the membrane surface and the bacterial suspension. Finally, the glass disk was inserted in the fluid cell (Fluid Cell Lite, Asylum Research), and the cell was filled with 1.4 mL of test solution. We conducted experiments in PBS or in 10 ppm NOM solution containing 156.4 mM KCl and 0.5 mM $CaCl_2$ (I = 158 mM, pH 7.2-7.4), i.e., conditions approximating those of PBS, to perform experiments under comparable conditions.

Tipless SiN cantilevers (nominal k = 0.01 N/m, MLCT-O10 probe "C", Bruker) were used. Wet polydopamine (wPDA) was used as a wet adhesive to immobilize a single bacterial cell on the cantilever, as done by others[50,52,118,119]. The adhesive properties of wPDA, which

contrast the antifouling properties of PDA explored in this work (and previously by others[49,120,121]), are thought to depend on the degree of pH-induced oxidation of DOPA catechol groups to quinones[122–124], and the extent of crosslinking of DOPA monomers[73,125]. In our work, we observed that longer deposition times on the membranes (~45 min) resulted in hydrophilic anti-fouling coatings, whereas shorter (15 minutes) deposition times rendered adhesive cantilevers on which bacterial cells could be robustly immobilized. We further observed that wPDA coatings completely lost their adhesiveness after ~3 hours, possibly due to conversion to non-adhesive (oxidized) PDA. Determination of the structures of adhesive wPDA and non-adhesive PDA, as well as their formation mechanisms, are active areas of research[126–128] that fall outside of the scope of this study.

To ensure adhesiveness of the wPDA, the AFM probes were coated immediately before each experiment as follows: the UV/O_3-cleaned AFM probe was immersed in 10 mL of 4 g/L PDA solution (pH 8.5) prepared as described in the SI. After 15 minutes under shaking at 60 RPM, the probe was rinsed with deionized (DI) water (18.2 MΩ-cm, Barnstead) and dried under a gentle nitrogen flow before mounting the probe on the AFM probe holder. The AFM head was then lowered into the fluid cell, immersing the probe in the solution (PBS or NOM) and allowing the cantilever deflection to reach a stable deflection signal (which was typically observed within 30-60 min).

Force Measurements Single-cell force spectroscopy (SCFS) was performed at room temperature using an MFP-3D-Bio atomic force microscope (Asylum Research, Santa Barbara, CA) integrated into a Zeiss Axio Observer A.1 inverted optical microscope (IOM). The cantilever spring constant was obtained using the thermal noise method[129], and was

always found to be within range specified by the manufacturer. The optical lever sensitivity of the cantilever was determined from the slope of the contact region of deflection signal (V) vs. piezo extension (nm) curves collected over the bare glass. To immobilize a single bacterial cell on the cantilever, we adapted previously reported experimental procedures[50,52]. Using the 60× objective of the IOM, the wPDA-coated cantilever was directed towards a cell (on the glass) aligned parallel to the front edge of the cantilever. The cantilever was engaged in contact mode over the cell for 5 minutes with a 1 nN loading force[50], after which the cantilever (functionalized with the bacterial cell) was withdrawn.

To begin force measurements, the cantilever was translated towards the membrane surface using the AFM top view digital camera. Approach-retraction force cycles were recorded at a 400 nm/s cantilever speed and 4 μm ramp (8-μm ramps were used when long range interactions were observed), with an approach (target loading) force of 600 pN. A dwell or contact time ($0 \leq t_{Contact} \leq 5$ s), defined as the time in which the bacterial cell can remain in contact with the membrane surface under a constant loading force, was investigated in a subset of the experiments. Experiments in NOM solution and/or conditioning film were carried out at $t_{Contact} = 5$ s only. Force curves were collected at multiple randomly chosen locations of the membranes, measuring 3 force curves over each point, to minimize the deposition of cell-surface macromolecules on the UF membrane (no systematic changes in adhesion force were observed in sequential measurements on the same membrane location, or between locations). A total of ≈ 100 force curves (minimum: 93, maximum: 129) were collected for each combination of membrane type and experimental conditions, using at least 3 different bacterial cells (i.e., at least 3 separate single-cell experiments). Both approach and pull-off force curves were measured, but only pull-off force curves were

considered to quantify adhesion. Raw data in terms of cantilever deflection as a function of piezo Z position were first converted to force versus cell-substrate separation curves using the method described by Senden[130]. The maximum adhesion force and rupture separation (i.e., the separation at which cell-substrate forces vanish) were extracted from each pull-off force curve using a Matlab code. A representative approach/pull-off force cycle, showing the maximum adhesion force and rupture separation, is shown in **Figure A. 1**.

Cell viability was assessed after each experiment using a live/dead assay (Baclight, Thermofisher Scientific) consisting of SYTO 9 and propidium iodide (PI) fluorescent nucleic acid stains. If the cell was dead (red fluorescence) or dislocated (i.e., if the cell position on the cantilever changed during the experiment), the collected data were discarded. Only data collected with a live cell (green fluorescence) that remained at its initial location throughout the experiment are reported herein.

2.4 Results and Discussion

2.4.1 Membrane Characterization

Contact Angle Contact angle provides information about the hydrophilicity of the membranes, a well-known attribute of fouling-resistant surfaces[1,45–47]. Contact angle measurements of an ultrapure water droplet on various membrane surfaces are shown in **Figure 2. 1.** The contact angle of PSF membranes was $\theta = 62.7° \pm 7.4°$. A more hydrophilic surface results from PDA deposition, which exhibits a contact angle $\theta = 51.5° \pm 5.7°$; the observed increase in hydrophilic character of the PSF-PDA membrane is consistent with previous results of PSF-PDA-modified membranes[1] and other organic and

inorganic[122,125,131–133] substrates. **Figure 2. 1.** also shows that both the PSF and PSF-PDA membranes are rendered more hydrophilic after deposition of an NOM conditioning film, when compared to their NOM-free counterparts. This can be attributed to the hydrophilic components of NOM, which have been shown to render membrane surfaces more hydrophilic after fouling experiments[134]. The hydrophilic components of NOM are believed to be non-humic substances[134] such as polysaccharides[135,136] and proteins[136]. The presence of polysaccharides on NOM-conditioned PSF and PSF-PDA membranes is supported by FTIR data (**Figure A. 2**. and **Figure A. 3**.), showing an increase in the ~1078 cm^{-1} and 1105 cm^{-1} bands, corresponding to polysaccharides and polysaccharide-like molecules[135,137].

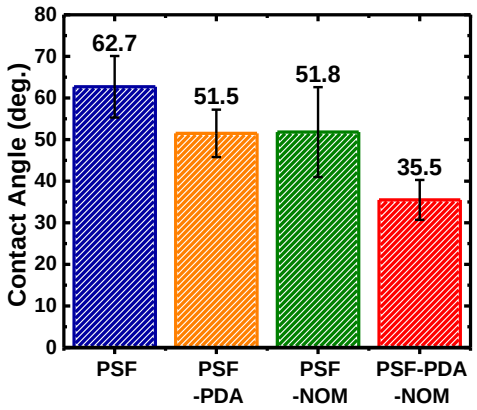

Figure 2. 1. Sessile water drop contact angle measurements on PSF and PSF-PDA membranes, both pristine and coated with an NOM film (as described in Appendix A). For each membrane type, the reported contact angle is an average of at least 18 measurements, collected over 2 separately cast membrane samples of the same type; error bars indicate one standard deviation ($p < 0.05$ for all pairwise comparisons, except for PSF-PDA compared to PSF-NOM).

Zeta Potential The charging behavior of a solid-water interface, as revealed by streaming potential measurements, provides information about the functional groups present on the membrane surface, as well as surface charges that influence cell deposition. The zeta

potential (ξ) of PSF, PSF-PDA, and NOM-conditioned membranes is shown in **Figure A. 4**. as a function of pH. PSF membranes exhibited a negative ξ over the entire pH range (4 to 10), due to OH^- adsorption on the PSF membrane surface[49]. In contrast, PSF-PDA membranes attained a positive zeta potential at pH < 4.5, due to protonation of –NH– to $–NH_2^+–$ in PDA. At basic pH, deprotonation of hydroxyl groups in PDA results in negative zeta potential[49]. **Figure A. 4**. further shows that the NOM conditioning film results in negative ξ over the entire pH range investigated for both PSF and PSF-PDA membranes. This is consistent with the presence of polysaccharides and polysaccharide-like substances that increase the number of negatively charged functional groups on the membrane surface[135]. The deposition of negatively charged humic acid (HA), alginate (a polysaccharide), and a combination of HA and alginate has been shown to decrease (i.e., render more negative) the zeta potential of polyethersulfone (PES) UF membranes[136]. Comparing the four membrane types, **Figure A. 4**. shows that at low pH (pH < 5) the zeta potential of NOM-conditioned membranes is lower (more negative) than that of pristine PSF and PSF-PDA membranes. On the other hand, all membranes exhibit similar surface charge at pH 7.2-7.4, the pH of our SCFS experiments (Section 2.4.2. Single-Cell Force Spectroscopy), irrespective of NOM-conditioning or PDA surface modification.

We also measured the zeta potential of *P. fluorescens* cells (**Figure A. 5.**, details in the Appendix A). Bacterial cells attain a negative surface charge at pH values corresponding to their normal living environment[76,138]. As shown in **Figure A. 5.**, bacteria exhibit a negative zeta potential at pH 7.2-7.4, becoming less negative with increasing ionic strength[139–141] due to electrical double layer compression[139,140]. **Figure A. 5.** also shows that the zeta potential of *P. fluorescens* was the same when suspended in PBS or NOM

solution, suggesting that both solutions yield similar screening of bacterial surface charge at comparable ionic strength. This observation agrees with the work of Yang *et al.*[99], who found that the zeta potential of motile and nonmotile *E. coli* was the same in the presence and absence of SRHA. Interestingly, the zeta potential of *P. fluorescens* was approximately the same as that of the cell-free NOM solution, possibly due to the presence of similar functional groups (e.g., carboxylates) in NOM and the surface of bacteria.

In summary, **Figure A. 4.** and **Figure A. 5.** show that both the bacterial and membrane surfaces possess negative zeta potentials under the conditions of the SCFS experiments reported below, irrespective of the presence of NOM or (for the membranes) PDA surface coating.

Roughness and Permeability **Figure A. 6.** presents AFM images of PSF and PSF-PDA membranes. The root-mean-squared (RMS) roughness, defined as the standard deviation of height z-values measured over the scanned area[142,143], was calculated from the AFM images. The RMS roughness of PSF and PSF-PDA membranes was 2.45 ± 0.32 nm and 3.74 ± 1.44 nm, respectively. The slight increase in roughness of PSF-PDA is presumed to be due to PDA nanoscale aggregates formed during deposition[49]. The permeability coefficients of the membranes presented in **Figure A. 7.**, are within the range expected for UF membranes[67,144]. The slightly higher permeability of PSF-PDA membranes can be attributed to the increased hydrophilicity of the PDA layer covering both the membrane surface and the inner walls of the pores[121].

2.4.2. Single-Cell Force Spectroscopy

In this section, we systematically investigate the effects of UF membrane hydrophilicity, cell-substrate contact time, and NOM conditioning on the adhesion of *P. fluorescens* to polysulfone UF membranes. Given the stochastic nature of microbial adhesion[52,118], raw data (maximum adhesion force and rupture separation, cf. **Figure A. 1.** for definition) are reported as histograms (see Appendix A).

Effect of Membrane Hydrophilicity and Contact Time The adhesion of single *P. fluorescens* cells on polysulfone (PSF) and polydopamine-coated polysulfone (PSF-PDA) membrane surfaces is investigated at contact times ($t_{Contact}$) of 0, 2 and 5 s in **Figure 2. 2.** (A) and (B), which report the average maximum adhesion force and rupture separation, respectively. All experiments were performed in PBS buffer, pH 7.4, at room temperature. The histograms of the maximum adhesion force (**Figure A. 8.**) and rupture separation (**Figure A. 9.**), from which **Figure 2. 2.** was obtained, show broad distributions, derived from complex interactions between the membrane and biopolymers present on the cell surface (see Section 2.4.2. Single-Cell Force Spectroscopy). By contrast, cell-free control measurements (Figures **Figure A. 10.** - **Figure A. 15.**) between a wPDA-coated cantilever and the membrane surface showed significantly higher average adhesion forces (~1 nN, compared to forces < 1 nN with bacterial probes, cf. **Figure A. 12.**) and much shorter rupture distances (~100 nm, compared to rupture at > 1 µm with bacterial probes, cf. **Figure A. 15**.), demonstrating that the forces presented in **Figure 2. 2. (A)** and **Figure A. 8.** are due to bacterium-membrane interactions.

Figure 2. 2. (A) and **Figure A. 8.** show that the distribution of adhesion force measurements became broader, i.e., the average adhesion force increased, as $t_{Contact}$ increased from 0 to 5 s. Similarly, **Figure A. 8.** shows that the fraction of predominantly repulsive forces (corresponding to the column labeled "NO") decreased with increasing contact time over both PSF and PSF-PDA membranes. In these instances, attractive forces were too weak (on the order of 40 pN or less), and could not be discriminated from the random fluctuations in the deflection of the cantilever about zero force. Data on **Figure 2. 2. (A)** thus show that adhesion of bacteria to membrane surfaces is a time-dependent phenomenon[50], irrespective of the membrane chemistry, with bacterial cells adhering more strongly to a surface when a sufficiently prolonged contact time is allowed. The higher mean adhesion force at longer $t_{Contact}$ suggests that adhesins undergo structural changes that strengthen attachment on contacting the membrane surface. The range of $t_{Contact}$ explored in Figure 2 (0 – 5 s) is shorter than the particle-substrate contact times encountered in membrane filtration, which would exceed the hydraulic residence time of the feed channel (> 10 s for typical module sizes and crossflow velocities of 10 cm s^{-1} [18,145]), but nonetheless suffices to observe surface-induced conformational changes in bacterial adhesins, which occur over times scales of ~100 – 700 ms [146]. An important observation in **Figure 2. 2. (A)** is that average adhesion forces over PDA-coated membranes were always weaker than those measured on PSF membranes at the same $t_{Contact}$. This is due to the interfacial properties of the pristine and PDA-coated polysulfone membranes. The surface charge of both PSF and PSF-PDA membranes is similar (≈ -25 mV at pH 7.4, **Figure A. 4.**), and the bacterial zeta potential is also weakly negative (≈ -5 mV, extrapolating data in **Figure A. 5.** to the ionic strength of PBS). Further, both membranes have similarly low (< 4 nm) RMS

surface roughness (**Figure A. 6**.). These results suggest that the weaker adhesion on PDA-coatings does not stem from surface electrostatic interactions or nanoscale roughness, but rather from the increased hydrophilicity of PSF-PDA membranes (Θ = 51.5º ± 5.7º, compared to Θ = 62.7º ± 7.4º for PSF, $p < 0.05$, cf. **Figure 2. 1.**). Stronger bioadhesion on more hydrophobic substrates (PSF in this case) has been reported by different studies using various bacterial strains[38,39,50,89,118]. Our results therefore indicate that *P. fluorescens* uses adhesins (probably of proteinaceous nature, such as pili and outer membrane proteins[112]) that depend on surface hydrophobicity for interaction.

Figure 2. 2. (B) presents the mean rupture separation (defined as the distance at which the adhesion force vanishes, cf. **Figure A. 1.**), obtained from the distributions shown in **Figure A. 9.** Long rupture separations, reaching up to 9 µm, were observed in some measurements (**Figure A. 9.**), which can be explained by the presence of long flagella and pili in *P. fluorescens.*[50,113,115,147,148] For both PSF and PSF-PDA, longer rupture separations were recorded as $t_{Contact}$ was increased from 0 to 2 s, but remained unchanged (or increased slightly for PSF-PDA) on increasing $t_{Contact}$ to 5 s. The increase in average rupture separation as $t_{Contact}$ was varied from 0 to 2 s indicates that at longer $t_{Contact}$, longer adhesins (possibly pili) mediated attachment or more contact points along a single pili were established. Beyond 2 seconds, the rupture separation did not vary significantly but the adhesion became stronger (**Figure 2. 2. (A)**), suggesting that more adhesins of similar length were involved[50]. Additionally, we note that average rupture separation was always smaller over PSF-PDA compared to PSF membranes for the same $t_{Contact}$ (**Figure 2. 2. (B)**). This observation is analogous to the stronger adhesion observed on PSF compared to PSF-PDA surfaces (**Figure 2. 2. (A)**), suggesting that adhesins can engage more binding sites

on the (more hydrophobic) PSF membrane surface, resulting in longer rupture separation distances.

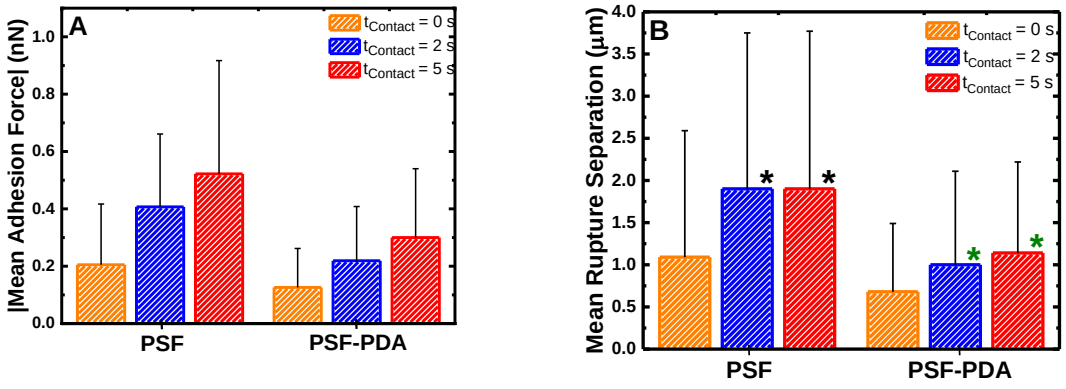

Figure 2. 2. Average maximum adhesion force (A) and mean rupture separation (B) of single *P. fluorescens* cells on PSF and PSF-PDA membranes investigated for different contact times ($t_{Contact}$) denoted in the inset. The histograms from which the reported means were computed are given in **Figure A. 8.** and **Figure A. 9.** ($p < 0.05$, except for pairwise comparisons indicated by *).

Effect of NOM on Microbial Adhesion To investigate the effect of NOM on microbial adhesion, we performed two types of experiments at $t_{Contact}$ = 5 seconds. In the first set, we investigated the effect of dissolved NOM on bioadhesion by conducting SCFS in a 10 mg/L Upper Mississippi River NOM solution at ionic strength (158 mM) and pH (7.2-7.4) that approximate those of PBS. The selected concentration of NOM is a typical upper limit of the NOM concentration in surface waters (2-10 mg/L).[149] In the second set of experiments, NOM was deposited on the surface of the membranes as a conditioning film (see Appendix A). SCFS experiments with NOM-conditioned membranes were also performed in 10 mg/L NOM solution at the ionic strength and pH indicated above. The NOM conditioning film resulted in brown coloration of the membrane, and its presence was verified by FTIR as explained in Section 2.4.1 Membrane Characterization (see also **Figure A. 2.** and **Figure**

A. 3.). **Figure 2. 3. .** summarizes the mean of the maximum adhesion force and mean rupture separation computed from histograms presented in **Figure A. 16.** and **Figure A. 17.** of Appendix A. Data for experiments performed in PBS ($t_{Contact}$ = 5 s) are also included in **Figure 2. 3. .** for comparison.

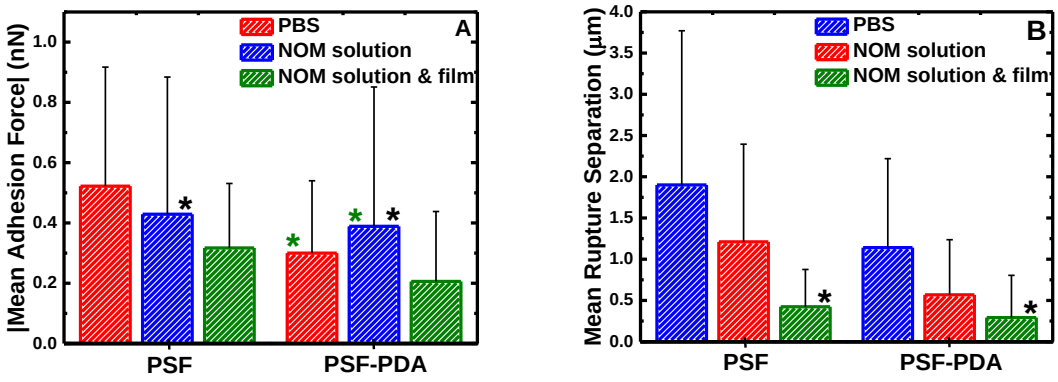

Figure 2. 3. Mean of the maximum adhesion force (A) and mean rupture separation (B) of single P. fluorescens cells on PSF and PSF-PDA membranes investigated in different solution chemistries, denoted in the inset: PBS, 10 ppm NOM solution, and NOM-conditioned membranes in 10 ppm NOM solution. The histograms from which the reported means were computed are given in **Figure A. 16.** and **Figure A. 17.** (p < 0.05, except for pairwise comparisons indicated by *).

Figure 2. 3. .(A) shows that the presence of NOM simultaneously in solution and as a conditioning film results in weaker adhesion, compared to experiments in NOM solution (without surface conditioning) and PBS. Also, weaker adhesion forces are observed on the PSF membrane when NOM is present only in solution compared to experiments performed in PBS. On the other hand, the experiment performed on PSF-PDA membranes in NOM solution resulted in stronger adhesion forces compared to PBS (-0.39 nN vs. -0.30 nN, respectively). Experiments with 3 different bacterial cell probes were conducted with the PSF-PDA membrane tested in NOM solution, yielding mean adhesion forces (-0.48 nN, -

0.65 nN and -0.08 nN) that varied by one order of magnitude. We speculate that the large variation in adhesion – which may be due to variations in bacterial surface hydrophobicity across different cells[150] – may explain the stronger adhesion observed in NOM solution with the PSF-PDA membrane. The effect of NOM on the mean rupture separation is described in **Figure 2. 3. . (B)**, showing smaller rupture separations in NOM solution, which become shorter still for adhesion on NOM-conditioned membranes. **Figure 2. 3. .** thus shows that NOM, when present simultaneously as a dissolved foulant and as an adsorbed film, weakens, and shortens the range of, adhesive interactions between the microbe and the membrane. A further observation from **Figure 2. 3. .** is that, for the same NOM solution chemistry, adhesive forces are weaker and shorter-ranged over PSF-PDA membranes compared to PSF membranes; this observation is consistent with findings in PBS, as depicted in **Figure 2. 2.**, and are attributable to the more hydrophilic PSF-PDA surface.

The weaker adhesion of *P. fluorescens* in the presence of simultaneously dissolved and adsorbed NOM is at odds with the notion that macromolecular adsorbed films promote bacterial attachment.[83,93,151] Nevertheless, we note that observations of lower deposition of biocolloidal particles on NOM-coated surfaces are not unprecedented; lower deposition rates of oocysts on NOM-coated silica collectors have been reported[97], while NOM was found to decrease adhesion of Gram negative *E. coli* and Gram positive *S. suis* bacteria to soil colloidal particles, possibly due to electrosteric repulsive forces[140]. In our experiments, the surface charge of control and NOM-conditioned membranes was similar ($\xi \approx$ -25 mV, cf. **Figure A. 4.**), while bacteria suspended in NOM solution and PBS also exhibited similar ξ values ($\approx$ -5 mV, extrapolating data in **Figure A. 5.** to the ionic strength of PBS).

These measurements indicate that NOM does not significantly modify the surface charge of the bacteria or the membranes. Nonetheless, we note that the NOM-conditioned PSF membranes are as hydrophilic as the non-conditioned PSF-PDA membranes, and that the NOM-coated PSF-PDA membrane exhibits the lowest contact angle of all the systems measured (see **Figure 2. 1.**). Consequently, NOM creates a hydrophilic coating on the membrane that weakens bacterial attachment, and reduces the rupture separation through a reduction of binding sites available to adhesins. The hydrophilic character of NOM films is expected given that NOM contains functional groups, such as carboxylic acid and amine groups, that can form hydrogen bonds with water[98]. Further, our FTIR data (**Figure A. 2.** and **Figure A. 3.**) show that NOM contains polysaccharides and polysaccharide-like components, both of which are hydrophilic constituents of NOM. The hydrophilicity of the NOM film can also be explained in terms of the high water content of the NOM conditioning layer.[152] Steric repulsion, which acts at short distances (< 15 nm)[89,140], may also weaken adhesion on NOM-coated surfaces: cell-surface structures, such as lipopolysaccharide chains, can introduce steric repulsive forces[59,89] against macromolecular polysaccharide chains that protrude from the NOM adsorbed on the membrane.

The weaker adhesion observed in PSF membranes when NOM is present only in solution can be attributed to Ca^{2+}-promoted complexation of NOM with sulfonyl functional groups on the membrane surface.[153] Ca^{2+} ions, present in NOM solution, can adsorb to the UF membrane surface[154] reducing the electrostatic repulsion between NOM and the membrane[136] and forming a bridging complex with carboxyl groups in NOM.[155] The aromatic and aliphatic content of NOM could also lead to the adsorption of NOM to

hydrophobic PSF membrane surfaces via hydrophobic interactions.[154,156] Since the NOM employed in this work is predominantly hydrophilic (cf. **Figure 2. 1.**), its adsorption to PSF membranes decreases the magnitude of bacterial adhesion forces and the rupture separation (cf. **Figure 2. 3. . (A) and (B)**). At the same time, it is possible that NOM also adsorbs on the bacterial cell surface[59,157], possibly due to mediation of Ca^{2+} ions in solution. This would result in a more hydrophilic bacterial cell surface, leading to weaker adhesion forces. Steric hindrance arising when a bacterial cell and substrate are both coated with a macromolecule (e.g., NOM)[157] may also be responsible for weaker adhesion forces.

Molecular Basis of Microbial Adhesion to UF Membranes A significant fraction (~30% at t_{Contact} = 5 s in PBS) of the pull-off force-separation measurements collected over PSF and PSF-PDA membranes exhibited a series of consecutive spring instabilities, resembling the "sawtooth" pattern characteristic of force unfolding of biomolecule domains.[158] The representative force curve in **Figure A. 1.** shows that following strong, unspecific adhesion at short separations, consecutive sawtooth peaks are observed, which are usually ascribed to progressive unwinding of biomolecule domains.[103,159,160] In agreement with previous work on protein unfolding[161], we find that each peak is well fitted ($R^2 \geq 0.98$) to the worm-like chain (WLC) model of polymer elasticity[162] (cf. **Figure A. 1.**). The WLC model describes the polymer (in this case, the bacterial surface macromolecule) as a semi-flexible chain that is randomly oriented at any point.[102,162,163]

The WLC fit to the force (F) – separation (z) profile along the sawtooth-like peaks (**Figure A. 1.**) is given by

$$F(z) = \frac{k_B T}{L_p}\left[\frac{1}{4}\left(\frac{L_c - z}{L_c}\right)^{-2} + \frac{z}{L_c} - \frac{1}{4}\right] \qquad (2.1)$$

where k_B is Boltzmann's constant, and T = 298 K is the absolute temperature.[102,161] Two fitting parameters characterize a semi-flexible chain as described by the WLC model: the persistence length (L_p) and the contour length (L_c). L_p is a property that reflects the flexibility of the chain bonds[164], and is thus a measure of the chain rigidity[86]; while L_c is the total length of the extended polymer without stretching its backbone.[102,164,165] The WLC model conceptualizes the polymer as an entropic chain: when undeformed, macromolecular chains are in a high entropy, random coil configuration that resists stretching; an external force F must be applied to elongate the polymer chain, i.e., to unfold the macromolecule.[162] Stretching results in a lower configurational entropy due to alignment of the constituent segments along the direction of load.[166]

Equation 2.1 was fitted to all the force curves exhibiting the sawtooth-like peaks. In all cases, we excluded the unspecific, high-adhesion peak (cf. **Figure A. 1.**), where the force-extension is not well-defined, and excluded peaks resulting in L_p values < 0.15 nm (i.e., smaller than the length of a C-C bond[163]) and > 1.0 nm[162]; persistence lengths exceeding 1 nm indicate that, in addition to entropy, hydrophobic interactions which are not accounted for by the WLC model contribute to protein extension.[167] The distribution of best-fit L_p values is presented in **Figure 2. 4. (A)**, showing that the persistence length is narrowly distributed between 0.15 nm and 0.3 nm, with an average L_p of 0.26 nm and 0.27 nm obtained for bacteria adhering on PSF and PSF-PDA, respectively. The approximately equal values obtained over both membrane types reflect the fact that L_p is an intrinsic property of the biopolymers intervening in bacterial adhesion, and is thus independent of the chemistry of the substrate. A salient observation is that the mean persistence length is consistent with that obtained from protein unfolding experiments (L_p = 0.36-0.4

nm[84,161,162]), i.e., with the persistence length of an unfolded polypeptide.[161,162] The data in **Figure 2. 4. (A)** therefore indicate that proteinaceous adhesins play a major role in attachment of *P. fluorescens* on the UF membrane surfaces. **Figure 2. 4 (B)** and **(C)** present the distribution of forces measured at the spring instabilities in each sawtooth-like peak (cf. **Figure A. 1.**), and the number of sawtooth-like peaks per cell pull-off, respectively. We refer to these quantities as the unfolding forces ($F_{\text{Unfolding}}$, **Figure 2. 4. (B)**) and number of unfolding events per cell pull-off ($N_{\text{Unfolding}}$, **Figure 2. 4. (C)**), respectively. We observed that the distribution of unfolding forces is approximately Gaussian over both membrane types, but a higher average unfolding force is observed over PSF compared to PSF-PDA (-0.35 nN vs. -0.24 nN, respectively, cf. **Figure 2. 4. (B)**). Moreover, we observed a broader distribution of the number of unfolding events per cell pull-off over PSF membranes than over PSF-PDA membranes (**Figure 2. 4. (C)**), and, on average, fewer unfolding events over PSF-PDA (5.3 ± 5.2) compared to PSF (6.4 ± 5.0).

We propose that data in **Figure 2. 4. (B)** and **(C)** can be explained in terms of unfolding of cell-surface proteins of *P. fluorescens* cells during bacterial adhesion. In support of this view, we note the well-established observation that proteins lose conformational stability near hydrophobic interfaces[168], given that hydrophobic interactions between the hydrophobic protein core and a hydrophobic substrate stabilize the unfolded state.[51,166,168,169] Protein unfolding is more significant over PSF surfaces (note the higher average number of unfolding events, cf. **Figure 2. 4. (C)**) because PSF surfaces are more hydrophobic than PSF-PDA membranes (cf. **Figure 2. 1.**). We surmise that adhesin proteins in *P. fluorescens* unfold, or partially unfold to a "molten" globule state[170] on the surface of the membrane, and that the forces reported in **Figure 2. 4. (B)** are those

necessary to desorb the unfolded (or partially unfolded) adhesin proteins from the membrane surface. On the surface of PSF membranes, adhesin proteins can establish stronger hydrophobic interactions, hence the higher unfolding forces shown in **Figure 2. 4. (B)**. These unfolding forces are in fair agreement with values (100 - 400 pN) observed during force-unfolding of proteins.[83,151,161,171,172] The observations made in **Figure 2. 4. (B)** are consistent with reported stronger adhesion forces of lysozyme on PSF membranes compared to adhesion on the more hydrophilic 2-hydroxyethyl methacrylate (HEMA)-grafted polysulfone.[169] Similarly, using AFM, adhesion forces of three different proteins (bovine serum albumin (BSA), fibrinogen, and human FXII) were weaker over more hydrophilic surfaces (contact angle less than 60°) than on more hydrophobic surfaces.[173] The tendency of proteins to adhere more readily to hydrophobic surfaces was also shown using lysozyme, fibrinogen, and BSA.[174]

We also obtained best-fit values of the contour length, finding that it ranged from 286 nm for sawtooth-like peaks at short separations to 9950 nm at long separations. Further, we calculated the increase in the contour length ΔL_c between two consecutive unfolding peaks (work not shown), as done by others[83,165,175], finding that ΔL_c was not constant, suggesting that the adhesin proteins are partially unfolded upon contact with the surface.[83] In *P. fluorescens*, proteins such as LapA are known to mediate adhesion. [83,84,111] However, L_c for LapA does not extend beyond 1875 nm[83,84], whereas we observe contour lengths of several microns. It is therefore likely that membrane proteins such as LapA are responsible for bacterial adhesion when the observed rupture separation is 1 - 2 µm. For longer rupture separations, adhesion is likely due to pili, which are several-micrometer-long structures comprising pilin proteins.[176,177] Finally, we examined the force-separation data collected

on NOM-coated membranes (**Figure A. 18.**), finding that a significant fraction (39% for PSF, 24% for PSF-PDA) of the measurements exhibit the signatures of force unfolding. The distribution of best-fit L_p values revealed mean values (**Figure A. 18. (A)**) in close agreement with those obtained with NOM-free membranes (**Figure 2. 4. (A)**), suggesting that the sawtooth patterns are due to the elasticity of bacterial adhesins, rather than stretching of adsorbed NOM. We also note that a smaller number of unfolding events per pull-off was observed on NOM-coated membranes (**Figure A. 18. (C)**) compared to NOM-free membranes (**Figure 2. 4. (C)**). It is possible that the NOM-conditioning film, through a combination of hydrophilicity and steric repulsion, results in a smaller number of adhesin proteins contacting and attaching to the substrate.

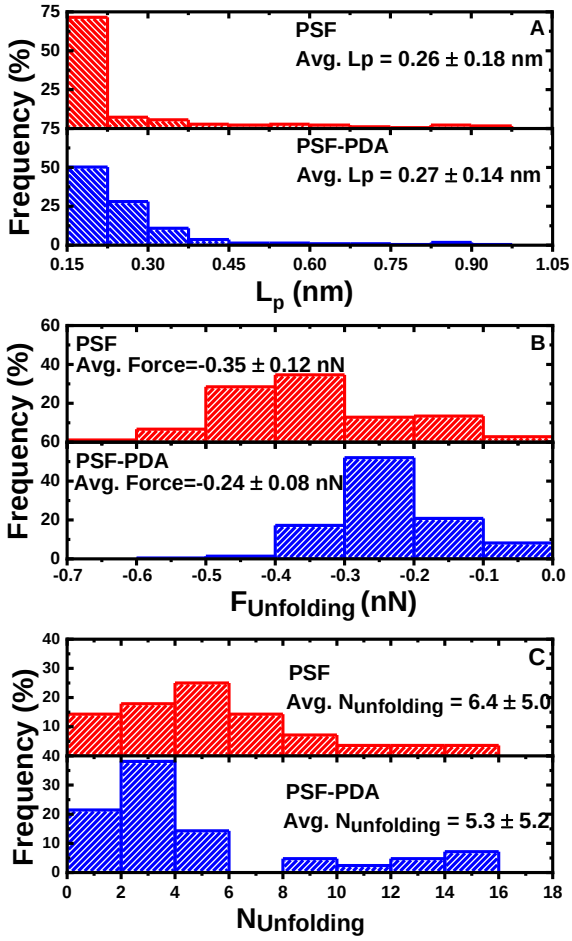

Figure 2. 4. (A) Distribution of best-fit persistence length values (L_p), obtained from WLC model fits to the pull-off force curve of single *P. fluorescens* cells. (B) Distribution of the unfolding forces ($F_{Unfolding}$, the force measured at the sawtooth peak, cf. **Figure A. 1.**), defined as the force necessary to unwind a macromolecular domain. (C) Distribution of the number of unfolding events ($N_{Unfolding}$, the number of sawtooth-like peaks per cell pull-off). The mean of each histogram is shown in the inset. Data were collected with single bacterial cells over PSF membranes (upper panel in A, B and C), and PSF-PDA membranes in PBS buffer (pH 7.4) at $t_{Contact}$ = 5 s. The histograms reflect 179 WLC fits to sawtooth-like unfolding events, identified in 28 retraction force curves over PSF membranes; and 221 sawtooth-like unfolding events observed in 42 retraction force curves over PSF-PDA membranes.

2.5. Environmental Implications

This work employed SCFS to understand bacterial adhesion to UF membrane surfaces, the first stage in membrane biofouling. Using *P. fluorescens* as a model biofilm-forming bacterium, we investigated the effect of PDA deposition on bioadhesion to polysulfone UF membranes. Weaker adhesion forces were observed on the more hydrophilic PSF-PDA UF membranes compared to the unmodified control PSF membranes. Nevertheless, we observed that the adhesion force increased with bacterium-UF membrane contact time, with the PDA membrane exhibiting an average adhesion force at $t_{Contact}$ = 5 s that is greater than that of the unmodified (and more hydrophobic) polysulfone at 0 s. When the membranes were challenged with bacterial suspensions in batch deposition experiments (**Figure A. 19.**, experimental details are given in the Appendix A), we observed that the difference in the number of deposited cells (PSF: 760 ± 720 mm^{-2}; PSF-PDA: 340 ± 250 mm^{-2}) was not statistically significant (p = 0.11, two sided, unpaired t-test). The strong bioadhesion forces observed at long $t_{Contact}$, together with the data in **Figure A. 19.**, call into question the effectiveness of simple hydrophilic coatings in controlling biofouling, considering that bacterium-membrane contact would be frequent and prolonged in membrane filtration. Similar observations have been made by others[90,178]. On the other hand, the combination of PDA surface modification with biocidal nanoparticles (e.g., Ag)[120], appears to be a promising strategy to slow down biofouling rates. Insights into molecular level phenomena underlying bacterial adhesion to membrane surfaces also emerge from this study. In bacteria which rely on hydrophobic adhesins for attachment, results pressented herein suggest that surface-induced protein unfolding on hydrophobic

membrane substrates (possibly involving outer membrane proteins, or pilin proteins) promotes bacterial attachment.

Acknowledgments

We gratefully acknowledge funding from the United States Geological Survey through the Minnesota Water Resources Center (grant no. MN WRC 2015MN362B), and from 3M Co. (Non-Tenured Faculty Award Program). Parts of this work were carried out in the Characterization Facility and Minnesota Nano Center at the University of Minnesota, which receive partial support from NSF through the MRSEC and NNIN programs, respectively. S. BA. acknowledges the support of a Ling Graduate Fellowship in Environmental Engineering. A. H. acknowledges the support of the Norwegian Center for International Cooperation in Education Partnership Program with North America. We also acknowledge Nathan Karp for his contributions to the preliminary stages of this study. We thank the University Imaging Centers at the University of Minnesota for support, and Dr. Guillermo Marqués for technical assistance.

Chapter 3: Do Graphene Oxide Nanostructured Coatings Mitigate Bacterial Adhesion?

This chapter has been published in the Journal *Environmental Science: Nano*, and is cited as follows:

Wuolo-Journey, K.; Binahmed, S.; Linna, E.; Romero-Vargas Castrillón, S. Do Graphene Oxide Nanostructured Coatings Mitigate Bacterial Adhesion? *Environ. Sci. Nano* 2019, *6* (9), 2863–2875. https://doi.org/10.1039/c9en00499h.

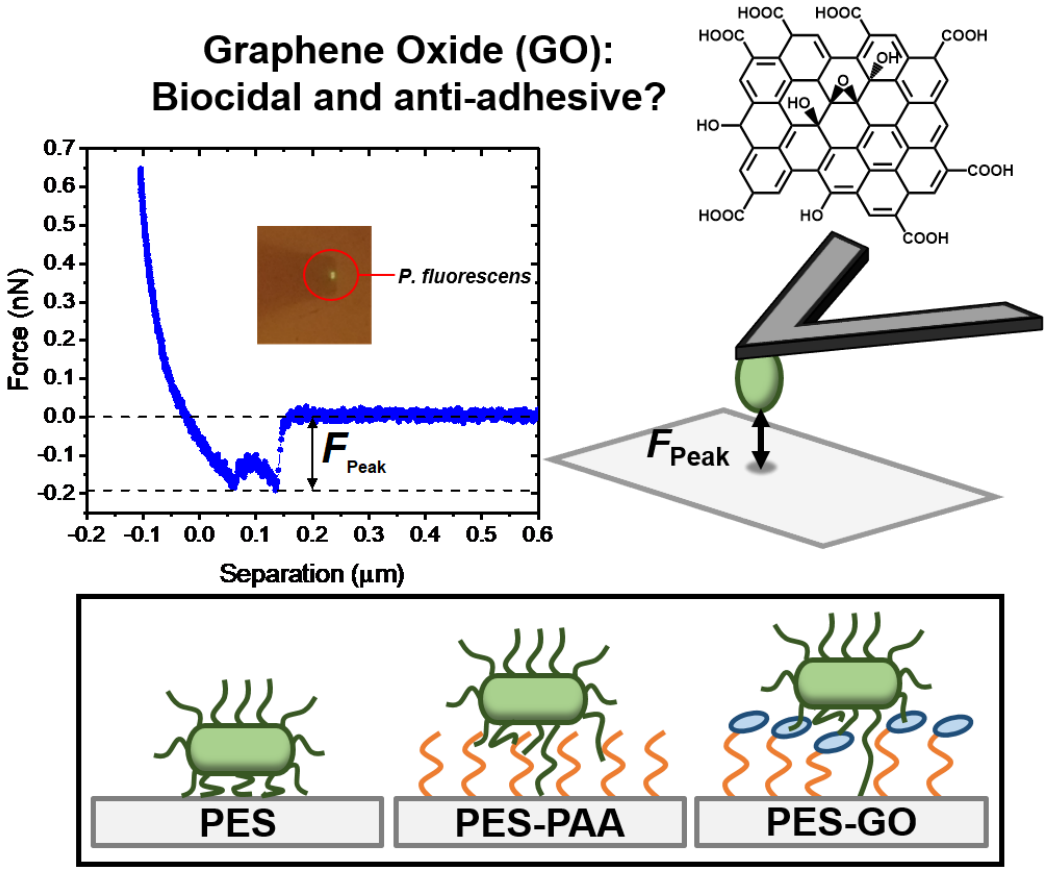

3.1 Summary

Given its potent biocidal properties, graphene oxide (GO) holds promise as a building block of anti-microbial surfaces, with numerous potential environmental applications. Nonetheless, the extent to which GO-based coatings decrease bacterial adhesion propensity, a necessary requirement of low-fouling surfaces, remains unclear. Here we use AFM-based single-cell force spectroscopy (SCFS) to show that coatings comprising GO nanosheets bonded to a hydrophilic polymer brush, mitigate adhesion of *Pseudomonas fluorescens* cells. We demonstrate low-adhesion GO coatings by grafting poly(acrylic acid) (PAA) to polyethersulfone (PES) substrates via self-initiated UV polymerization, followed by edge-tethering of GO to the PAA chains through amine coupling. We characterize the chemistry and interfacial properties of the unmodified PES, PAA-modified (PES-PAA), and GO-modified (PES-GO) substrates using ATR-FTIR, Raman spectroscopy, contact angle goniometry, and AFM to confirm the presence of PAA and covalently bonded GO on the substrates. Using SCFS we show that peak adhesion force distributions for PES-PAA (with mean adhesion force $\overline{\boldsymbol{F}}$Peak = -0.13 nN) and PES-GO ($\overline{\boldsymbol{F}}$Peak = -0.11 nN) substrates are skewed towards weaker values compared to the PES control ($\overline{\boldsymbol{F}}$Peak = -0.18 nN). Our results show that weaker adhesion on PES-GO is due to a higher incidence of non-adhesive (repulsive) forces (45.9% compared to 22.2% over PES-PAA and 32.3% over PES), which result from steric repulsion afforded by the brush-like GO-PAA interface. Lastly, we show that attachment to the various substrates is due to interactions of proteinaceous adhesins whose force response is well described by the worm-like chain model of polymer elasticity.

3.2 Introduction

The discovery of graphenic nanomaterials (GNMs, such as graphene, graphene oxide and reduced graphene oxide)[179] in 2004 unleashed a scientific revolution due to their unique physical and chemical properties, leading to numerous potential applications in water treatment and wastewater reuse.[180] The high specific surface area (~2,630 m^2 g^{-1})[181] and single-atom-thickness of GNMs could enable them as membrane materials[182–184] and adsorbents for the removal of water contaminants.[185] Moreover, the thermal properties displayed by graphene (i.e., its ability to harvest sunlight and increase the local temperature above the boiling point of water[186]), and graphene's high electron mobility (up to 2×10^5 cm^2 V^{-1} s^{-1})[181], could enable electrochemical and solar-driven water purification and disinfection.

The specific application addressed by the present work concerns graphene oxide (GO)-based biocidal coatings.[187,188] Given their wide-spectrum antimicrobial activity[189–192], GO nanosheets are being explored as building blocks of antimicrobial surfaces, aiming to inactivate water-borne bacteria and mitigate biofilm formation. In recent studies, GO has been incorporated into the polymeric matrix of polyamide membranes,[23,193–195] or covalently bonded to membrane surfaces.[196,197] Nevertheless, the underlying mechanism of bacterial adhesion to GO-functionalized interfaces – the crucial first step of biofilm formation[198] – continues to be poorly understood. Moreover, recent studies have observed that GO functionalization of inorganic and polymeric substrates can increase their bio-adhesiveness.[199,200] The possible adverse modification of interfacial properties challenges the notion of GO films as anti-biofouling coatings. This question needs to be addressed

since the effectiveness of GO as a biocidal nanomaterial will be compromised if it increases the adhesiveness of a given substrate vis-à-vis bacterial cells.

In a recent study,[199] we reported that the nanoscale morphology of GO coatings significantly influences bacterial adhesion, with edge-tethered GO showing weaker adhesion forces compared to immobilized layers of horizontally arranged GO nanosheets; spatial arrangement and conformational disorder of the GO building blocks thus seem essential to realize both biocidal activity and low adhesion propensity. Here, we investigate the extent to which GO coatings, comprising GO nanosheets edge-tethered to a polymer brush, are capable of mitigating bacterial adhesion. We surmise that the combination of hydrophilicity and conformational disorder afforded by the GO-functionalized polymer brush is essential to mitigate bioadhesion. To test this hypothesis, we use self-initiated UV polymerization of acrylic acid to graft poly(acrylic acid) (PAA) to polyethersulfone (PES) substrates, tethering GO nanosheets to the PAA chains. We then explore the interfacial properties of the GO coatings using atomic force microscopy (AFM)-based single-cell force spectroscopy[119], whereby a single *Pseudomonas fluorescens* cell (a Gram-negative, biofilm-forming bacterium[104,111]) is immobilized on an AFM cantilever, enabling investigation of bacterial adhesion with nanoscale resolution. We show that microbial adhesion to GO-functionalized substrates is weakened compared to the GO-free control substrates. Consistent with our AFM results, bacterial deposition experiments show that GO-functionalized substrates mitigate adhesion under dynamic conditions. Characterization of the surface interfacial properties suggests that weaker adhesion on GO-

modified substrates is a consequence of steric repulsive forces derived from the GO layer, edge-tethered to PAA brushes.

This paper is organized as follows. In section 3.3 we describe the substrate modification protocols, and the techniques employed to characterize interfacial properties. Results and discussion are given in section 3.4. We close with concluding remarks in section 3.4.

3.3 Materials and Methods

3.3.1 GO Functionalization

Substrates All coatings investigated were formed on polyethersulfone (PES) substrates. To this end, commercially available PES ultrafiltration (UF) membranes were used (30 kDa molecular weight cutoff; Synder Filtration, Vacaville, USA). PES substrates were soaked in 50% glycerin solution and stored at 4 °C. Prior to use, substrates were rinsed with ultrapure (UP) water (18.2 MΩ cm, Barnstead, Thermo Fisher), soaked in 25 vol.-% aqueous isopropanol for 24 hours, and thoroughly rinsed again with UP water to remove residual preservatives.

Poly(acrylic acid) Grafting We used self-initiated UV graft polymerization to grow poly(acrylic acid) (PAA) on PES.[201–205] PAA chains were subsequently used to functionalize substrates with GO. A schematic diagram of the surface modification protocol is given in **Figure 3. 1.** An aqueous acrylic acid (AA) solution (10 vol.-%) was prepared from a 99% AA stock solution (Sigma Aldrich) with UP water. PES coupons (9 × 14 cm^2) were attached to PTFE frames with a holding volume of 112 mL. The PES substrates and the AA solution were brought to a glove box, from which oxygen had been

purged to a concentration < 500 ppm. The solution and the substrates were left to equilibrate with the atmosphere inside the glove box for 15 minutes to lower the dissolved oxygen concentration in the AA monomer solution. Next, 10 vol.-% AA solution was poured over the PES (affixed to the PTFE frame) and allowed to soak the PES substrate. After 15 minutes, excess AA solution was removed, leaving a thin liquid film of AA monomer solution on the surface (**Figure 3. 1. (a)**). Ensuring that the monomer solution is cast as a thin film increases UV penetration depth, thus accelerating the polymerization kinetics on the substrate. Subsequently, the AA-soaked PES surface was irradiated with a UV lamp (Spectroline Model EF-160C) positioned ~2 cm above the substrate for times ranging from 10 to 60 seconds. After irradiation, the substrate was rinsed thoroughly and soaked in UP water for 24 hours to remove unreacted monomers. This step resulted in PAA-functionalized PES substrates (**Figure 3. 1. (b)**), which hereinafter we designate as PES-PAA.

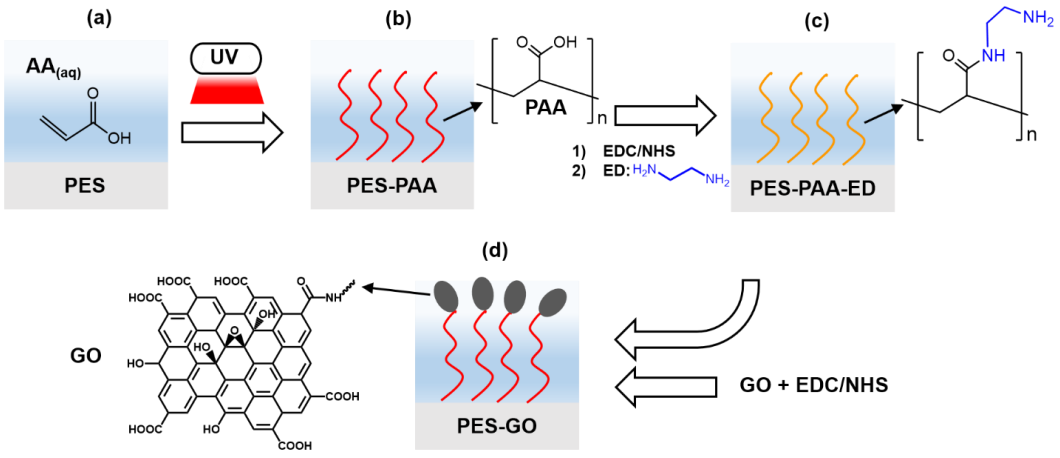

Figure 3. 1. Schematic diagram of polyethersulfone (PES) surface modification with graphene oxide (GO). (a-b) Self-initiated UV polymerization results in growth of poly(acrylic acid) (PAA) chains from acrylic acid (AA) monomers in aqueous solution, yielding PES-PAA substrates. (c) EDC/NHS-mediated amine coupling binds ethylenediamine (ED) linkers to the PAA chains, resulting in PES-PAA-ED substrates. (d) EDC/NHS-activated GO nanosheets react with primary amines in the ED linker to covalently tether GO to the substrates (yielding PES-GO substrates).

Substrate Functionalization with GO Single-layer graphene oxide (GO) was purchased from Cheap Tubes (Grafton, VT, USA). Characterization by AC mode AFM revealed an average nanosheet thickness of 0.8 ± 0.1 nm, consistent with single sheets,[199] and sub-micron lateral dimensions (**Figure B. 1. (a) and (b)**) in agreement with the manufacturer's specifications (i.e., 300-800 nm). A negative zeta potential was observed over the pH range ~1.5-9 for GO in aqueous dispersion (**Figure B. 1. (c)**) (consistent with previous work[206]), indicative of deprotonation of carboxylic acid groups in the nanosheet edges.[188] The oxygen content of GO was 35-45%, per the manufacturer's specifications. The Raman spectrum of GO nanosheets deposited on a silicon wafer (**Figure B. 1. (d)**) exhibited the D (~1350 cm^{-1}) and G (~1590 cm^{-1}) bands characteristic of GO.[207] Substrates were functionalized with 250 µg mL^{-1} GO dispersions prepared from 2 mg mL^{-1} stock dispersions, which were rendered colloidally stable through bath sonication for 24 hours. PES-PAA substrates were functionalized with GO by adapting the procedure developed by Perreault et al.,[196] which is based on amine coupling.[208] Carboxylic acid functional groups in the grafted PAA chains were activated to amine-reactive esters with 4 mM 1-ethyl-3-(3-dimethylaminopropyl)carbodiimide hydrochloride (EDC, 98%, Sigma) and 10 mM *N*-hydroxysuccinimide (NHS, 98%, Sigma), buffered at pH 5 with 10 mM MES (BioXtra, Sigma) supplemented with 0.5 M NaCl. The EDC-NHS activation step was carried out for 60 minutes under ambient conditions on a benchtop shaker at 30 rpm. Substrates were then rinsed gently with UP water. The amine reactive esters on the PES-PAA surface were subsequently contacted with 10 mM ethylenediamine solution (ED, BioXtra, Sigma) buffered at pH 7.5 by 10 mM HEPES (99.5%, Sigma) with 0.15 mM NaCl. The ED amine coupling step proceeded for 30 minutes, resulting in PES-PAA-ED substrates, as shown

schematically in **Figure 3. 1. (c)**. Next, the carboxylic acid functional groups decorating the GO nanosheet edges[188] were activated to amine reactive esters in a similar way. A GO dispersion (10 parts, 250 μg mL^{-1}) was mixed with 2 parts 100 mM MES buffer, followed by 1.75 parts 20 mM EDC in 10 mM MES buffer, and 1.75 parts 50 mM NHS in 10 mM MES buffer. The pH of the solution was then lowered to 5.5 by addition of 1 M HCl dropwise (to minimize flocculation of GO nanosheets), and allowed to react for 15 minutes. Subsequently, the pH was raised to 7.2 by addition of 1 M NaOH dropwise. The GO dispersion was poured over the ED-functionalized surface (PES-PAA-ED), covered, and allowed to react for 1 hour on a benchtop shaker at 30 rpm. Reaction between the amine-reactive esters in GO and the primary amine groups on the surface of the ED-modified substrate resulted in covalent linkage of the GO nanosheets to produce PES-GO substrates **Figure 3. 1. (d)**. Finally, PES-GO samples were thoroughly rinsed and sonicated for 5 minutes to remove non-covalently bonded GO. All substrate samples were stored in ultrapure water at 4 °C for up to 3 weeks until use.

3.3.2 Interfacial Characterization Techniques

Raman and Fourier-Transform Infrared Spectroscopy (FTIR) Attenuated total reflectance (ATR) FTIR was used to characterize the surface chemistry of the substrates. Spectra of desiccator-dried specimens of each substrate type were acquired in an FTIR spectrometer (Nicolet Series II Magna-IR System 750) equipped with an ATR cell. The spectra were collected in terms of % reflectance at a resolution of 0.241 cm^{-1}. Raman spectra were obtained with an Alpha300R Raman microscope (Witec). For each specimen, we acquired 20 × 20 μm^2 Raman scans at a 0.5 μm resolution, on randomly chosen sections of the substrates. At each point in the 2D scan, we computed the ratio of the area under the D

band of GO (observed at 1350 cm^{-1})[207] and the area under a prominent PES peak (observed at 1146 cm^{-1}) to generate maps characterizing the spatial distribution of GO nanosheets. In addition, a mean Raman spectrum was generated by averaging the spectra collected at each point on the 2D scan.

Contact Angle, Surface Charge, and Nanoscale Roughness Substrate hydrophobicity was characterized in terms of oil-in-water contact angle measurements using the captive bubble technique. We performed measurements with a Ramé-Hart Model 200 goniometer; images were analyzed with the DROP Image software (Ramé-Hart). For captive bubble measurements, substrates were affixed to a surface with the functionalized side facing a liquid cell containing ultrapure water. A J-shaped needle was used to inject *n*-decane droplets (~10 μL). We performed ≥ 14 contact angle measurements across three independently functionalized specimens of each substrate type. The surface charge of the substrates was characterized *via* streaming potential measurements using an electrokinetic analyzer (SurPass, Anton-Paar) equipped with an adjustable gap cell at a gap size of 120 μm. Streaming potential was measured from pH 10 to pH 4 in 1 mM KCl solution, and the zeta potential was determined from the streaming potential using the Smoluchowski-Helmholtz equation.[209] Three specimens of each substrate type were characterized. The nanoscale roughness of the substrates was investigated with an MFP-3D-Bio AFM (Asylum Research) equipped with a liquid cell. AC mode AFM scans (5 × 5 μm^2, scan rate = 0.25 Hz) of two specimens of each substrate type were obtained in phosphate-buffered saline (PBS) at pH 7.4 using a silicon nitride cantilever (SNL probe "C", nominal k = 0.24 N m^{-1}, Bruker). Surface topography was quantified in terms of the root-mean-squared

roughness (R_{RMS}) determined in 1 × 1 μm^2 areas of each of the AFM scans for a total of 8 roughness calculations for each substrate type.

3.3.3 Single-Cell Force Spectroscopy (SCFS)

The adhesion of *P. fluorescens* cells to the surface of control and functionalized substrates was quantitatively investigated using single-cell force spectroscopy (SCFS). Bacterial cells were grown and cultivated following the protocol provided in the Electronic Supplementary Information (ESI). The experimental procedure of SCFS, outlined below, is provided in detail in our recent publication.[72] An individual *P. fluorescens* (ATCC 13525) cell was adhered to a tip-less AFM cantilever (MLCT-O10 probe "C", nominal k = 0.01 N m^{-1}, Bruker) on which a polydopamine wet adhesive layer had been deposited from a dopamine hydrochloride solution (4 mg of dopamine hydrochloride per milliliter of Trizma buffer, pH 8.5) shortly before adhering the cell. The cell was adhered with its long axis parallel to the leading edge of the cantilever, an orientation that maximizes adhesion contact area. Bacterium orientations probing adhesion via the flagellar pole were not studied, due to the risk of cell detachment during force collection. An MFP-3D-Bio AFM (Asylum Research) integrated to a Zeiss Axio Observer A1 inverted optical microscope was used to perform cell adhesion force measurements. All forces were determined at room temperature (25 °C) in a liquid cell filled with PBS, pH 7.4. Force curves, comprising extension-retraction cycles, were carried out at a cantilever speed of 400 nm/s, a piezo dynamic range of at least 3 μm, a trigger force (the maximum force applied to the cell as it contacts the substrate) of 600 pN, and a dwell time of 0 s (i.e., the bacterial cell was immediately retracted from the substrate upon reaching the trigger force). For each

substrate type, a total of ≥ 98 force curves were collected with at least 2 independently cultivated bacterial cells, on ≥ 2 different substrate specimens of each type. Force curves were acquired at randomly chosen sites on the substrate. At each randomly chosen location, up to three force curves were collected to minimize deposition of extracellular polymeric substances on the substrate. After each experiment, the cell viability was determined using a live/dead assay (BacLight, Thermofisher). Only data collected with a live cell that remained at its initial location were reported.

3.3.4 Statistical Analysis

Unless stated otherwise, two-sided unpaired *t*-tests, presuming unknown but equal population variances (i.e., assuming homoscedasticity), were conducted to determine the statistical significance of the results.

3.4 Results and Discussion

3.4.1 Interfacial Characterization

We used an array of surface analytical techniques to characterize the chemistry and morphology of the various substrates.

Surface Chemistry Given the prominent IR bands present in the AA monomer, we used FTIR spectroscopy to assess the efficacy of PAA grafting. AA polymerizes on the substrate due to UV-generated free radicals formed on the PES surface, which react with the vinyl double bond of the AA molecule, leading to the formation of PAA chains covalently bonded to the substrate.[203] The degree of grafting (i.e., the extent of AA polymerization on

the PES substrate), and the kinetics of polymerization, are influenced by the UV irradiation time and UV wavelength.[203,210] PES substrates soaked with a thin liquid film of 10 vol.-% AA solution were exposed to UV light for 10-60 seconds. The FTIR results for the PES control and PES-PAA substrates are shown in **Figure 3. 2.** The peak at 1580 cm^{-1}, observed in all samples, is due to vibration of the aromatic rings in PES.[211] In addition, we observe IR bands resulting from carboxylic acid groups in PAA, namely a peak at 1700-1730 cm^{-1} due to C=O stretching vibration,[212] and multiple bands in the 2500-3300 cm^{-1} range due to COO-H stretching.[212] These peaks increase monotonically with irradiation time, in line with increasing degree of PAA grafting.[210] In the remainder of the study we focus on substrates fabricated with a 10-s UV irradiation step, which resulted in materials with nanofiltration-like water permeability coefficient and divalent ion rejection (see **Appendix B** for methods and results). Irradiation times > 10 s resulted in a dense PAA layer and a steep loss in water permeability.

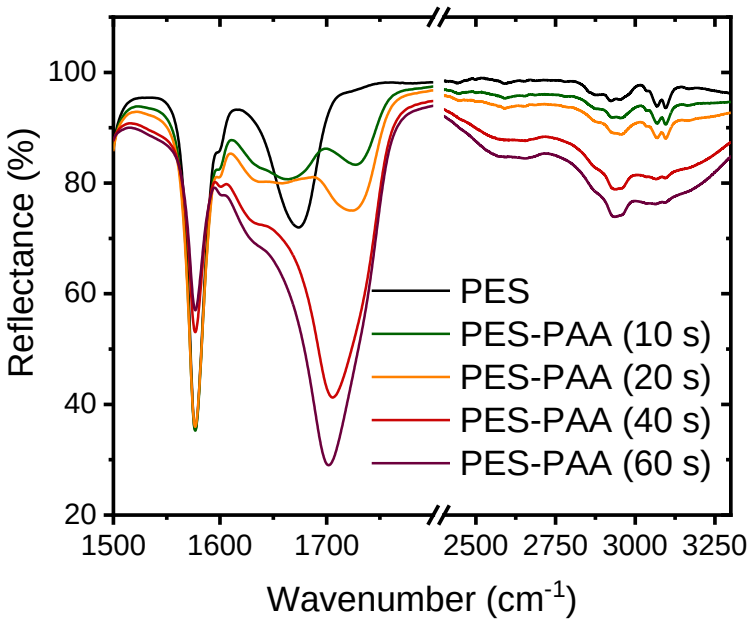

Figure 3. 2. FTIR spectra of PES and poly(acrylic acid) (PAA)-functionalized PES substrates (PES-PAA, prepared with different UV irradiation times noted in the caption).

The FTIR spectra of the PES, PES-PAA (10-s UV irradiation) and PES-GO substrates are presented in **Figure 3. 3.** The spectrum corresponding to PES-GO shows an increase in the COO-H stretching band at 3300 cm^{-1} relative to PES-PAA, which can be attributed to carboxylic acid functional groups present in the GO nanosheet edges.[188] In addition, PES-GO presents a peak at ~2900 cm^{-1} absent in the other substrates, which is likely an N-H stretching vibration band (typically observed at 3100-3500 cm^{-1} [212]) due to primary amines that remain unreacted after GO modification.

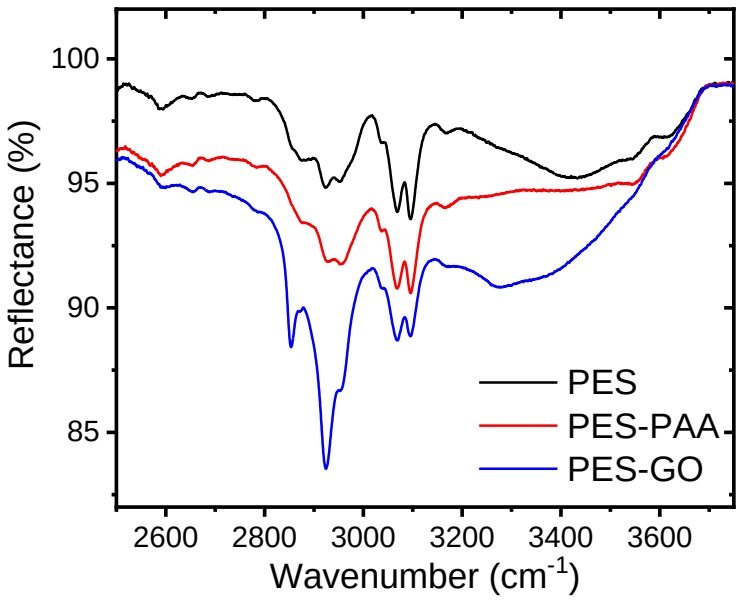

Figure 3. 3. FTIR spectra of control (PES), poly(acrylic acid) (PAA)-functionalized PES (PES-PAA, 10-s UV irradiation), and GO-functionalized (PES-GO) substrates.

We confirmed the presence of graphene oxide on the PES-GO substrates using Raman spectroscopy. The average of 1600 spectra scanned over a 20 × 20 μm^2 area of each specimen is presented in **Figure 3. 4.** The PES-GO substrate prominently shows the G and D bands of graphene oxide,[207] thus confirming functionalization of PES with GO. All substrates show similar chemical signatures due to polyethersulfone, e.g., peaks at 790, 1070, 1107, 1146, 1580 and 1601 cm^{-1}.[213]

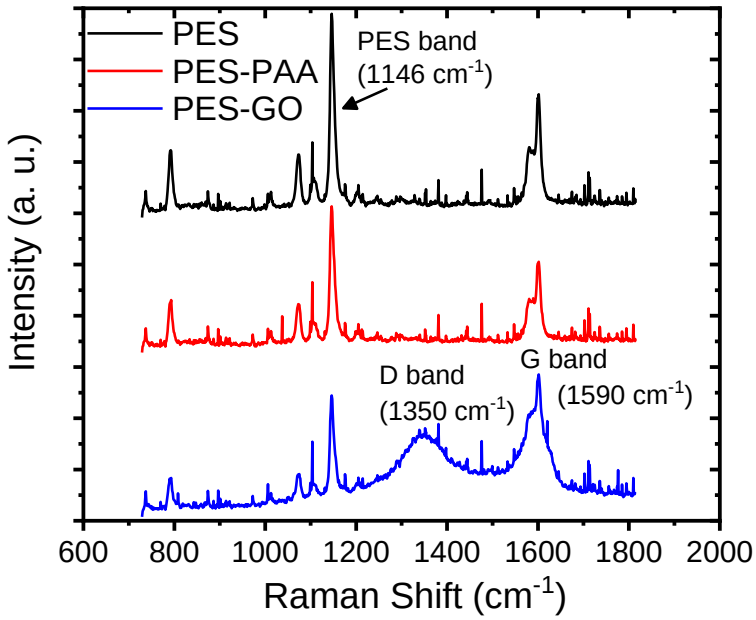

Figure 3. 4. Raman spectra of pristine PES, poly(acrylic acid) (PAA)-functionalized PES (PES-PAA), and GO-modified PES (PES-GO) substrates.

We used confocal Raman mapping to assess the spatial distribution of GO on the PES-GO substrates. The results are presented in **Figure 3. 5. .** The PES-GO map (**Figure 3. 5. . (c)**) exhibits high brightness regions indicative of the presence of GO nanosheets throughout the scanned area (the intensity of each pixel is proportional to the ratio of the area under the D peak of GO to that under the polyethersulfone peak at 1146 cm^{-1}). Conversely, neither the PES nor the PES-PAA Raman maps (**Figure 3. 5. . (a-b)**) exhibit signatures of GO.

The data in **Figure 3. 5. .** consequently show that the modification protocol enables the formation of uniform layers of tethered GO nanosheets on the PES substrates.

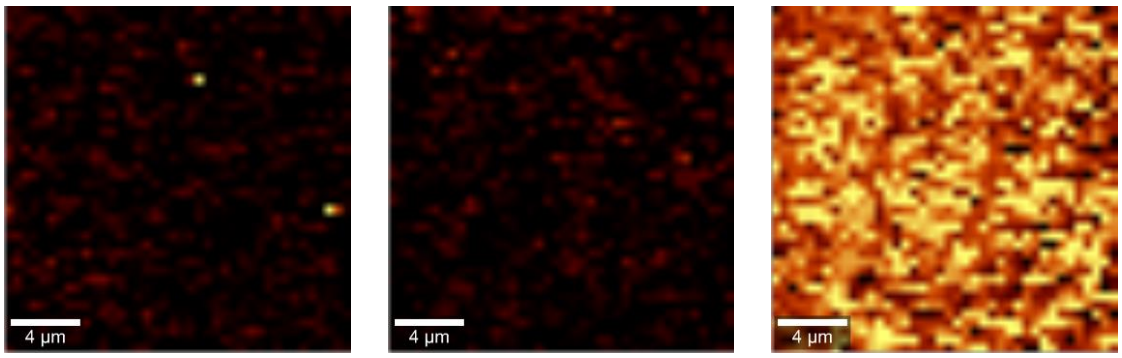

(a) (b) (c)

Figure 3. 5. Raman spectroscopy maps of (a) pristine PES, (b) poly(acrylic acid) (PAA)-modified PES (PES-PAA), and (c) GO-modified PES (PES-GO) substrates.

Interfacial Properties We investigated the interfacial properties which are known to influence biofouling propensity: hydrophobicity, nanoscale roughness and surface charge.[214,215] To characterize the hydrophobicity of each substrate type, we measured the contact angle of *n*-decane droplets in aqueous suspension using the captive bubble technique. The angles shown below are measured from the substrate, through the aqueous phase, to the *n*-decane interface, so that smaller values indicate poor wetting of the substrate by the *n*-decane droplet (i.e., greater hydrophilicity). The results, presented in **Figure 3. 6(a)**, show that PES-PAA ($\theta_{n\text{-Decane}} = 20.6 \pm 4.3°$) and PES-GO samples ($\theta_{n\text{-Decane}} = 19.7 \pm 5.4°$) are significantly more hydrophilic ($p < 0.01$) than the control PES substrate ($\theta_{n\text{-Decane}} = 53.1 \pm 3.9°$). PES-PAA and PES-GO showed approximately equal contact angles ($p = 0.6$). We attribute the low wettability of PES-AA and PES-GO surfaces by a hydrophobic liquid (*n*-decane) to the abundance of H-bonding functional groups in PAA-

and GO-functionalized surfaces (i.e., -COOH groups in PES-PAA; hydroxyl, and -COOH groups in GO,[188] all of which are absent in PES).

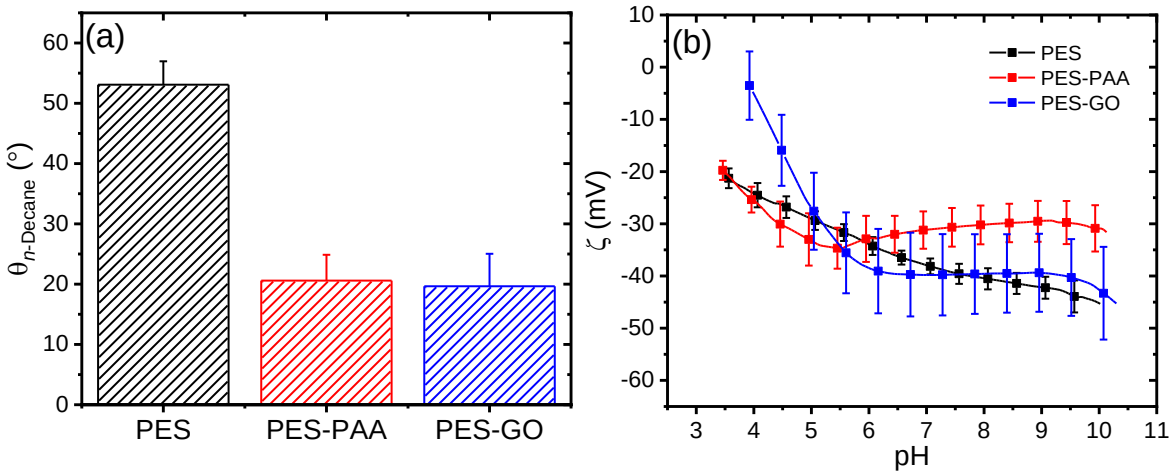

Figure 3. 6. (a) Contact angles of n-decane droplets (θ_n-Decane) on the various substrates, determined in ultrapure water via the captive bubble technique. Error bars denote one standard deviation ($n \geq 14$). (b) ζ-Potential as a function of pH of pristine PES, poly(acrylic acid) (PAA)-modified PES (PES-PAA), and GO-modified PES (PES-GO) substrates. The ζ-potential results shown for each substrate type are the average of three independently modified specimens (error bars indicate one standard deviation.

We characterized the surface charge of the substrates in terms of the ζ-potential as a function of pH. The results are presented in **Figure 3. 6. (b)**. All substrates (including pristine PES[216]) exhibited negative zeta potentials over the pH range investigated. At pH 7.4, (i.e., the condition at which we characterized other interfacial properties such as surface roughness, and microbial adhesion), all specimens show a similar zeta potential value of ~-30 to -40 mV, suggesting that surface functionalization does not significantly modify the charge of the interface at this pH. PES-PAA and PES-GO samples are negatively charged primarily due to deprotonation of carboxylic acid groups with increasing pH.[188,206] While PES does not have acidic functional groups, its negative zeta potential is due to adsorption of hydroxyl ions.[49]

Surface roughness influences fouling, with rougher substrates exhibiting greater biofouling and colloidal fouling propensity.[217–220] We determined the RMS roughness (R_{RMS}) of the hydrated substrates using AFM. Representative 2 × 2 μm^2 AFM scans along with average R_{RMS} values are shown in **Figure 3. 7.** We observed a relatively smooth interface in the PES substrate with low surface roughness (R_{RMS} = 2.51 ± 0.49 nm, cf. **Figure 3. 7. (a)**). On the other hand, the grafted PAA chains increase the R_{RMS} of the PES-PAA substrate (R_{RMS} = 5.74 ± 2.18 nm, cf. **Figure 3. 7. (b)**) compared to the PES control ($p < 0.01$). The negatively charged tethered PAA chains exist in a collapsed (i.e., non-extended) conformation given that the high ionic strength of PBS (162 mM) results in screening of electrostatic repulsions.[221] PAA chain collapse yields the rough, peak-and-valley interfacial structure shown in **Figure 3. 7. (b)**. Upon edge-tethering GO nanosheets to the PAA surface, we observe an interface with lower R_{RMS} (R_{RMS} = 3.63 ± 1.17 nm, cf. **Figure 3. 7. (c)**) compared to PES-PAA (p = 0.03). GO nanosheets appear to cover the rougher PAA interfacial features, thus decreasing R_{RMS}. This “smoothing over” is possibly caused

by GO nanosheets tethered to the PAA layer through multiple sites along the sheet periphery (effectively acting as a crosslinker of PAA chains).

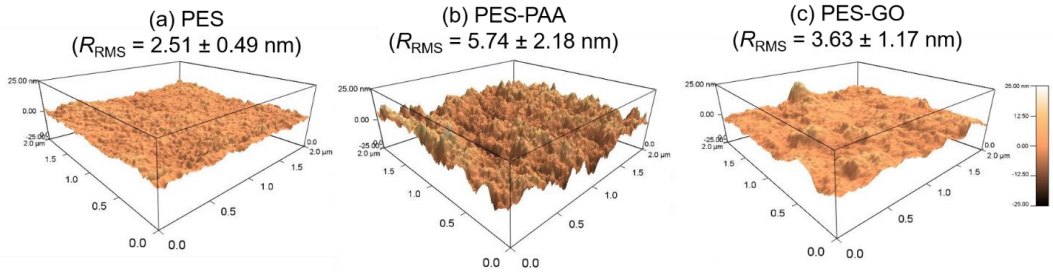

Figure 3. 7. AC mode AFM images of (a) pristine PES, (b) poly(acrylic acid) (PAA)-modified PES (PES-PAA), and (c) GO-modified PES (PES-GO) substrates. The caption denotes the root-mean-squared roughness (RRMS) computed from eight 1 × 1 μm^2 sections sampled over two different 5 × 5 μm^2 scans of each substrate type. AFM scans and RRMS were obtained in PBS (pH 7.4).

3.4.2 Bacterial Adhesion

We now investigate bacterial adhesion onto GO-functionalized substrates. Our aim is to examine whether GO substrate functionalization mitigates bacterial adhesion, the first step in biofouling. GO coatings that are both biocidal and anti-adhesive are preferable to those that afford only bacterial inactivation (without preventing bacteria, and bacterial debris, from adsorbing). While previous work on GO-functionalized polyamide membranes has shown that GO coatings may exert dual biocidal/anti-adhesive functions[197], recent studies have shown that GO nanosheets increase the adhesiveness of inert Si substrates[199] and weakly adhesive polymeric spacer substrates.[200] Here we explain these seemingly contradictory results. Lastly, we elucidate the molecular determinants of adhesion by

analyzing the interactions of bacterial adhesin molecules (proteinaceous structures such as pili and outer membrane proteins[84,86]) with the various substrates.

A representative force-distance curve, showing a typical extension−retraction force cycle, is presented in **Figure 3. 8.** For each retraction force curve, we recorded the peak adhesion force, F_{Peak}, defined as the binding force with the highest magnitude, and the rupture separation, R, i.e., the separation at which cell-substrate forces vanish (cf. **Figure 3. 8.**). We set the trigger force (F_{Tr}, defined as the force exerted on the bacterium when it contacts the substrate, cf. **Figure 3. 8.**), to 600 pN; this value is of the same order of magnitude as the permeation drag force experienced by similarly-sized colloidal particles during low-pressure membrane filtration.[222]

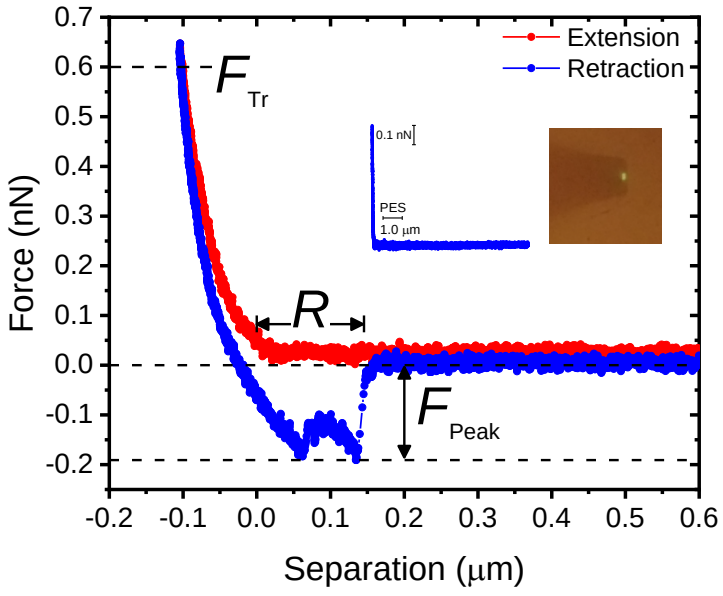

Figure 3. 8. Representative extension-retraction force cycle recorded over PES with a *P. fluorescens* bacterial probe. The curve shows the definition of the trigger force (F_{Tr}), peak adhesion force (F_{Peak}), and rupture separation (R). The inset shows a representative non-adhesive retraction force curve recorded over PES, and a digital image of a bacterial probe

Figure 3. 9. (a-c) presents the distribution of *P. fluorescens* peak adhesion forces (F_{Peak}) observed over the different substrates. The "NO" column in the histograms corresponds to measurements in which weak adhesion (< 30 pN, equivalent in magnitude to the noise level in the force) or no adhesion peaks were observed (see **Figure 3. 8.** (inset) for a representative non-adhesive force curve).

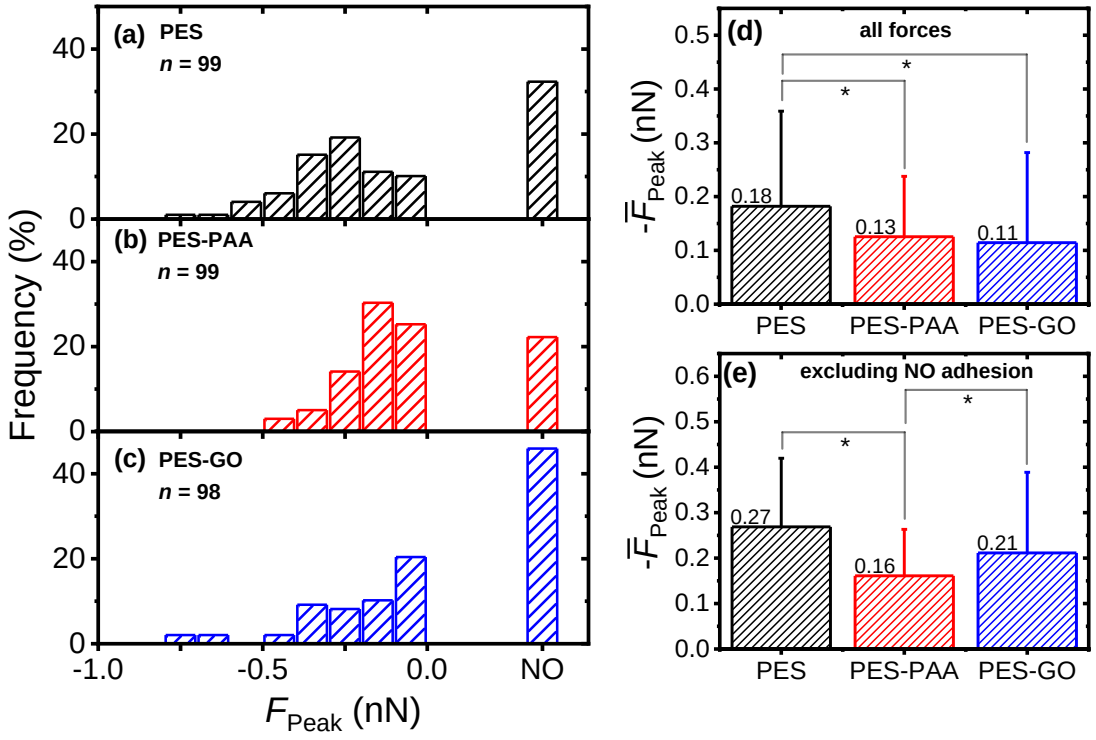

Figure 3. 9. Distribution of peak adhesion forces (F_{Peak}) of single *P. fluorescens* cells on: (a) pristine PES; (b) poly(acrylic acid) (PAA)-modified PES (PES-PAA); (c) GO-modified PES (PES-GO). The inset shows the number of force measurements (n). Measurements were performed in PBS at pH 7.4. (d) Mean peak adhesion forces ($\bar{F}_{Peak}$) computed from (a)-(c), including non-adhesive events (F_{Peak} = 0 nN). (e) Mean peak adhesion forces excluding non-adhesive events. Error bars in (d) and (e) indicate the standard deviation. Pairwise comparisons denoted by * indicate statistical significance ($p < 0.05$).

We observe a broad distribution of peak adhesion forces for all substrates (cf. **Figure 3. 9. (a) – (c)**), with the majority of adhesion events occurring in the ≈ 0 to 0.5 nN range, typical of bacterial adhesion.[84] Further, we observe that adhesion forces are substrate-dependent. Among the surfaces studied, PES-GO exhibits the lowest probability of adhesion, with

45.9% of measurements showing no-adhesion events, compared to 22.2% for PES-PAA and 32.3% for PES. The observation of three consecutive non-adhesive force curves was reproducible in 15% (PES-PAA), 21% (PES), and 25% (PES-GO) of the loci probed, i.e., a similar trend to that of the probability of observing non-adhesive events across the whole surface. Consistent with the (quasi-static) AFM measurements, bacterial deposition experiments (**Figure B. 2.**) show that the extent of irreversible adhesion is lowest on PES-GO. **Figure 3. 9. (d)**, presenting the average of all forces ($\bar{F}_{\text{Peak}}$), shows that adhesion is strongest on PES, while PES-GO displays the weakest mean adhesion: $\bar{F}_{\text{Peak}}$ = -0.11 (± 0.17) nN for PES-GO vs. -0.18 (± 0.18) nN for PES (p = 0.006). PES-PAA substrates also demonstrated weaker adhesions ($\bar{F}_{\text{Peak}}$ = -0.13 (± 0.11) nN) compared to PES (p = 0.008), while similar adhesiveness was displayed by PES-PAA and PES-GO (p = 0.6).

A more nuanced adhesion behavior arises when we exclude the non-adhesive measurements from the calculation of the mean. The results, presented in **Figure 3. 9. (e)**, show that PES substrates still reveal the strongest mean adhesion, i.e., $\bar{F}_{\text{Peak}}$ = -0.27 (± 0.15) nN. On the other hand, PES-PAA exhibits the weakest mean adhesion forces with $\bar{F}_{\text{Peak}}$ = -0.16 (± 0.10) nN, compared to -0.21 (± 0.18) nN for PES-GO (p = 0.04). Consequently, **Figure 3. 9.** shows that, while PES-GO surfaces display the lowest probability of *P. fluorescens* attachment (i.e., highest incidence of non-adhesion events, as shown in **Figure 3. 9. (c)**, adhering bacteria engage the GO substrate with forces that are stronger than those observed over PES-PAA, and only somewhat weaker than those observed over PES (**Figure 3. 9. (e)**).

The picture emerging from **Figure 3. 9.** indicates that edge-tethering GO to a PAA coating decreases the mean adhesion force ($\bar{F}_{\text{Peak}}$) of *P. fluorescens* compared to the unmodified PES surface (cf. **Figure 3. 9. (d)**). However, it is important to note that the lower $\bar{F}_{\text{Peak}}$ observed on PES-GO (**Figure 3. 9. (d)**) is due to a high incidence of non-adhesive events on the GO-functionalized substrate (cf. **Figure 3. 9. (c)**), which offsets the relatively strong adhesion forces exhibited by cells that do successfully adhere to the PES-GO surface (**Figure 3. 9. (e)**).

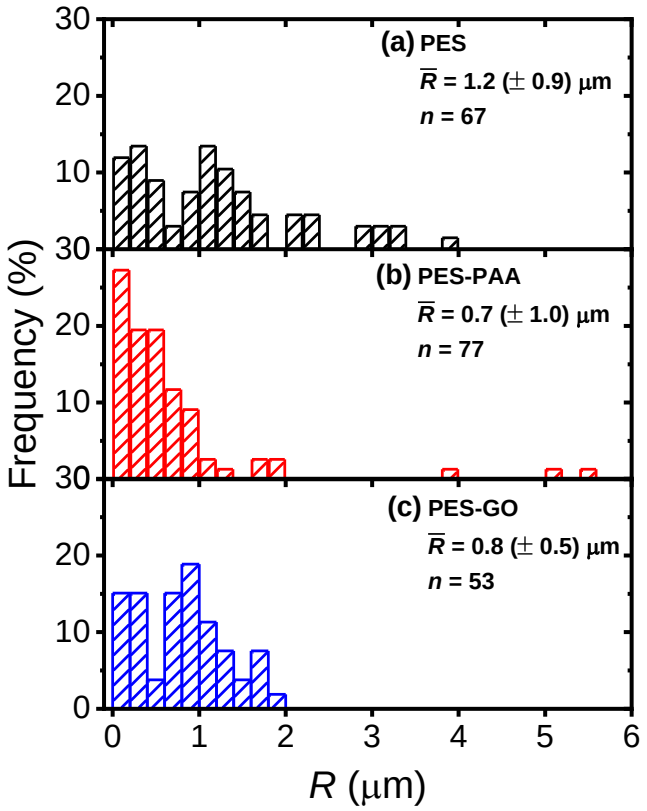

Figure 3. 10. Distribution of rupture separations (R), defined as the distance at which cell adhesion forces vanish, for various substrates: (a) pristine PES; (b) poly(acrylic acid) (PAA)-modified PES (PES-PAA); (c) GO-modified PES (PES-GO). The inset shows the histogram average ($\bar{R}$ (± standard deviation)), and number of measurements (n). Measurements were performed in PBS at pH 7.4.

Figure 3. 10. presents the distribution of the rupture separation (R) over the different substrates. R is also distributed broadly, with mean values ($\bar{R}$) around 1 μm that are a reflection of the adhesins, namely pili and flagella, that mediate *P. fluorescens* binding to substrates.[50,115,223] **Figure 3. 10.** further shows that longer ranged interactions are observed over PES ($\bar{R}$ = 1.2 (± 0.9 μm)) compared to PES-PAA ($\bar{R}$ = 0.7 (± 1.0 μm), p = 0.002) and to PES-GO ($\bar{R}$ = 0.8 (± 0.5 μm), p = 0.008), suggesting that more sites along individual adhesins bind to the PES substrate. It is also possible that higher $\bar{R}$ observed on the PES substrate indicates that several adhesins of different contour length mediate attachment on PES.[72] R thus displays behavior in line with the adhesion forces reported in **Figure 3. 9. (d)**, since longer ranged forces are observed on more adhesion-prone PES substrates. Moreover, in view of the lower $\bar{R}$ observed over PES-GO and PES-PAA, **Figure 3. 10.** shows that the range of cell adhesion forces is determined by microbial adhesins, and that extension of poly(acrylic acid) chains during cell pull-off does not contribute significantly to R.

We turn to the interfacial properties presented in **Figure 3. 6.** And **Figure 3. 7.** to explain the differences in adhesive behavior among the three substrate types. Weakening of cell-substrate forces in PES-PAA (cf. **Figure 3. 9. (d-e)**) compared to PES is due to the PAA coatings resulting in more hydrophilic substrates (cf. **Figure 3. 6. (a)**), which mitigate adhesion of *P. fluorescens* bacteria reliant on hydrophobic interactions.[50,72,89] In addition, PAA chain compression results in a steric repulsive force that contributes to weaker bioadhesion.[224,225] We note that long-range electrostatic repulsive forces, involving the negatively charged substrate (**Figure 3. 6. (b)**) and bacterium, are absent in PBS (Debye

length = 0.75 nm). We observe two effects upon functionalization with GO. First, an increase in the frequency of non-adhesive events compared to PES and PES-PAA (cf. "NO" column in **Figure 3. 9. (a-c)**), which we attribute to the layer of GO nanosheets that is covalently tethered to PES-PAA; this GO coating lowers the roughness of the interface (cf. **Figure 3. 7.**) thus decreasing adsorption surface area, and results in an additional steric barrier that limits binding of the microbe[199] (similarly, higher surface roughness in PES-PAA explains its lower incidence of non-adhesive events compared to PES). Second, we observe an increase in the mean adhesion force relative to PES-PAA (as shown in **Figure 3. 9. (e)**, which excludes non-adhesive observations). In view of the similar contact angles of PES-PAA and PES-GO (cf. **Figure 3. 6. (a)**), the stronger adhesion on the GO-coated substrate cannot be explained by a macroscopic view of hydrophobicity. At the nanoscale, however, GO is known to be amphiphilic, possessing hydrophilic sheet edges,[188] and basal surfaces featuring hydrophobic graphenic domains.[188,226] These nanoscale hydrophobic regions embedded in GO serve as sorption sites for hydrophobic molecules,[227–229] and thus can bolster microbial adhesion through interactions with hydrophobic adhesins.[115]

Role of Adhesin Molecules in Microbial Adhesion **Figure 3. 11.** and **Figure 3. 12.** discuss the molecular-level determinants of bacterial adhesion. Force measurements on all three substrates exhibit adhesion peaks such as those shown in **Figure 3. 11.**, whose characteristic shape results from stretching and unfolding of single biopolymer molecules.[230] Examination of these extension events can therefore provide additional insight into the role of adhesin molecules, such as pili, outer membrane proteins and lipopolysaccharides, in microbial adhesion.[72] Two models are commonly used to describe

the elasticity of single biopolymers under force: the worm-like chain (WLC) model, which describes the mechanics of protein domains; and the extended freely-jointed chain (FJC) model, known to describe the elasticity of polysaccharide molecules.[102] In our data only a small fraction of extension events (<3%) were well described by the FJC model (see **Figure B. 3.** for representative FJC fits on the three substrates); these rare events are due to the extension of polysaccharides on the surface of the bacterial cell, or stretching of PAA chains (known to exhibit FJC mechanics[231]) on the PES-PAA or PES-GO substrate. On the other hand, WLC extension events are far more common, and we analyze them in detail below. We find that 33% of all force measurements collected on PES and PES-PAA substrates, and 26% of measurements collected over PES-GO, exhibit single-molecule extensions that can be quantitatively described by the WLC model. In the WLC model, the elasticity of macromolecules under tension is given by the following force (F)-elongation (z) equation:

$$F(z) = \frac{k_B T}{4L_p}\left[\left(1 - \frac{z}{L_c}\right)^{-2} + \frac{4z}{L_c} - 1\right] \qquad (3.1)$$

where L_p is the persistence length (a measure of the flexibility of the polymer chain), L_c is the contour length (i.e., the total length of the unraveled polymer chain), k_B is Boltzmann's constant, and T = 298.15 K is the absolute temperature. Non-linear regression of the force-distance data using the WLC model (carried out with the WLC fitting function in IGOR Pro 6.3) results in best-fit L_p estimates (**Figure 3. 12. (a)**) across all substrates with an average value $\bar{L}_p \approx 0.3$ nm, in line with the persistence length of proteins[162,230,232], thus suggesting outer membrane proteins (such as LapA in *P. fluorescens*[84]) as the adhesins mediating microbial attachment.

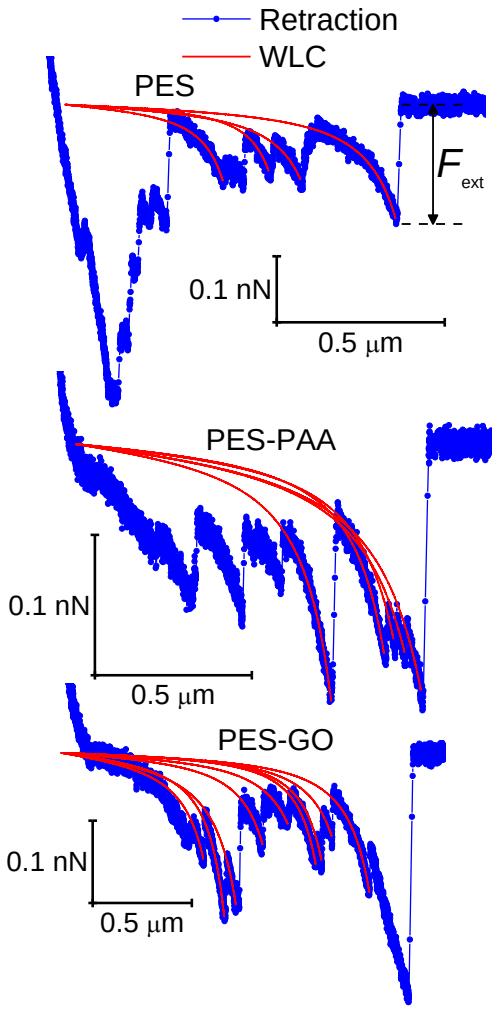

Figure 3. 11. Enlarged view of retraction force curves, showing single-molecule extension events and corresponding worm-like chain (WLC) fits for various substrates, indicated in the caption.

We further observe multiple WLC events in a single force measurement (cf. **Figure 3. 11.**), allowing us to calculate the number of WLC extensions per force curve (N_{WLC}), as shown in **Figure 3. 12. (b)**. While WLC events are observed in fewer PES-GO force curves (26% compared to 33% for the other substrates), the mean values ($\bar{N}_{WLC}$) are similar for PES-GO and PES, i.e., 2.3 ± 2.1 and 2.7 ± 2.2, respectively (p = 0.5). Further PES-PAA exhibits lower $\bar{N}_{WLC}$ (1.4 ± 0.9) compared to PES and PES-GO ($p < 0.05$). Considering that N_{WLC} is proportional to the number of adhesins that attach to the substrate, the values of $\bar{N}_{WLC}$

are consistent with the adhesion properties described previously in **Figure 3. 9. (e)**, which showed that (provided non-adhesive events are excluded) PES and PES-GO showed similar mean adhesion forces.

The single-molecule extension events presented in **Figure 3. 11.** (along with corresponding WLC fits) show the occurrence of consecutive single-molecule extensions. This allows determination of the length scale of the extended biomolecule domains from $\Delta L_c = L_{c,i+1} - L_{c,i}$, where $L_{c,i}$ and $L_{c,i+1}$ denote the contour length of two consecutive WLC fits. As shown in **Figure 3. 12. (c)**, ΔL_c is narrowly distributed around mean values ($\overline{\Delta L_c}$) of 0.10 (± 0.06) μm and 0.11 (± 0.10) μm for PES-PAA and PES-GO, respectively, whereas for PES we observe a much broader distribution with $\overline{\Delta L_c}$ = 0.24 (± 0.18) μm. The tight distribution of ΔL_c around ~100 nm suggests that the WLC events observed on PES-GO and PES-PAA are likely due to proteinaceous adhesins whose domains unravel sequentially in pairs or triplets (the contour length of cell membrane and pilin proteins is 30-60 nm[84,233]), as was recently proposed for *P. fluorescens* adhesins.[84] On the other hand, the much broader distribution observed over PES substrates could be the result of two distinct phenomena. Firstly, desorption of two different adhesin molecules of disparate lengths[50], resulting in two sequential WLC peaks characterized by a large ΔL_c; the longer rupture separation observed on PES compared to the other two surfaces (see **Figure 3. 10.**) supports this mechanism. Alternatively, the more hydrophobic character of PES substrates (**Figure 3. 6.**

(a)) could lead to surface-induced partial unfolding of adhesin molecules[72], the corresponding change in protein conformation leading to a wider range of ΔL_c values.

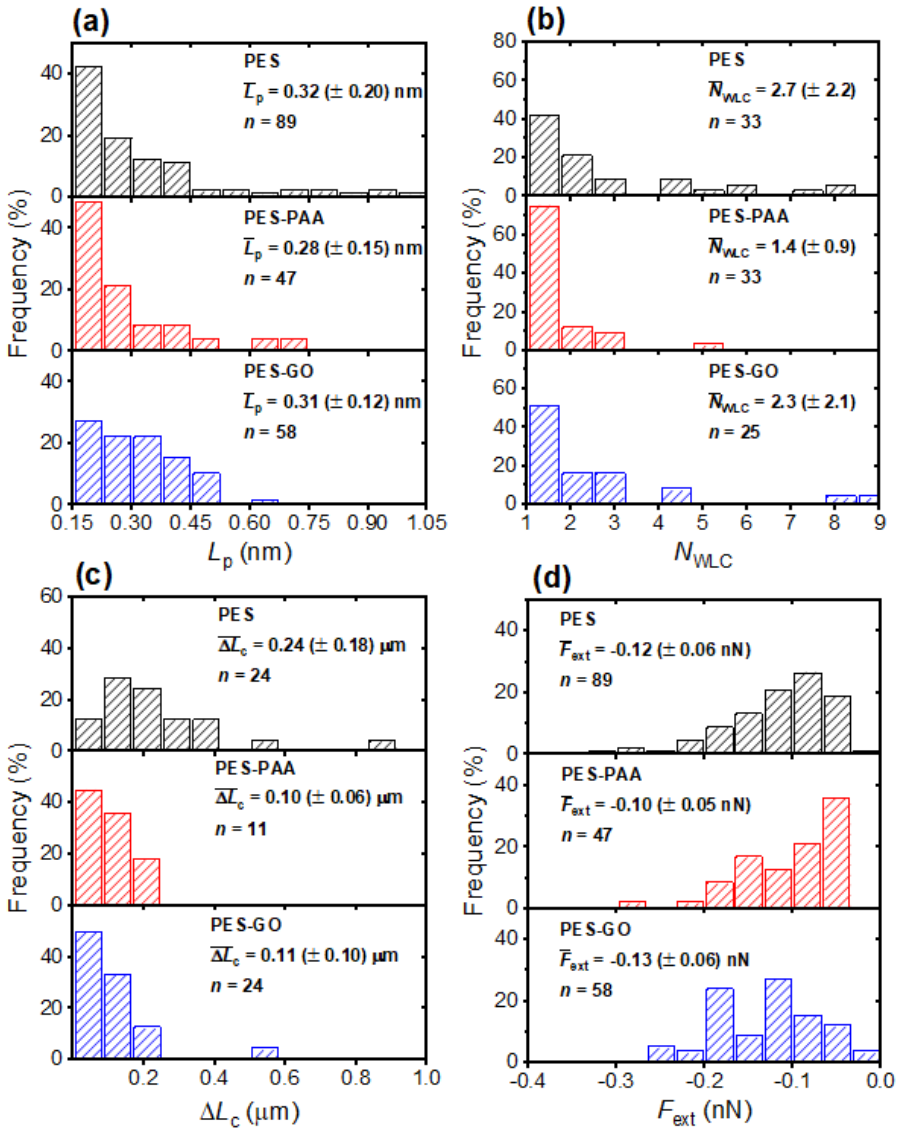

Figure 3. 12. (a) Distribution of best-fit persistence length values (L_p), obtained from WLC model fits on various substrates (see **Figure 3. 11.** for representative fits). (b) Distribution of the number of WLC single-molecule extension events per force curve (N_{WLC}). (c) Distribution of ΔL_c (the difference in contour length (L_c) between two consecutive WLC extension events). (d) Distribution of extension forces (F_{ext}, the force measured at the each WLC extension peak). The caption of each figure indicates the substrate type, histogram average ($\bar{L}_p$, $\bar{N}_{WLC}$, $\overline{\Delta L_c}$, $\bar{F}_{ext}$ (± standard deviation)) and number of measurements (n).

Finally, **Figure 3. 12. (d)** presents the distribution of extension forces (F_{ext}), defined as the force at each peak observed in a single-molecule extension event (cf. **Figure 3. 11.**, top panel). The magnitude of the forces is in the range of 100-300 pN, in agreement with previous reports for unfolding forces of protein domains,[84,230] with the average value ($\bar{F}_{ext}$) being similar for all substrates. This suggests that F_{ext} is primarily due to the elastic response of adhesins to the external force, and that desorption from the substrate does not contribute significantly to the extension force.[230]

3.5 Conclusions

While graphene oxide (GO) has shown strong biocidal activity[190,191,196,234], there have been conflicting reports as to whether GO can mitigate bacterial adhesion,[199,200] the first step of biofilm formation and biofouling. This paper used single-cell force spectroscopy to show that edge-tethering GO nanosheets to poly(acrylic acid) (PAA) brushes produces GO coatings (formed on polyethersulfone (PES) substrates) characterized by low *P. fluorescens* adhesion forces. Our results show that lower mean adhesion forces observed on GO-functionalized coatings (designated PES-GO) are mainly due to the occurrence of cell-substrate repulsive (non-adhesive) forces; these are in turn derived from the hydrophilicity and steric repulsion afforded by the GO-functionalized PAA layer. A salient observation is that GO is not intrinsically anti-adhesive: its integration into a polymeric brush is essential to achieve a low-adhesion interface. GO-free PAA coatings (termed PES-PAA) also demonstrated lower bacterial adhesion due to their hydrophilicity. In the absence of PAA or GO, PES control substrates exhibited stronger bacterial adhesion due to their hydrophobicity. Analysis of the force spectroscopy data on all substrates shows

that adhesion of *P. fluorescens* is driven by proteinaceous adhesins, whose elasticity is well described by the worm-like chain model.

Our results highlight the importance of interfacial properties (e.g., surface roughness, hydrophilicity) in the formulation of GO-based antibacterial interfaces for environmental applications, pointing out possible directions for future study. In the context of water treatment systems, it is necessary to characterize bioadhesion to GO interfaces (such as those in membranes[196,197], spacers[200], and adsorbents[185]), under realistic hydrodynamic conditions.

Acknowledgements

This work was supported by the Environment and Natural Resources Trust Fund, as recommended by the Legislative-Citizen Commission on Minnesota Resources. Portions of this work were carried out in the Characterization Facility at UMN, supported by NSF through award DMR-1420013, and at the Minnesota Nano Center, which receives partial support from NSF through the National NanoCoordinated Infrastructure Network (NNCI) (Award Number ECCS-1542202). SRVC is grateful to 3M Co. for a Non-Tenured Faculty Award.

Chapter 4: Feed Temperature Effects on Organic Fouling of Reverse Osmosis Membranes: Competition of Interfacial and Transport Properties

This chapter is in preparation to be submitted to the Journal *Environmental Science: Nano*

BinAhmed, S.; Hozalski, R.; Romero-Vargas Castrillón, S.

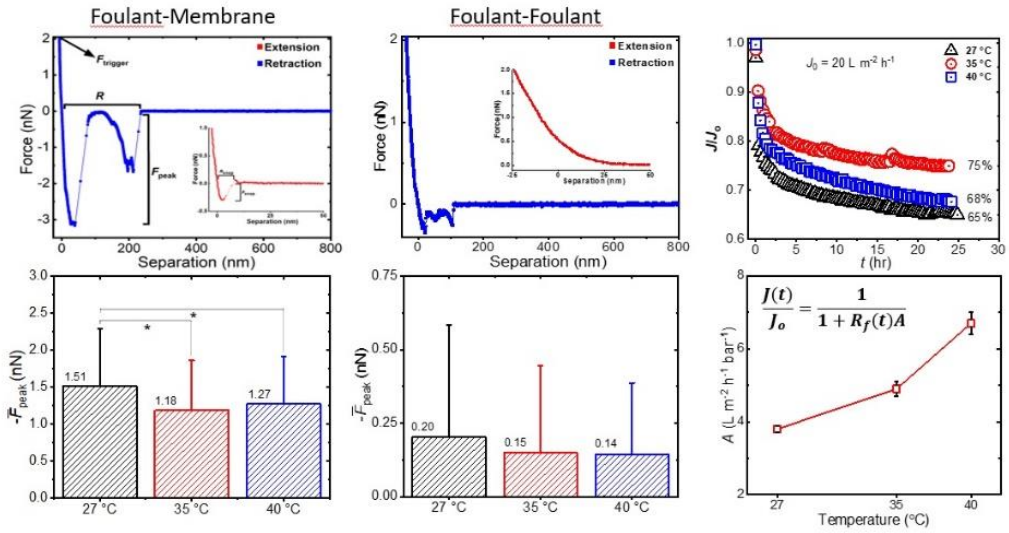

4.1 Summary

Feed temperature is one of the key parameters to affect the performance of reverse osmosis (RO) membranes, but little is known about its effect on organic fouling. This study investigates the effect of temperature on alginate fouling of RO membranes at an intermolecular level using atomic force microscopy (AFM) based colloidal force spectroscopy. A carboxyl modified latex (CML) particle is used as an alginate surrogate to probe foulant-membrane and foulant-foulant intermolecular interactions in synthetic wastewater at T =27, 35, and 40 °C in the presence of 20 mg L^{-1} sodium alginate. Adhesion forces between CML particles and pristine RO membranes are strongest ($p < 0.05$) at 27 °C, while foulant-membrane interactions are similar at 35 °C and 40 °C. Lower adhesion forces at higher temperatures are attributed to weaker hydrophobic force and increasing hydrophilicity of membranes with increasing temperatures. On the other hand, foulant-foulant interactions are weaker than foulant-membrane adhesion forces and show repulsive behavior at each temperature. Steric and electrostatic repulsion resulting from the presence of the fouling layer can explain the resulting similar average foulant-foulant adhesion forces at all temperatures.

The study also examines the effect of feed water temperature (T =27, 35, and 40 °C) on the transport properties and rate of organic fouling by sodium alginate of RO membranes using a bench scale crossflow system. The water permeability coefficient, A, increases with increasing temperature and salt rejection of foulant-free synthetic wastewater is lowest at 27 °C with no significant difference between rejection at 35 °C and 40 °C. Fouling rate measured over 24 hours in terms of normalized permeate flux of synthetic feed wastewater

supplemented with 250 mg L^{-1} alginate shows the largest decline at 27 °C followed by 40 °C then 35 ºC. All temperatures show the same pattern a steep initial flux decline (t < 2 h) followed by slower loss of flux. Fouling rate behavior is explained in terms of the type of hydraulic resistance dominating at each temperature: fouling layer hydraulic resistance at 27 °C in comparison to membrane hydraulic resistance at 35 and 40 °C.

4.2 Introduction

Population growth and climate change are exerting enormous pressure on the world's water resources.[11,16,31] Over 2.4 billion people inhabit highly water stressed areas (defined as those with a water scarcity index > 0.4), many of which are in densely populated urban agglomerations in which water demand exceeds the watershed capacity.[235] In addition to increased population, urbanization, and industrialization[236], climate change is expected to increase water stress through prolonged heatwaves that diminish surface and groundwater supplies.[9] There is thus an urgent need to tap into unconventional water sources (e.g., brackish water, seawater, and wastewater) to expand the water inventory.[3,6,10,11] Water recovered from secondary and tertiary municipal wastewater effluents can supplement water resources[12] through indirect use in agricultural and urban irrigation, cooling towers, and recharge of groundwater aquifers.[4] Desalination and advanced wastewater treatment by reverse osmosis (RO) have been instrumental in sustainably extracting potable water from unconventional water sources. Nonetheless, membrane fouling in its various forms (organic, inorganic, colloidal, biological) remains a key obstacle[5,237,238], resulting in lower permeability and contaminant rejection[5,16,237,239], ultimately increasing energy comsumption.[237]

Research over the past two decades has improved our understanding of the link between fouling propensity and RO membrane interfacial properties. Within the context of organic fouling of polyamide RO membranes, low roughness[48], more hydrophilic[240,241], and more negatively charged[242] membranes exhibit less pronounced flux losses.[48,240–242] Studies on the effect of feed water quality have shown that Ca^{2+} causes more severe organic fouling (compared to Mg^{2+} and Na^{+}) with protein (bovine serum albumin BSA) and alginate[22,42], likely due to calcium-mediated gelation of foulants[22,63,243] and Ca^{2+} bridging of carboxyl groups on the membrane and foulant[42]. Higher ionic strength results in compression of the electrical double layer and shielding of surface charge of both the surface of the membrane and the foulants, resulting in higher fouling rate due to reduced electrostatic repulsion.[22,31,42] The effect of pH is more pronounced around the isoelectric point (IEP) of the foulant, such that foulant-membrane electrostatic repulsion is reduced and fouling rate increases at a pH equal or less than the IEP of the foulant.[31,42,244] The presence of organic matter in water contributes to the formation of an organic fouling layer on the surface of the membrane, which can provide nutrients to bacteria and facilitate bacterial adhesion to the surface.[38,39,78,80] Therefore, minimising organic fouling can help delay biofouling by mitigating initial bacterial adhesion to the surface of RO membranes.[245,246]

The influence of feed water temperature on membrane performance and fouling has attracted far less attention. Only a few studies have been devoted to this subject[41–44], despite the increasing use of membrane-based desalination and wastewater reuse in arid, near-

equatorial latitudes[247] where water temperatures can reach 35.5 ºC.[248] Previous work on the connection between RO membrane transport properties and feed temperature has shown that water permeability[43,70] increases with increasing temperature, due to lower water viscosity[249,250] and higher water diffusivity.[41,43] As a result of increasing temperature, permeate recovery increases[69,70,250,251] and energy consumption decreases due to lower pressure requirements.[69,251,252] Similarly, the salt permeability coefficient, B_s, is directly proportional to the solute diffusivity, D_s, and partition (solubility) coefficient K_s,[41,64,66] both of which increase with temperature, leading to a higher salt flux and lower salt rejection.[69,70,251,253] In one study, Goosen *et al.*[43] observed an increase in permeate flux at a given applied pressure as temperature was increased from 20 ºC to 40 ºC for NaCl concentrations ranging from 0 to 5 % w/v NaCl, suggesting that the membrane undergoes morphological changes such as an increase in the polymer free void volume[43]. Sharma and Chellam[254] observed that the network pore size of nanofiltration (NF) membranes increased with increasing temperature (5 – 41 °C). In another study, Goosen *et al.*[44] found that correcting for viscosity changes of water with increasing temperature did not totally account for the increase in water permeability coefficient with increasing temperature. The researchers suggested an interplay between feed temperature and applied pressure that affected the membrane void volume. Francis and Pashly[250] observed that water recovery and permeate flow increased, while salt rejection decreased, with increasing temperature (20 to 30 °C) when treating seawater (0.5 M NaCl) and brackish water (0.2 M NaCl) with thin-film composite (TFC) RO membranes. Jin *et al.*[41] attributed the lower rejection of humic acid as total organic carbon (TOC) with increasing temperature (T = 15 to 35 °C) to increased swelling of the network voids. The rate of fouling was similar at 25 ºC and 35 ºC

while the highest flux decline occurred at 15 ºC. The higher applied pressure and the larger size of humic acid aggregates at lower temperatures resulted in a higher resistance of the fouling layer at these temperatures.[41] On the other hand, Mo *et al*.[42] reported an increased rate of protein fouling (50 mg L^{-1} bovine serum albumin) of RO membranes at higher temperatures (18 to 35 ºC) and for pH values 4.9, and 7. Baghdadi *et al*.[68] simulated the performance of two TFC RO membranes with increasing temperature (15 – 45 ºC) and observed an increase in salt mass transfer coefficient and a decrease in salt rejection when treating a 35 g L^{-1} NaCl feed water at a constant hydraulic pressure (800 psi).

Current investigations of the effect of feed temperature on membrane performance are limited to bench-scale experiments, which describe thermal effects on membrane transport parameters and flux loss, but offer little mechanistic insight.[41–44,68] To explain the connection between feed temperature and the observed fouling kinetics, it is necessary to understand the thermal response of interfacial properties such as membrane hydrophobicity, roughness, and charge. As a step in this direction, we used colloidal probe atomic force microscopy (AFM) measurements to probe the effects of temperature on membrane-foulant and foulant-foulant interactions. We then explore how the temperature dependence of the interfacial properties manifests itself in RO membrane fouling experiments using alginate, a polysaccharide that is abundant in wastewater[25,255] and in bacterial biofilms[117,256], as a model foulant. We show that weaker hydrophobic interactions with increasing feed temperature (from 27 to 35 ºC) initially decrease membrane fouling, but further increases in feed temperature exacerbate fouling due to an increase in the water permeability coefficient of the membrane. Consequently, variation of the feed temperature

reveals that fouling is determined by a competition between membrane interfacial and transport properties.

This chapter is structured as follows. In section 4.3, we describe the experimental protocols for the colloidal-probe AFM and dynamic fouling experiments. We discuss our results in section 4.4, beginning with the effect of T on interfacial properties (section 4.4.1); the effect of T on foulant-membrane and foulant-foulant interactions, as determined by AFM, is discussed in section 4.4.2; sections 4.4.3 and 4.4.4 present the results of membrane transport and fouling experiments, drawing connections to the interfacial and nanoscale adhesion properties. Concluding remarks are given in section 4.5.

4.3 Materials and Methods

4.3.1 Reverse osmosis (RO) membrane.

All experiments were carried out with ESPA2-LD membranes (Hydranautics, Oceanside, CA), a low pressure aromatic polyamide RO membrane commonly employed in wastewater recycling.[12,257] Membrane coupons (~ 15 × 9 cm^2) were cut out from a 10-cm diameter spiral wound element (membrane area 7.43 m^2), rinsed in ultrapure water (UP) (18.2 MΩ-cm, Barnstead), and stored at 5 ºC in UP water. The hydraulic resistance (R_m = (9.1 ± 0.6) × 10^{13} m^{-1}) and water permeability coefficient (A = 4.5 L m^{-2} h^{-1} bar^{-1}) of the membranes were determined with a UP water feed at 25 °C. For quality assurance purposes, only membranes with A values within the range specified by the manufacturer (3.6 – 5.1 L m^{-2} h^{-1} bar^{-1})[258] were used for dynamic fouling experiments. Further details on the determination of membrane transport properties is provided in Appendix C.

The hydrophilicity and roughness of ESPA2 membranes were characterized at T = 27, 35, and 40 °C. Hydrophilicity was quantified in terms of water contact angle measurements in a temperature-controlled goniometer (DSA30S, Krüss). Root-mean-squared roughness (R_{RMS}) was measured in a temperature-controlled fluid cell using an atomic force microscope (MFP-3D-Bio, Asylum Research) in tapping mode. The zeta potential of the membrane was determined from streaming potential measurements using an electrokinetic analyzer (SurPass, Anton Paar). Streaming potential measurements were performed at 27 °C and 35 °C only (40 °C exceeded the maximum operating temperature of the instrument). Further details on membrane surface characterization are found in Appendix C.

4.3.2 Organic foulant and feed solution chemistry.

We used alginate, a polysaccharide[259], as a model foulant representative of extracellular polymeric substances (EPS)[260–263] in secondary wastewater effluent[262–264]. A 6 g L^{-1} sodium alginate (SA) (A2033, Millipore Sigma, St Louis, MO) stock solution was prepared in UP water before each dynamic fouling experiment by stirring the solution for 24 hours. Alginate was dosed at a concentration of 250 mg L^{-1} to a feed solution containing 0.45 mM KH_2PO_4, 0.935 mM NH_4Cl, 0.5 mM $CaCl_2$, 0.5 mM $NaHCO_3$, 9.20 mM NaCl, and 0.61 mM $MgSO_4$ at pH 7.4. The inorganic composition of the synthetic wastewater used in all fouling experiments is representative of the inorganic fraction of secondary wastewater effluent from certain wastewater treatment plants in California.[117,265] The ionic strength of foulant-free synthetic wastewater was 14.7 mM (MinTEQ 3.1). The alginate concentration used (250 mg L^{-1}) is much higher than concentrations in real systems (in

which TOC concentrations are in the 5-20 mg L^{-1} range.[32,266–268] An elevated concentration was used to accelerate fouling and ensure fouling can be observed within 24 hours.

4.3.3 Dynamic fouling experiments.

A bench-scale crossflow system (see Appendix C) was used for our fouling experiments, each comprising the following stages: 1) Membrane compaction at 500-580 psi with UP water at 25 ºC until a steady-state permeate flux was achieved. 2) Stabilization of the permeate flux at J = 20 ± 1 L m^{-2} h^{-1} (LMH) for 1 hour at 25 °C to validate the water permeability coefficient of the membrane (the expected water permeability coefficient for ESPA2-LD membranes is 3.6 – 5.1 LMH bar^{-1} [258]). 3) Adjustment of the temperature of the UP water feed to 27, 35, or 40 ºC by means of a heater/chiller (6500 series, Polyscience) followed by overnight stabilization of the permeate flux at J = 20 ± 1 LMH (this stage was used to calculate the A coefficient at each temperature). 4) Dosing of alginate-free synthetic wastewater into the feed tank, followed by system stabilisation at the desired temperature (27, 35, or 40 ºC) at J = 20 ± 1 LMH; this stage typically required stabilisation for 4-6 days, and included sampling of the feed and permeate conductivity to determine salt rejection before fouling. 5) Dosing of 250 mg L^{-1} alginate into the synthetic wastewater feed and initiation of dynamic fouling; the flux loss during fouling was measured over 24 hours accompanied by sampling of the feed and permeate conductivity and TOC content (2 and 24 hours after initiation of fouling) to calculate salt and TOC rejection, respectively. The flow rate was recorded every 0.2 seconds at all phases (except compaction) with a digital flow meter (SLI-2000, Sensirion, Stäfa, Switzerland) and logged to a computer. Further

details on the experimental apparatus and fouling experiments can be found in Appendix C.

4.3.4 Colloidal Probe AFM Force Spectroscopy.

Colloidal probes Carboxyl-modified latex (CML) colloidal particles with a nominal diameter of 4 μm were used in all AFM measurements. These polystyrene microspheres have a surface rich in carboxylic acid functional groups[263,269], which are commonly found in alginate and other foulants.[61,263] According to the product specifications (ThermoFisher Scientific, C37253), the CML particles are hydrophobic at low pH and somewhat hydrophilic at high pH. However, other studies have characterized similar CML particles as hydrophobic.[270] CML particles were received as a 4% w/v suspension in deionized water and were stored at 5 ºC until use.

Preparation of colloidal probes The protocol for preparing the colloidal probes was adapted from that reported by others.[31,51,269] A 20-μL aliquot of CML particle suspension (2500× dilution) was deposited on a UV/O_3-cleaned [271] glass slide and dried overnight in a desiccator. An inverted optical microscope (Zeiss Axio Observer A.1) integrated into the AFM was used to guide a tipless AFM cantilever (MLCT-O10 cantilever "A", nominal *k* = 0.07 N/m, Bruker) first towards a small amount of UV-curable glue (Norland 86, Norland optical, Cranbury, NJ) deposited on the glass slide and then towards the CML to be adhered to the cantilever. The prepared AFM colloidal probes were then cured in a solar simulator (Xenon lamp, wavelength > 290 nm, 350 W/m^2) for 30 minutes.

Experimental conditions Measurement of interfacial interactions between the CML probes and the surface of pristine and alginate-fouled ESPA2 membranes was performed using an atomic force microscope (MFP-3D-Bio, Asylum Research) equipped with a temperature-controlled fluid cell. Force measurements were conducted at T = 27 °C, 35 °C, and 40 °C in two different systems: pristine membranes in 20 mg L^{-1} alginate in synthetic wastewater (a concentration representative of the TOC levels of 5-20 mg L^{-1} [262,266] in wastewater effluent); and alginate-fouled membranes in synthetic wastewater supplemented with 20 mg L^{-1} alginate. The former investigates the temperature dependence of foulant-membrane interactions, which determine the initial adhesion of foulant at the early stages of fouling, while the latter measurements investigate foulant-foulant interactions in the subsequent stages, once a foulant layer has formed on the membrane surface.[31,62,269] Synthetic wastewater supplemented with 20 mg L^{-1} alginate was freshly prepared prior to each experiment as described in section 4.3.2. The alginate-fouled membrane substrate was prepared as described in Appendix C. To distinguish between real CML particle adhesion and artifacts resulting from particles contaminated with glue, control measurements were performed using a particle-free cantilever on which we deposited a small amount of cured glue. These measurements (performed in phosphate buffered saline at pH 7.4 on pristine membranes) resulted in distinctly sharp adhesion peaks compared to those of clean CML particles. Probes suspected of glue contamination were discarded. Only data collected with CML particles unaffected by glue artifacts are presented and discussed.

For individual coupons, force measurements were collected at 27 °C, then 35 °C, and finally at 40 °C by ramping up the temperature at a rate of 1 °C/min. After allowing 30

minutes for the cantilever to reach thermal equilibrium, at each set-point temperature the inverse optical lever sensitivity and spring constant were determined (the latter according to the thermal noise method[129]). Measurements at the three temperatures were repeated in triplicate (i.e., with three different membrane coupons) with three independently functionalized AFM cantilevers. A total of ≥ 105 force curves were collected at each temperature. To account for membrane surface heterogeneity[79], adhesion forces were measured at each temperature over at least 11 randomly selected spots (collecting 3 force curves per spot) located at least 6 μm apart from one another. The AFM probe was checked at the end of every experiment to verify that the CML particle was not dislocated and that it had remained at its original position during force measurements.

Force curves were recorded at 200 nm/s approach-retraction speed, a cycle speed that results in negligible dissipative friction on the CML particle.[272] The CML probe engaged the membrane substrate with a trigger force ($F_{trigger}$; **Figure C. 3**) of 2 nN, while remaining in contact with the surface of the pristine or fouled membrane for a dwell time of 5 seconds. A constant force was maintained between the CML particle and membrane surface during the dwell time by setting the feedback channel to deflection. AFM experiments were performed in open loop to minimize noise in the collected forces. The choice of trigger force was based on calculations of the permeation drag force exerted on a 4 μm diameter particle experiencing a flux of 20 LMH, typical of RO operation (see Appendix C for a detailed discussion). For data analysis, the minimum measurable force – 30 pN – was determined by measuring the noise in the free end of several force curves at each temperature. Parameters collected from force curves are identified in **Figure C. 3**. From

the extension force curve: snap-in force (F_{snap}) is defined as the adhesion force observed as the colloidal probe approaches the membrane substrate;[273–275] snap-in separation (R_{snap}) is identified as the distance at which the snap-in event occurs.[118,276] From the retraction force curve: peak adhesion force (F_{peak}) is defined as the maximum adhesion force observed as the colloidal probe is pulled away from the membrane; rupture separation (R) is the distance at which interactions between the probe and the membrane surface vanish.[72]

4.3.5 Statistical analysis.

Unpaired two-sided homoscedastic (equal variance) *t*-tests were used to determine statistical significance of the results using Excel and Origin.

4.4 Results and Discussion

4.4.1 Characterization of RO membrane.

Characterizing the interfacial properties (contact angle, roughness, and surface charge) of the RO membrane as a function of temperature can help better understand the effect of temperature on the membrane fouling behavior. It is generally accepted that hydrophilic membranes[1,46,277] of low surface roughness[16,30] are more fouling resistant.

The contact angle of sessile water droplets (θ_w) reflects membrane hydrophilicity[1,278,279] and depends on membrane properties (surface roughness, surface charge, and surface functional groups)[1,258,278,280] as well as on external conditions such as water temperature[278,281] and salt concentration[278,282]. The effect of temperature on θ_w and root-mean-squared roughness (R_{RMS}) of pristine RO membranes is shown in **Figure 4. 1.** The measured θ_w at 27 ºC (53.5 ± 2.5º) is similar to that reported by other studies (43º-55º)[12,283]

on ESPA2 membranes at room temperature. The contact angle at 27 ºC was significantly higher from that at 35 ºC (38.5 ± 2.8º; $p < 0.01$) and at 40 ºC (36.7 ± 3.5°; $p < 0.01$) but θ_w at 35 ºC and 40 ºC were similar ($p = 0.078$). The decrease in contact angle with increasing temperature is a manifestation of a general surface phenomenon: as first postulated by Zisman[284] and Petke and Ray[285], θ_w decreases with rising T for common liquids whose surface tension decreases with increasing T. It is expected that the membrane would swell more at higher temperatures, as has been observed with polyamide membranes[41,286], due to the increasing wettability of the membrane by water. Consistent with this expectation, we observed (**Figure 4. 1.**) an increase in R_{RMS} of the pristine RO membrane with increasing temperature (representative AFM scans at each T are given in **Figure C. 1.**). R_{RMS} increased from 91.8 ± 12.3 nm at 27 ºC to 113.7 ± 15.7 nm at 35 ºC ($p < 0.01$) and 102.8 ± 14.5 nm at 40 ºC ($p < 0.05$), while the R_{RMS} values at 35 °C and 40 °C were similar ($p = 0.0562$).

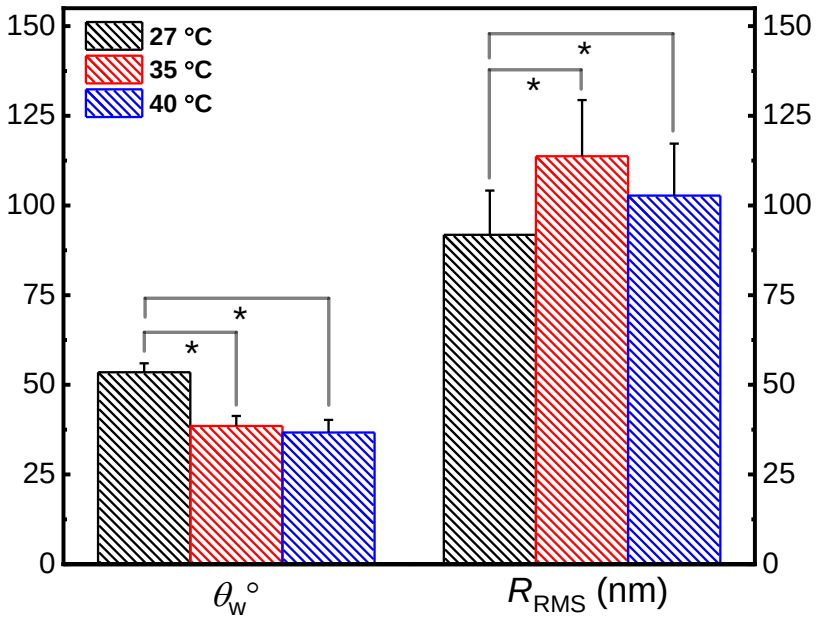

Figure 4. 1. Sessile water drop contact angle (θ_w) and root-mean-squared roughness (R_{RMS}) measurements of pristine ESPA2 membranes at T = 27, 35, and 40 °C (* denotes a significant difference between the indicated samples, $p < 0.05$).

The zeta potential (ζ) of ESPA2 membranes at 27 ºC (**Figure C. 2.**) varied from -7 mV to -35 mV as pH was increased from 4 to 10 with ζ ≈ -30 mV at pH = 7.4 which is similar to other reports of measurements made at room temperature[12] (-45 mV at pH = 9[12,283] to -10 mV at pH = 4[283]). The negative charge of polyamide is due to the deprotonation of carboxylic acid groups on the membrane surface[282], and presumably to the adsorption of hydroxide ions on uncharged hydrophobic regions on polyamide. Hydroxide ion adsorption is posited as the cause of the negative charge of many hydrophobic surfaces.[49,287] At 35 °C we observe similar charging behavior at pH < 7, while a less negative ζ is observed at basic pH. We ascribe this behavior to a lower extent of adsorption of hydroxide ions resulting from the decreasing hydrophobicity of the interface at 35 °C (cf. **Figure 4. 1.**).

4.4.2 Effect of temperature on adhesion forces.

In this section, we investigate the T dependence of membrane surface forces using AFM-based force spectroscopy measurements with a carboxylated colloidal probe (a mimic of alginate). We considered pristine membranes as well as alginate-fouled membranes (prepared as explained in Appendix C) to investigate the T dependence of foulant-membrane and foulant-foulant interactions. Previous work has used AFM to relate foulant-membrane interactions to the rate of fouling, finding a strong correlation between fouling propensity and the strength of adhesion forces determined by AFM.[263,269] On the other hand, the effect of temperature, investigated below, has hitherto been overlooked. We analyzed

both the approach and retraction segments of the force curves. The approach segment provides information about the mechanism of adhesion of foulant molecules as they first encounter the membrane interface, i.e., whether foulants experience repulsive or attractive forces during initial adhesion (and the strength of such interactions). The retraction segment quantifies the force necessary to detach adhered foulants.

Before discussing the force spectroscopy data quantitatively (**Figure 4. 2. - Figure 4. 3, Figure C. 6. - Figure C. 9.**), a few qualitative features of the force curves are noteworthy. **Figure C. 3.** and **Figure C. 4.** show representative force-distance curves, including the approach segment as the inset, collected over pristine and alginate-fouled membranes, respectively. The CML microsphere experiences a small repulsive force (43-50 pN) as it approaches the surface of pristine membranes; this repulsion is likely steric as it is observed at separations (8 – 9 nm) greater than the Debye length (2.5 nm at I = 14.7 mM). At shorter separations, the polystyrene chains protruding from the microsphere eventually encounter the surface, and the microsphere experiences a sudden attractive force known as a 'snap-in' or 'jump-to-contact' spring instability[52,288]: at the snap-in point, the gradient of the particle-membrane force exceeds the cantilever spring constant, the cantilever becomes unstable (i.e., the particle-surface force and the cantilever elastic force are no longer in balance), and jump-to-contact occurs. This jump-to-contact force has been attributed to the van der Waals attractive force between the tip and the surface.[273–275] Moreover, as discussed below, the T dependence of the magnitude of the snap-in force is evidence that particle adhesion is also driven by hydrophobic interactions between the membrane and the colloidal particle. The snap-in force is not observed in the approach force curves

recorded over alginate-fouled membranes (inset in **Figure C. 4.(a)**); instead, the force is repulsive throughout the contact region, but the gradual increase in the loading force is consistent with compression of the soft alginate layer by the colloidal microsphere.[276] The retraction force curves over pristine membranes display sharp (often multiple) adhesion peaks (**Figure C. 3.**), presumed to be due to the stretching of polystyrene chains upon probe pull-off. In some cases, we observe tethering events **Figure C. 5.**), which are likely due to detachment of alginate molecules bridging (with the aid of Ca^{2+}) the CML probe and the membrane surface[60], or desorption[289] of alginate molecules from the membrane. Over alginate-fouled membranes, we observe adhesion peaks, likely due to alginate desorption (**Figure C. 4.(a)**). In addition, a fraction of the force curves (quantified below) are repulsive during retraction (**Figure C. 4.(b)**) indicating that the alginate layer prevented the adhesion events that are otherwise observed in pristine membranes.

Next, we discuss quantitatively the force spectroscopy data in terms of the distribution of peak adhesion, snap-in forces, and rupture separations (defined in Section 4.3.4 and in **Figure C. 3.**). The data are plotted as histograms in **Figure 4. 2. - Figure 4. 3, Figure C. 6. - Figure C. 9.** The distribution of snap-in forces (F_{snap}) and snap-in separations (R_{snap}) on pristine membranes is shown in **Figure C. 6.** and **Figure C. 7.** As shown in **Figure C. 6. (d)**, the attraction is strongest at 27 °C when the membrane is least hydrophilic and smoothest (see **Figure 4. 1.**), with an average snap-in force ($\bar{F}_{snap}$) of 115 pN compared to 81 pN at 35 °C (p = 0.039) and 92 pN at 40 °C (p = 0.138). The force curves that do not display a snap-in force (i.e., purely repulsive approach curves tallied as the "NO" column in **Figure C. 6. (a-c)**), representing between 31.4% and 45.7% of the forces were assigned

F_{snap} = 0 when calculating the average in **Figure C. 6. (d)**. A similar trend – decreasing $\bar{F}_{snap}$ with rising *T* is observed when the average excluded the non-adhesive approaches, Figure **Figure C. 6. (e)**. The probability with which snap-in events occurred (ranging between 54.3% and 68.6%), and the distance at which snap-in is established (R_{snap}, **Figure C. 7.**), ~8-9 nm on average, showed no discernible *T* dependence.

Figure 4. 2. (a-c) shows the peak adhesion force (F_{peak}) distribution (defined in **Figure C. 3.**) of CML probes collected over pristine membranes at *T* = 27, 35, and 40 ºC. The distribution of F_{peak} at 27 ºC shows more frequent strong adhesion events (-3 nN < F_{peak} < -2 nN) compared to higher temperatures. Moreover, **Figure 4. 2. (d)** shows that the average adhesion force at 27 ºC ($\bar{F}_{peak}$ = -1.51 ± 0.78 nN) is stronger than that at 35 °C ($\bar{F}_{peak}$ = -1.18 ± 0.68 nN; *p* = 0.0015) and 40 °C ($\bar{F}_{peak}$ = -1.27 ± 0.65 nN; *p* = 0.0174). Adhesion forces at 35 °C and 40 °C were similar (*p* = 0.339). Moreover, the distribution of rupture separations (*R*) over pristine membranes (**Figure C. 8.**), ranging between 120 and 150 nm, was not found to be *T* dependent.

The decreasing adhesion force with increasing temperature observed during approach (F_{snap}; **Figure C. 6.**) and retraction (F_{peak}; **Figure 4. 2.**) followed the same trend with *T* as hydrophobic interactions, suggesting that the *T* dependence of organic foulant adhesion shows close resemblance to hydrophobic hydration phenomena. Weakening of hydrophobic adhesion forces with rising *T* agree with previous force spectroscopic experiments.[290,291] The decreasing magnitude of adhesion forces is also consistent with theoretical investigations showing that extended surfaces become less hydrophobic with

rising *T*.[292] Huang and Chandler[292] showed that the excess chemical potential per unit surface area decreases monotonically with increasing temperature for extended hydrophobic surfaces (spheres of radii > 1 nm). As a result, the change in entropy of solvation becomes positive and the free energy of solvation decreases with temperature.

While hydrophobic interactions appear to be the main driving force of foulant-membrane adhesion, we cannot rule out the possibility that adhesion is aided by Ca^{2+}-mediated [238,269] bridging interactions between the deprotonated carboxylic groups on the CML particle and the surface of the membrane. Both the membrane (**Figure C. 2.**) and alginate are negatively charged at pH > 6 because most of the carboxylic groups are deprotonated[60] (pK_a = 3.5 - 4.7 [31,48,293]). The presence of deprotonated carboxylic acid groups is suggested by the negative charge of both the membrane (**Figure C. 2.**) and alginate.[48,60]

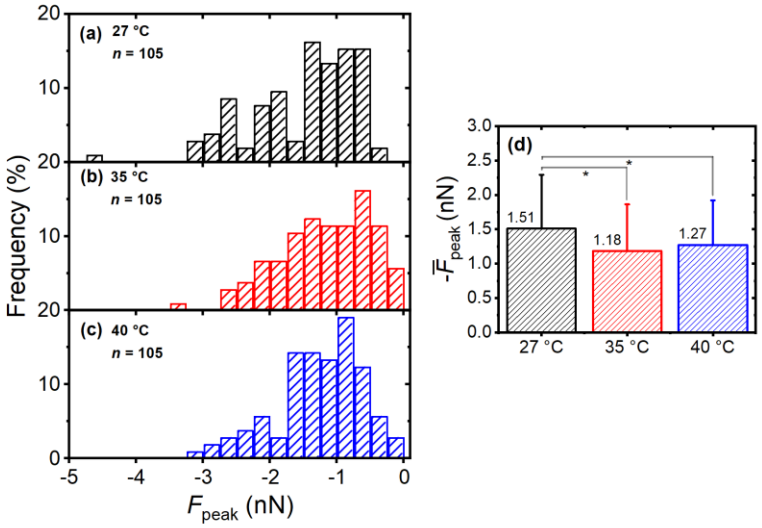

Figure 4. 2. (a-c) Distribution of peak adhesion forces (F_{peak}) of CML colloidal probes on pristine membranes for each indicated temperature (given in the inset along with the number of force measurements, n). (d) Average peak adhesion force ($\bar{F}_{peak}$) at each temperature calculated from (a-c) (* denotes statistical significance with $p < 0.05$). Error bars denote one standard deviation. Data were collected in synthetic wastewater supplemented with 20 mg L^{-1} sodium alginate ($t_{contact}$ = 5 s; $F_{trigger}$ = 2 nN; pH 7.4; I = 14.7 mM).

Substantially different surface forces dominate the interactions between the colloidal particle and the alginate-fouled membrane. These results are presented in **Figure 4. 3. (a-c)** for T = 27, 35, and 40 ºC, respectively. As mentioned previously, snap-in events are absent in measurements with fouled membranes, observing instead repulsive forces during approach at any temperature (see **Figure C. 4.**). Repulsive forces are also observed in 25.9-33.3% of retraction force curves (denoted by the "NO" column in **Figure 4. 3. (a-c)**) These repulsive forces can be attributed to stronger electrostatic repulsion between the CML particle and the more negative membrane surface in the presence of alginate fouling

layer.[136] Wang *et al.*[62] also attributed weaker alginate-alginate adhesion forces to electrostatic repulsive forces resulting from the more negative charge of alginate compared to other foulants (bovine serum albumin and effluent organic matter).

In contrast to pristine membrane, the average peak adhesion force ($\bar{F}_{\mathrm{peak}}$) over fouled membranes is significantly weaker in magnitude and less sensitive to temperature ($p > 0.05$ for all pairwise comparisons) irrespective of whether repulsive forces curves are included in the average (**Figure 4. 3. (d)**) or not (**Figure 4. 3. (e)**)

The distribution of rupture separations (R) of CML particles over fouled membranes at T = 27, 35, and 40 ºC is shown in **Figure C. 9.** Although $\bar{R}$ is similar for all the temperatures investigated ($p > 0.05$ for all pairwise comparisons), $\bar{R}$ is much longer on the fouled membranes than on pristine membranes (compare **Figure C. 9.** with **Figure C. 8.**). Longer rupture separations are likely due to desorption of alginate molecules from the membrane surface during probe retraction.

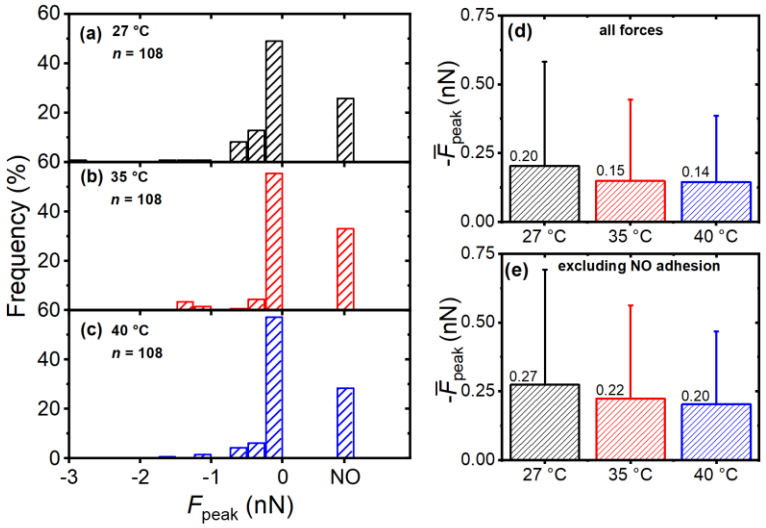

Figure 4. 3. (a-c) Distribution of peak adhesion forces (Fpeak) of three CML colloidal probes on alginate-fouled membranes for each indicated temperature (given in the inset along with the number of force measurements, n). Force curves in which |Fpeak | < 30 pN are tallied as the "NO" column (30 pN is the magnitude of the noise observed in the free end of force curves). (d) Average peak adhesion force ($\bar{F}_{\mathrm{peak}}$) at each temperature calculated from (a-c) including the non-adhesive events as $\bar{F}_{\mathrm{peak}} = 0$. (e) Average peak adhesion force ($\bar{F}_{\mathrm{peak}}$) at each temperature calculated from (a-c) excluding the non-adhesive events. Error bars denote one standard deviation. Data were collected in synthetic wastewater supplemented with 20 mg L^{-1} sodium alginate (t_{contact} = 5 s; F_{trigger} = 2 nN; pH 7.4; I = 14.7 mM).

4.4.3 Effect of temperature on membrane transport parameters and fouling.

Having established the *T*-dependence of membrane adhesive properties, we next examine the impact of the latter nanoscale phenomena on transport and selectivity during membrane filtration. The effect of temperature on the permeability coefficient of water and conductivity rejection of ESPA2 thin-film composite membranes is shown in **Figure 4. 4.**

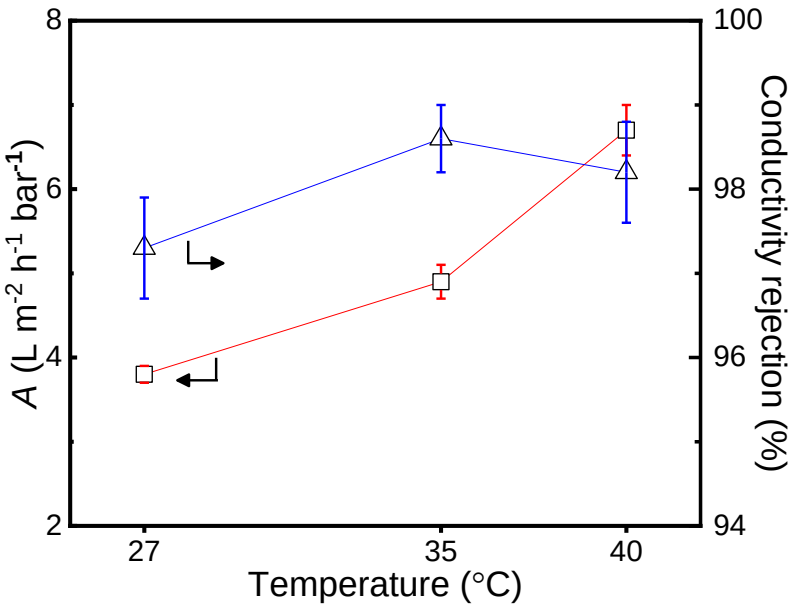

Figure 4. 4. Effect of temperature on the water permeability coefficient (A) and conductivity rejection (right axis) at T = 27, 35, and 40 ºC. The error bars in the determination of A denote one standard deviation computed from measurements of flow rate collected every 0.2 s and pressure. Alginate-free synthetic wastewater feed was used to determine conductivity rejection (n = number of measurements; n = 6 at 27 °C, n = 6 at 35 °C, and n = 8 at 40 °C). Error bars denote one standard deviation. All data determined at a permeate flux of 20 ± 1 LMH.

In agreement with previous experiments (5 ºC < T < 60 ºC)[43,69,294], A increases with feed temperatures (**Figure 4. 4.**) from 3.8 ± 0.1 LMH bar^{-1} at 27 ºC to 4.9 ± 0.2 and 6.7 ± 0.3 LMH bar^{-1} at 35 ºC and 40 ºC, respectively. The change in permeability coefficient with temperature is due to the dependence of A on water viscosity and diffusivity[41,69]: $A \propto \frac{D_{\mathrm{w,m}}}{T}$ ($D_{\mathrm{w,m}}$ is water diffusivity in the membrane) and $D_{\mathrm{w,m}} \propto \frac{T}{\mu}$ (μ is the dynamic water viscosity).[41] As a result, A will be inversely proportional to μ which, in turn, varies inversely with temperature.[70,294,295] Another possible factor contributing to the increase in A is the thermal expansion of the polyamide network[41]: the increase in surface roughness with T (**Figure 4. 1.**) is presumably due to thermal expansion of the polyamide active

layer.[41] In addition, the increasing roughness with T may provide a larger effective permeable area[296], resulting in a larger A[297].

Conductivity rejection was found to be weakly dependent on T, ranging from 97.3 ± 0.6% at 27 °C to 98.6 ± 0.4% and 98.2 ± 0.6% at 35 ºC and 40 ºC, respectively. While these observations are at odds with the expected temperature dependence of the solute diffusivity, D_s, and solubility, K_s, in the membrane (both D_s and K_s increase with increasing temperature)[30,41,69], the results in **Figure 4. 4.** appear to be in agreement with other studies showing negligible temperature dependence of the reflection coefficient over a similar temperature range.[43]

4.4.4 Effect of temperature on organic fouling.

The effect of temperature on alginate fouling is investigated in **Figure 4. 5. (a)**, showing the normalized permeate flux, J/J_o as a function of time. The time dependence of the permeate flux exhibits common features at all temperatures, indicative of a transition of fouling dominated by foulant-membrane interactions to a regime determined by foulant-foulant interactions.[298] A steep flux loss (26% at 27 ºC, 19% at 35 ºC, and 22% at 40 ºC) within the first two hours is followed by slow flux decline at longer times (**Figure 4. 5. (a)**). This behavior is consistent with our colloidal AFM data: at short time scales, fouling is dominated by strong foulant-clean membrane interactions (**Figure 4. 2.**), leading to the rapid formation of a foulant layer and significant flux loss. At longer times scales ($t \gtrsim 5$ h), weakly adhesive or repulsive foulant-foulant interactions (**Figure 4. 3.**) cause J/J_o to decrease at a much slower rate. On the other hand, the extent of flux loss is different at

each temperature. Fouling is most severe at 27 °C, with a flux loss of 35% after 24 h compared to 25% at 35 °C and 32% at 40 °C. The more significant fouling at 27 °C is consistent with the stronger hydrophobic interactions at this temperature (cf. **Figure 4. 2.**). However, at 35 and 40 °C different fouling propensity does not reflect the similar adhesion forces observed (**Figure 4. 2.**). Thus, interfacial behavior alone does not explain the observed fouling behavior.

To reconcile the fouling experiments in **Figure 4. 5. (a)** with the interfacial behavior presented in **Figure 4. 2.**, we quantified the resistance contributed by the foulant layer to water transport using a resistance-in-series model.[299,300] Within the series-resistance approach, the overall transport resistance of the fouled membrane is given by the sum of the individual hydraulic resistances of the polyamide (A^{-1}) and a (time-dependent) hydraulic resistance due to the foulant layer, $A_f(t)^{-1}$. The resulting expression for the time-dependent flux through the fouled membrane is,

$$J(t) = \frac{1}{A^{-1}+A_f(t)^{-1}}(\Delta p - \Delta\pi) \qquad (4.1)$$

where $\Delta\pi$ is the osmotic pressure difference between the feed and the permeate. Dividing Equation (4.1) by the steady-state water flux through the clean membrane ($J_o = A(\Delta p - \Delta\pi)$) yields,

$$\frac{J(t)}{J_o} = \frac{1}{1+\frac{A}{A_f(t)}} = \frac{1}{1+R_f(t)A} \qquad (4.2)$$

where the inverse of the permeability of the foulant layer is expressed as a hydraulic resistance, $R_f(t) = A_f(t)^{-1}$. Equation (4.1) shows that two mechanisms can contribute to flux loss: fouling, which increases $R_f(t)$ as the foulant layer develops; and increasing water permeability (e.g., due to T), which will also lower J/J_o. Based on the characterization results, we speculate that the smaller flux loss at 35 °C compared to 27 °C is primarily due to the effect of the interfacial properties on the foulant layer: a lower R_f value at 35 °C results from a thinner foulant layer due to a more hydrophilic membrane (**Figure 4. 1.**) and weaker hydrophobic interactions (**Figure 4. 2.**) at 35 ºC versus 27 ºC. The smaller R_f mitigates the effect of a larger value of A at 35 °C compared to 27 °C (**Figure 4. 4.**), with the net effect being a smaller flux loss at 35 °C. Conversely, increasing T from 35 to 40 °C brings about a negligible change in interfacial properties and R_f (similar hydrophilicity and adhesion forces, cf. **Figure 4. 1.** and **Figure 4. 2.**), but a significant increase in A (**Figure 4. 4.**) that results in more severe flux loss at 40 °C compared to 35 °C.

These arguments are supported by the experimental data. Solving for R_f using Equation (4.2) with data from **Figure 4. 4.** and **Figure 4. 5.** ($A_{35\,°C}$ = 4.9 LMH bar^{-1}, $A_{40\,°C}$ = 6.7 LMH bar^{-1}, $(J(t = 24\text{ h})/J_o)_{35\,°C}$ = 0.75 and $(J(t = 24\text{ h})/J_o)_{40\,°C}$ = 0.68) yields $R_{f,\,35\,°C}$ = 0.07 bar LMH^{-1} and $R_{f,\,40\,°C}$ = 0.07 bar LMH^{-1}, i.e., similar foulant layer resistances consistent with the AFM results (**Figure 4. 2.**); thus, greater flux loss at 40 °C compared to 35 °C stems from $A_{40\,°C} > A_{35\,°C}$ (**Figure 4. 4.**). On the other hand, $R_{f,\,27\,°C}$ = 0.14 bar LMH^{-1}, a significantly higher resistance (due to stronger adhesions at 27 °C) that causes a more pronounced flux loss compared to higher T.

Finally, the results of salt and TOC rejection at each temperature are summarized in **Figure 4. 5. (b)**. These data are derived from measurements at t = 2 h and 24 h after initiation of the fouling experiment and are reported as a single average as they were similar (within 1%) to one another at each temperature. Salt rejection remained approximately constant with increasing temperature, exhibiting values similar to those of the clean membrane (see **Figure 4. 4**. Similarly, TOC rejection shown in **Figure 4. 5. (b)** is independent of temperature. Although increased passage of dissolved alginate could be expected with rising temperature on account of membrane swelling[41], the high TOC rejection suggests that alginate (likely found as Ca^{+2}-complexed aggregates) are large enough (> 1 nm[301], compared to sub-nanometer voids in polyamide[16,297]) as to deposit on the surface of the membrane as a fouling layer. The TOC passage observed (1.7-2.4%) is likely due to low molecular weight impurities in alginate (e.g., polyphenols and proteins[302]). Similar TOC passage has been observed by previous studies with humic acid.[41]

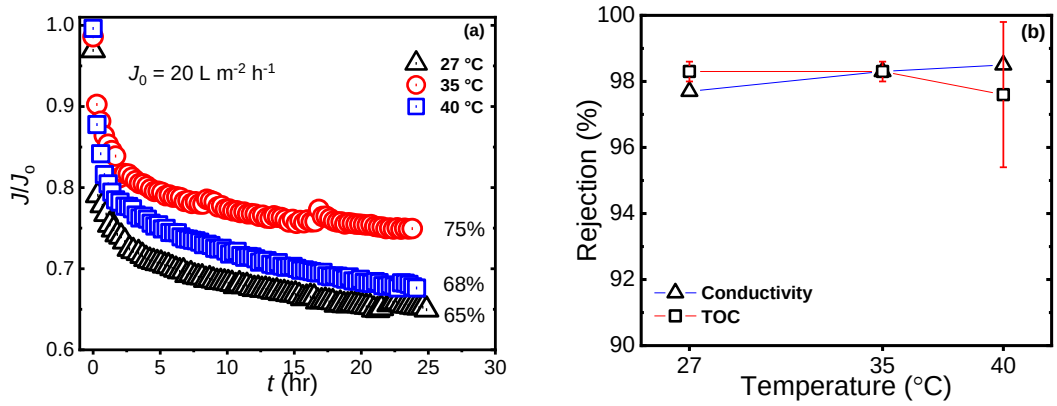

Figure 4. 5. Effect of temperature on the performance of ESPA2 membranes during alginate fouling: (a) flux decline of ESPA2 membranes over 24 hours during accelerated fouling with 250 mg L^{-1} sodium alginate for each indicated feed temperature given in the inset. A 5000 point Loess method (Origin 2020) was used to filter the normalized flux using Origin. (b) Average conductivity and TOC rejection. Error bars denote one standard deviation. Experimental conditions: initial permeate flux J_o = 20 LMH; feed solution 14.7 mM synthetic wastewater at pH = 7.4 supplemented with 250 mg L^{-1} sodium alginate; crossflow velocity = 19.8 cm/s.

4.5 Conclusions

In this study we investigate the effect of temperature (T = 27, 35, and 40 °C) on organic fouling of RO membranes at two different scales: intermolecular level using atomic force microscopy (AFM) and membrane scale using a cross flow system for accelerated dynamic fouling. We observe that the initial rate of fouling is *T* dependent and is determined by the foulant-membrane interactions. On the other hand, long term fouling is not *T* dependent such that foulant-foulant adhesion forces and the slope of flux decline are similar at all temperatures. Our results show that measurements of foulant-membrane and foulant-foulant adhesion forces can be used to predict fouling behavior (rate flux decline) as a function of temperature.

Our work emphasizes the importance of temperature as an operating parameter that needs to be taken into consideration by manufactures to make RO membranes robust for a wider temperature range to accommodate for different climates and seasonal changes. Operators should also take into consideration the temperature of the feed as a major factor resulting in a compromise between performance and fouling of the membranes. While lower temperatures should result in better salt and TOC rejection, they also increases the rate of organic fouling and energy requirements as higher pressure is needed to maintain a constant permeate flux.

Chapter 5: Conclusions and Recommendations

Single-cell force spectroscopy (SCFS) was used as a major experimental tool in this research to investigate initial stages of bacterial attachment. The presented work have shown that initial bacterial adhesion is dependent on different interfacial properties of ultrafiltration (UF) membranes as well as operational parameters. Hydrophilicity of the substrate proved to be a critical property that weakens bioadhesion. The presence of natural organic matter (Mississippi River NOM) in solution and as fouling layer also weakens bioadhesion due to steric and electrostatic repulsion. We have also shown that bioadhesion is time-dependent such that increased contact time (t = 0, 2, and 5 s) between the cell and the surface of UF membrane resulted in stronger adhesion. Although the formation of biofilms is inevitable, the onset of bacterial adhesion to the surface of the membranes can be delayed and/or weakened considering these different factors. Future work can evaluate the effectiveness of these factors to mitigate for long-term bioadhesion.

Part of this research have shown that edge-tethering of graphene oxide (GO) nanosheets to polyacrylic acid (PAA) brushes covalently bonded to UF membranes resulted in more repulsive bacterium-membrane interactions. The weaker bioadhesion resulted from increased hydrophilicity and steric repulsion due to the GO-PAA brush layer not the GO itself. Therefore, incorporating GO to membrane surfaces need to be in combination with other modifications that render the membranes more hydrophilic and increase steric repulsion. Like other novel membrane modification methods, a major obstacle in incorporating PAA-GO would be the feasibility of upscaling the production of modified membranes. At the same time, factors (such as size of GO sheets and methods of

binding GO to the surface, internal structure, or spacers) that can play a role in the robustness of GO modification and its effect on bacterial adhesion can be further investigated.

An important part of this thesis is the worm-like chain (WLC) model analysis applied to SCFS data exhibiting extension of protein domains. Although the exact adhesins involved in bacterial adhesion cannot identified since we used a wild bacterial species, the WLC analysis of the sawtooth pattern observed during force measurements (Chapters 2 and 3) indicate that importance of proteins, and consequently, hydrophobic interactions in mediating initial bacterial adhesion.

This work have also shown that temperature is a critical operational parameter as it can affect both the transport properties of the membrane as well as foulant-membrane and foulant-foulant interactions. Initial rate of fouling was temperature dependent and correlated with measured foulant-membrane interactions. Colloidal force spectroscopy can be used as a tool to anticipate fouling propensity of membranes.

Future work can study a broader range of temperatures (T < 27 ºC and T > 40 ºC) to investigate how transport and interfacial properties of membranes are affected. Further research might identify if one of these properties dominates at higher or lower temperatures. Such work can help treatment plant operators adjust operational parameters to mitigate for fouling. Additionally, the effect of operational temperature on the internal structure of RO membranes can also be investigated to further understand the changes in transport properties.

References

(1) Miller, D. J.; Dreyer, D. R.; Bielawski, C. W.; Paul, D. R.; Freeman, B. D. Surface Modification of Water Purification Membranes. *Angew. Chemie Int. Ed.* **2017**, *56* (17), 4662–4711. https://doi.org/10.1002/anie.201601509.

(2) Water Facts - Worldwide Water Supply https://www.usbr.gov/mp/arwec/water-facts-ww-water-sup.html#:~:text=3%25 of the earth's water,water is available fresh water.

(3) Elimelech, M.; Phillip, W. a. The Future of Seawater Desalination: Energy, Technology, and the Environment. *Science* **2011**, *333* (6043), 712–717. https://doi.org/10.1126/science.1200488.

(4) Petala, M.; Tsiridis, V.; Samaras, P.; Zouboulis, A.; Sakellaropoulos, G. P. Wastewater Reclamation by Advanced Treatment of Secondary Effluents. *Desalination* **2006**, *195*, 109–118.

(5) Kang, G.; Cao, Y. Development of Antifouling Reverse Osmosis Membranes for Water Treatment: A Review. *Water Res.* **2012**, *46* (3), 584–600. https://doi.org/10.1016/j.watres.2011.11.041.

(6) Alvarez, P. J. J.; Chan, C. K.; Elimelech, M.; Halas, N. J.; Villagrán, D. Emerging Opportunities for Nanotechnology to Enhance Water Security. *Nat. Nanotechnol.* **2018**, *13* (8), 634–641. https://doi.org/10.1038/s41565-018-0203-2.

(7) Chappelle, C.; Mccann, H.; Jassby, D.; Schwabe, K.; Szeptycki, L. *Managing Wastewater in a Changing Climate*; 2019.

(8) Rosario-Ortiz, F.; Rose, J.; Speight, V.; Gunten, U. v.; Schnoor, J. How Do You like Your Tap Water? *Science (80-.).* **2016**, *351* (6276), 912–914. https://doi.org/10.1126/science.aaf0953.

(9) Kelley, C. P.; Mohtadi, S.; Cane, M. A.; Seager, R.; Kushnir, Y. Climate Change in the Fertile Crescent and Implications of the Recent Syrian Drought. *Proc. Natl. Acad. Sci.* **2015**, *112* (11), 3241–3246. https://doi.org/10.1073/pnas.1421533112.

(10) Jarusutthirak, C.; Amy, G. Membrane Filtration of Wastewater Effluents for Reuse: Effluent Organic Matter Rejection and Fouling. *Water Sci. Technol.* **2001**, *43* (10), 225–232.

(11) Jjemba, P. K.; Weinrich, L. A.; Cheng, W.; Giraldo, E.; LeChevallier, M. W. Regrowth of Potential Opportunistic Pathogens and Algae in Reclaimed-Water Distribution Systems. *Appl. Environ. Microbiol.* **2010**, *76* (13), 4169–4178. https://doi.org/10.1128/AEM.03147-09.

(12) Fujioka, T.; Khan, S. J.; McDonald, J. A.; Henderson, R. K.; Poussade, Y.; Drewes, J. E.; Nghiem, L. D. Effects of Membrane Fouling on N-Nitrosamine Rejection by Nanofiltration and Reverse Osmosis Membranes. *J. Memb. Sci.* **2013**, *427*, 311–319. https://doi.org/10.1016/j.memsci.2012.09.055.

(13) Kumar, M.; Payne, M. M.; Poust, S. K.; Zilles, J. L. Polymer-Based Biomimetic Membranes for Desalination. In *Biomimetic Membranes for Sensor and Separation Applications*; Hélix-Nielsen, C., Ed.; Springer Netherlands: Dordrecht, 2012; pp 43–62. https://doi.org/10.1007/978-94-007-2184-5_3.

(14) Wang, J.; Dlamini, D. S.; Mishra, A. K.; Theresa, M.; Pendergast, M. T. M.; Wong, M. C. Y. Y.; Mamba, B. B.; Freger, V.; Verliefde, A. R. D. D.; Hoek, E. M. V. V.

A Critical Review of Transport through Osmotic Membranes; 2014; Vol. 454, pp 516–537. https://doi.org/10.1016/j.memsci.2013.12.034.

(15) Lee, C. W.; Bae, S. D.; Han, S. W.; Kang, L. S. Application of Ultrafiltration Hybrid Membrane Processes for Reuse of Secondary Effluent. *Desalination* **2007**, *202* (1–3), 239–246. https://doi.org/10.1016/j.desal.2005.12.059.

(16) Werber, J. R.; Osuji, C. O.; Elimelech, M. Materials for Next-Generation Desalination and Water Purification Membranes. *Nat. Rev. Mater.* **2016**, *1* (5), 1–15. https://doi.org/10.1038/natrevmats.2016.18.

(17) Baker, R. W. Ultrafiltration. In *Membrane Technology and Applications*; Wiley; pp 237–274.

(18) Kang, S.; A, A.; Mayes, A.; Elimelech, M. Protein Antifouling Mechanisms of PAN UF Membranes Incorporating PAN-g-PEO Additive. *J. Memb. Sci.* **2007**, *296* (1–2), 42–50. https://doi.org/10.1016/j.memsci.2007.03.012.

(19) Zaky, A. M.; Escobar, I. C.; Gruden, C. L. Studying the Effect of Feed Water Characteristics on the Hydrophobicity of Cellulose Acetate Ultrafiltraion Membranes and Its Correlation to Membrane Morphology: A Chemical Force Microscopy Approach. *Mod. Appl. Membr. Sci. Technol. ACS Symp. Ser.* **2011**. https://doi.org/10.1021/bk-2011-1078.ch014.

(20) Bengani-Lutz, P.; Zaf, R. D.; Culfaz-Emecen, P. Z.; Asatekin, A. Extremely Fouling Resistant Zwitterionic Copolymer Membranes with ~ 1 Nm Pore Size for Treating Municipal, Oily and Textile Wastewater Streams. *J. Memb. Sci.* **2017**, *543*, 184–194. https://doi.org/10.1016/j.memsci.2017.08.058.

(21) Kumar, R.; Ismail, A. F. Fouling Control on Microfiltration/Ultrafiltration Membranes: Effects of Morphology, Hydrophilicity, and Charge. *J. Appl. Polym. Sci.* **2015**, *132* (21). https://doi.org/10.1002/app.42042.

(22) Lee, S.; Ang, W. S.; Elimelech, M. Fouling of Reverse Osmosis Membranes by Hydrophilic Organic Matter: Implications for Water Reuse. *Desalination* **2006**, *187*, 313–321.

(23) Inurria, A.; Cay-Durgun, P.; Rice, D.; Zhang, H.; Seo, D.-K.; Lind, M. L.; Perreault, F. Polyamide Thin-Film Nanocomposite Membranes with Graphene Oxide Nanosheets: Balancing Membrane Performance and Fouling Propensity. *Desalination* **2019**, *451*, 139–147. https://doi.org/10.1016/j.desal.2018.07.004.

(24) Farhat, N. M.; Vrouwenvelder, J. S.; Van Loosdrecht, M. C. M.; Bucs, S. S.; Staal, M. Effect of Water Temperature on Biofouling Development in Reverse Osmosis Membrane Systems. *Water Res.* **2016**, *103*, 149–159. https://doi.org/10.1016/j.watres.2016.07.015.

(25) Romero-Vargas Castrillón, S.; Lu, X.; Shaffer, D. L.; Elimelech, M. Amine Enrichment and Poly(Ethylene Glycol) (PEG) Surface Modification of Thin-Film Composite Forward Osmosis Membranes for Organic Fouling Control. *J. Memb. Sci.* **2014**, *450*, 331–339. https://doi.org/10.1016/j.memsci.2013.09.028.

(26) Al-Ahmad, M.; Abdul Aleem, F. A.; Mutiri, A.; Ubaisy, A. Biofuoling in RO Membrane Systems Part 1: Fundamentals and Control. *Desalination* **2000**, *132* (1–3), 173–179. https://doi.org/10.1016/S0011-9164(00)00146-6.

(27) Characklis, W. G.; Bryers, J. D. Fouling Biofilm Development: A Process Analysis. *Biotechnol. Bioeng.* **2009**, *102* (2), 309–347. https://doi.org/10.1002/bit.22227.

(28) Al-Amoudi, A. S. Factors Affecting Natural Organic Matter (NOM) and Scaling

Fouling in NF Membranes: A Review. *Desalination*. 2010, pp 1–10. https://doi.org/10.1016/j.desal.2010.04.003.

(29) Quay, A. N.; Tong, T.; Hashmi, S. M.; Zhou, Y.; Zhao, S.; Elimelech, M. Combined Organic Fouling and Inorganic Scaling in Reverse Osmosis: Role of Protein–Silica Interactions. *Environ. Sci. Technol.* **2018**, *52* (16), 9145–9153. https://doi.org/10.1021/acs.est.8b02194.

(30) Goh, P. S.; Lau, W. J.; Othman, M. H. D.; Ismail, A. F. Membrane Fouling in Desalination and Its Mitigation Strategies. *Desalination* **2018**, *425*, 130–155. https://doi.org/10.1016/j.desal.2017.10.018.

(31) Ang, W. S.; Elimelech, M. Protein (BSA) Fouling of Reverse Osmosis Membranes: Implications for Wastewater Reclamation. *J. Memb. Sci.* **2007**, *296* (1–2), 83–92. https://doi.org/10.1016/j.memsci.2007.03.018.

(32) Michael-Kordatou, I.; Michael, C.; Duan, X.; He, X.; Dionysiou, D. D.; Mills, M. A.; Fatta-Kassinos, D. Dissolved Effluent Organic Matter: Characteristics and Potential Implications in Wastewater Treatment and Reuse Applications. *Water Res.* **2015**, *77*, 213–248. https://doi.org/10.1016/j.watres.2015.03.011.

(33) Costa, A. R.; de Pinho, M. N. Effect of Membrane Pore Size and Solution Chemistry on the Ultrafiltration of Humic Substances Solutions. *J. Memb. Sci.* **2005**, *255* (1–2), 49–56. https://doi.org/10.1016/j.memsci.2005.01.016.

(34) Dufrene, Y. F.; Dufrêne, Y. F. Sticky Microbes: Forces in Microbial Cell Adhesion. *Trends Microbiol.* **2015**, *23* (6), 376–382. https://doi.org/10.1016/j.tim.2015.01.011.

(35) Geise, G. M.; Lee, H.-S.; Miller, D. J.; Freeman, B. D.; McGrath, J. E.; Paul, D. R. Water Purification by Membranes: The Role of Polymer Science. *J. Polym. Sci. Part B Polym. Phys.* **2010**, *48* (15), 1685–1718. https://doi.org/10.1002/polb.22037.

(36) Low, D.; Hamood, A.; Reid, T.; Mosley, T.; Tran, P.; Song, L.; Morse, A. Attachment of Selenium to a Reverse Osmosis Membrane to Inhibit Biofilm Formation of S. Aureus. *J. Memb. Sci.* **2011**, *378* (1–2), 171–178. https://doi.org/10.1016/j.memsci.2011.04.041.

(37) Subramani, A.; Huang, X.; Hoek, E. M. V. Direct Observation of Bacterial Deposition onto Clean and Organic-Fouled Polyamide Membranes. *J. Colloid Interface Sci.* **2009**, *336* (1), 13–20. https://doi.org/10.1016/j.jcis.2009.03.063.

(38) Garrett, T. R.; Bhakoo, M.; Zhang, Z. Bacterial Adhesion and Biofilms on Surfaces. *Prog. Nat. Sci.* **2008**, *18* (9), 1049–1056. https://doi.org/10.1016/j.pnsc.2008.04.001.

(39) Araújo, E. A.; de Andrade, N. J.; da Silva, L. H. M.; de Carvalho, A. F.; de Silva, C. A. S.; Ramos, A. M. Control of Microbial Adhesion as a Strategy for Food and Bioprocess Technology. *Food Bioprocess Technol.* **2010**, *3* (3), 321–332. https://doi.org/10.1007/s11947-009-0290-z.

(40) Lee, S.; Kim, S.; Cho, J.; Hoek, E. M. V. V. Natural Organic Matter Fouling Due to Foulant–Membrane Physicochemical Interactions. *Desalination* **2007**, *202* (1–3), 377–384. https://doi.org/10.1016/j.desal.2005.12.077.

(41) Jin, X.; Jawor, A.; Kim, S.; Hoek, E. M. V. V. Effects of Feed Water Temperature on Separation Performance and Organic Fouling of Brackish Water RO Membranes. *Desalination* **2009**, *239* (1–3), 346–359. https://doi.org/10.1016/j.desal.2008.03.026.

(42) Mo, H.; Tay, K. G.; Ng, H. Y.; Guan Tay, K.; Yong Ng, H. Fouling of Reverse Osmosis Membrane by Protein (BSA): Effects of PH, Calcium, Magnesium, Ionic Strength and Temperature. *J. Memb. Sci.* **2008**, *315*, 28–35.

https://doi.org/10.1016/j.memsci.2008.02.002.
(43) Goosen, M. F. A.; Sablani, S. S.; Al-Maskari, S. S.; Al-Belushi, R. H.; Wilf, M. Effect of Feed Temperature on Permeate Flux and Mass Transfer Coefficient in Spiral-Wound Reverse Osmosis Systems. *Desalination* **2002**, *144* (1–3), 367–372. https://doi.org/10.1016/S0011-9164(02)00345-4.
(44) Goosen, M. F. A. A.; Sablani, S.; Cin, M. D.; Wilf, M. Effect of Cyclic Changes in Temperature and Pressure on Permeation Properties of Composite Polyamide Seawater Reverse Osmosis Membranes. *Sep. Sci. Technol.* **2010**, *46* (1), 14–26. https://doi.org/10.1080/01496395.2010.502552.
(45) Hoffman, A. S. Non-Fouling Surface Technologies. *J. Biomater. Sci. Polym. Ed.* **1999**, *10* (10), 1011–1014. https://doi.org/10.1163/156856299X00658.
(46) Matin, A.; Khan, Z.; Zaidi, S. M. J.; Boyce, M. C. Biofouling in Reverse Osmosis Membranes for Seawater Desalination: Phenomena and Prevention. *Desalination* **2011**, *281* (1), 1–16. https://doi.org/10.1016/j.desal.2011.06.063.
(47) Habimana, O.; Semião, A. J. C.; Casey, E. The Role of Cell-Surface Interactions in Bacterial Initial Adhesion and Consequent Biofilm Formation on Nanofiltration/Reverse Osmosis Membranes. *J. Memb. Sci.* **2014**, *454*, 82–96. https://doi.org/10.1016/j.memsci.2013.11.043.
(48) Li, Q.; Xu, Z.; Pinnau, I. Fouling of Reverse Osmosis Membranes by Biopolymers in Wastewater Secondary Effluent: Role of Membrane Surface Properties and Initial Permeate Flux. *J. Memb. Sci.* **2007**, *290* (1–2), 173–181. https://doi.org/10.1016/j.memsci.2006.12.027.
(49) Kasemset, S.; He, Z.; Miller, D. J.; Freeman, B. D.; Sharma, M. M. Effect of Polydopamine Deposition Conditions on Polysulfone Ultrafiltration Membrane Properties and Threshold Flux during Oil/Water Emulsion Filtration. *Polymer (Guildf).* **2016**, *97*, 247–257. https://doi.org/10.1016/j.polymer.2016.04.064.
(50) Zeng, G.; Müller, T.; Meyer, R. L. Single-Cell Force Spectroscopy of Bacteria Enabled by Naturally Derived Proteins. *Langmuir* **2014**, *30* (14), 4019–4025. https://doi.org/10.1021/la404673q.
(51) Beaussart, A.; El-Kirat-Chatel, S.; Sullan, R. M. A.; Alsteens, D.; Herman, P.; Derclaye, S.; Dufrêne, Y. F. Quantifying the Forces Guiding Microbial Cell Adhesion Using Single-Cell Force Spectroscopy. *Nat. Protoc.* **2014**, *9* (5), 1049–1055. https://doi.org/10.1038/nprot.2014.066.
(52) Thewes, N.; Thewes, A.; Loskill, P.; Peisker, H.; Bischoff, M.; Herrmann, M.; Santen, L.; Jacobs, K. Stochastic Binding of Staphylococcus Aureus to Hydrophobic Surfaces. *Soft Matter* **2015**, *11* (46), 8913–8919. https://doi.org/10.1039/C5SM00963D.
(53) Hugel, T.; Seitz, M. The Study of Molecular Interactions by AFM Force Spectroscopy. *Macromolecular Rapid Communications*. 2001, pp 989–1016. https://doi.org/10.1002/1521-3927(20010901)22:13<989::AID-MARC989>3.0.CO;2-D.
(54) Singh, G.; Bremmell, K.; Griesser, H. J.; Kingshott, P. Colloid-Probe AFM Studies of the Surface Functionality and Adsorbed Proteins on Binary Colloidal Crystal Layers. *RSC Adv.* **2017**, *7* (12), 7329–7337. https://doi.org/10.1039/c6ra28491d.
(55) Kappl, M.; Butt, H.-J. The Colloidal Probe Technique and Its Application to Adhesion Force Measurements. *Part. Part. Syst. Charact.* **2002**, *19* (3), 129–143.

https://doi.org/10.1002/1521-4117(200207)19:3<129::AID-PPSC129>3.0.CO;2-G.
(56) Lu, X.; Arias Chavez, L. H.; Romero-Vargas Castrillón, S.; Ma, J.; Elimelech, M. Influence of Active Layer and Support Layer Surface Structures on Organic Fouling Propensity of Thin-Film Composite Forward Osmosis Membranes. *Environ. Sci. Technol.* **2015**, *49* (3), 1436–1444. https://doi.org/10.1021/es5044062.
(57) Aubry, C.; Gutierrez, L.; Croue, J. P. Coating of AFM Probes with Aquatic Humic and Non-Humic NOM to Study Their Adhesion Properties. *Water Res.* **2013**, *47* (9), 3109–3119. https://doi.org/10.1016/j.watres.2013.03.023.
(58) Gutierrez, L.; Aubry, C.; Valladares Linares, R.; Croue, J.-P. Natural Organic Matter Interactions with Polyamide and Polysulfone Membranes: Formation of Conditioning Film. *Colloids Surfaces A Physicochem. Eng. Asp.* **2015**, *477* (477), 1–8. https://doi.org/10.1016/j.colsurfa.2015.03.031.
(59) Abu-Lail, L. I.; Liu, Y.; Atabek, A.; Camesano, T. A. Quantifying the Adhesion and Interaction Forces Between Pseudomonas Aeruginosa and Natural Organic Matter. *Environ. Sci. Technol.* **2007**, *41* (23), 8031–8037. https://doi.org/10.1021/es071047o.
(60) Lee, S.; Elimelech, M. Relating Organic Fouling of Reverse Osmosis Membranes to Intermolecular Adhesion Forces. *Environ. Sci. Technol.* **2006**, *40* (3), 980–987. https://doi.org/10.1021/es051825h.
(61) Mi, B.; Elimelech, M. Organic Fouling of Forward Osmosis Membranes: Fouling Reversibility and Cleaning without Chemical Reagents. *J. Memb. Sci.* **2010**, *348* (1–2), 337–345. https://doi.org/10.1016/j.memsci.2009.11.021.
(62) Wang, L.; Miao, R.; Wang, X.; Lv, Y.; Meng, X.; Yang, Y.; Huang, D.; Feng, L.; Liu, Z.; Ju, K. Fouling Behavior of Typical Organic Foulants in Polyvinylidene Fluoride Ultrafiltration Membranes: Characterization from Microforces. *Environ. Sci. Technol.* **2013**, *47* (8), 3708–3714. https://doi.org/10.1021/es4004119.
(63) Ang, W. S.; Lee, S.; Elimelech, M. Chemical and Physical Aspects of Cleaning of Organic-Fouled Reverse Osmosis Membranes. *J. Memb. Sci.* **2006**, *272* (1–2), 198–210. https://doi.org/10.1016/j.memsci.2005.07.035.
(64) Geise, G. M.; Paul, D. R.; Freeman, B. D. Fundamental Water and Salt Transport Properties of Polymeric Materials. *Progress in Polymer Science*. 2014, pp 1–24. https://doi.org/10.1016/j.progpolymsci.2013.07.001.
(65) Lind, M. L.; Suk, D. E.; Nguyen, T. V.; Hoek, E. M. V. Tailoring the Structure of Thin Film Nanocomposite Membranes to Achieve Seawater RO Membrane Performance. *Environ. Sci. Technol.* **2010**, *44* (21), 8230–8235. https://doi.org/10.1021/es101569p.
(66) Geise, G. M.; Park, H. B.; Sagle, A. C.; Freeman, B. D.; McGrath, J. E. Water Permeability and Water/Salt Selectivity Tradeoff in Polymers for Desalination. *J. Memb. Sci.* **2011**, *369* (1–2), 130–138. https://doi.org/10.1016/j.memsci.2010.11.054.
(67) Benjamin, M. M.; Lawler, D. F. Membrane Processes. In *Water Quality Engineering Physical/Chemical Treatment Processes*; John Wiley & Sons, Inc.: Hoboken, NJ, 2013; pp 731–845.
(68) Baghdadi, Y. N.; Alnouri, S. Y.; Matsuura, T.; Tarboush, B. J. A. Temperature Effects on Concentration Polarization Thickness in Thin-Film Composite Reverse Osmosis Membranes. *Chem. Eng. Technol.* **2018**, *41* (10), 1905–1912.

https://doi.org/10.1002/ceat.201800184.
(69) Jawor, A.; Hoek, E. M. V. Effects of Feed Water Temperature on Inorganic Fouling of Brackish Water RO Membranes. *Desalination* **2009**, *235* (1–3), 44–57. https://doi.org/10.1016/j.desal.2008.07.004.
(70) Agashichev, S. P.; Lootah, K. N. Influence of Temperature and Permeate Recovery on Energy Consumption of a Reverse Osmosis System. *Desalination* **2003**, *154* (3), 253–266. https://doi.org/10.1016/S0011-9164(03)80041-3.
(71) Liu, S.; Gunawan, C.; Barraud, N.; Rice, S. A.; Harry, E. J.; Amal, R. Understanding, Monitoring, and Controlling Biofilm Growth in Drinking Water Distribution Systems. *Environ. Sci. Technol.* **2016**, *50* (17), 8954–8976. https://doi.org/10.1021/acs.est.6b00835.
(72) BinAhmed, S.; Hasane, A.; Wang, Z.; Mansurov, A.; Romero-Vargas Castrillón, S. Bacterial Adhesion to Ultrafiltration Membranes: Role of Hydrophilicity, Natural Organic Matter, and Cell-Surface Macromolecules. *Environ. Sci. Technol.* **2018**, *52* (1), 162–172. https://doi.org/10.1021/acs.est.7b03682.
(73) Lee, H.; Dellatore, S. M.; Miller, W. M.; Messersmith, P. B. Mussel-Inspired Surface Chemistry for Multifunctional Coatings. *Science* **2007**, *318* (5849), 426–430. https://doi.org/10.1126/science.1147241.
(74) Wuolo-Journey, K.; Binahmed, S.; Linna, E.; Romero-Vargas Castrillón, S. Do Graphene Oxide Nanostructured Coatings Mitigate Bacterial Adhesion? *Environ. Sci. Nano* **2019**, *6* (9), 2863–2875. https://doi.org/10.1039/c9en00499h.
(75) Costerton, J. W. Bacterial Biofilms: A Common Cause of Persistent Infections. *Science (80-.).* **1999**, *284* (5418), 1318–1322. https://doi.org/10.1126/science.284.5418.1318.
(76) Busscher, H. J.; van der Mei, H. C. How Do Bacteria Know They Are on a Surface and Regulate Their Response to an Adhering State? *PLoS Pathog.* **2012**, *8* (1), 1–3. https://doi.org/10.1371/journal.ppat.1002440.
(77) Vlamakis, H.; Chai, Y.; Beauregard, P.; Losick, R.; Kolter, R. Sticking Together: Building a Biofilm the Bacillus Subtilis Way. *Nat. Rev. Microbiol.* **2013**, *11* (3), 157–168. https://doi.org/10.1038/nrmicro2960.
(78) Bazaka, K.; Jacob, M. V.; Crawford, R. J.; Ivanova, E. P. Efficient Surface Modification of Biomaterial to Prevent Biofilm Formation and the Attachment of Microorganisms. *Appl. Microbiol. Biotechnol.* **2012**, *95* (2), 299–311. https://doi.org/10.1007/s00253-012-4144-7.
(79) Allen, A.; Semião, A. J. C.; Habimana, O.; Heffernan, R.; Safari, A.; Casey, E. Nanofiltration and Reverse Osmosis Surface Topographical Heterogeneities: Do They Matter for Initial Bacterial Adhesion? *J. Memb. Sci.* **2015**, *486*, 10–20. https://doi.org/10.1016/j.memsci.2015.03.029.
(80) Friedlander, R. S.; Vogel, N.; Aizenberg, J. Role of Flagella in Adhesion of *Escherichia Coli* to Abiotic Surfaces. *Langmuir* **2015**, *31* (22), 6137–6144. https://doi.org/10.1021/acs.langmuir.5b00815.
(81) Quirynen, M.; Dierickx, K.; van Steenberghe, D. Effects of Surface Roughness and Free Energy on Oral Bacterial Adhesion. In *Handbook of Bacterial Adhesion Principles, Methods, and Applications*; An, Y. H., Friedman, R. J., Eds.; Humana Press Inc.: Totowa, NJ, 2000; pp 91–102.
(82) An, Y. H.; Dickinson, R. B.; Doyle, R. J. Mechanisms of Bacterial Adhesion and

Pathogenesis of Implant and Tissue Infections. In *Handbook of Bacterial Adhesion Principles, Methods, and Applications*; An, Y. H., Friedman, R. J., Eds.; Humana Press Inc.: Totowa, NJ, 2000; pp 1–27.

(83) El-Kirat-Chatel, S.; Boyd, C. D.; O'Toole, G. A.; Dufrêne, Y. F. Single-Molecule Analysis of Pseudomonas Fluorescens Footprints. *ACS Nano* **2014**, *8* (2), 1690–1698. https://doi.org/10.1021/nn4060489.

(84) El-Kirat-Chatel, S.; Beaussart, A.; Boyd, C. D.; O'Toole, G. A.; Dufrêne, Y. F. Single-Cell and Single-Molecule Analysis Deciphers the Localization, Adhesion, and Mechanics of the Biofilm Adhesin LapA. *ACS Chem. Biol.* **2014**, *9* (2), 485–494. https://doi.org/10.1021/cb400794e.

(85) Sullan, R. M. A.; Beaussart, A.; Tripathi, P.; Derclaye, S.; El-Kirat-Chatel, S.; Li, J. K.; Schneider, Y.-J.; Vanderleyden, J.; Lebeer, S.; Dufrêne, Y. F. Single-Cell Force Spectroscopy of Pili-Mediated Adhesion. *Nanoscale* **2014**, *6* (2), 1134–1143. https://doi.org/10.1039/C3NR05462D.

(86) Camesano, T. A.; Liu, Y.; Datta, M. Measuring Bacterial Adhesion at Environmental Interfaces with Single-Cell and Single-Molecule Techniques. *Adv. Water Resour.* **2007**, *30* (6–7), 1470–1491. https://doi.org/10.1016/j.advwatres.2006.05.023.

(87) Van Loosdrecht, M. C. M.; Lyklema, J.; Norde, W.; Zehnder, A. J. B.; Zehnder ', A. J. B. Bacterial Adhesion: A Physicochemical Approach. *Source Microb. Ecol. Microb Ecol Microb. Ecol.* **1989**, *17* (17), 1–15.

(88) Donnarumma, G.; Buommino, E.; Fusco, A.; Paoletti, I.; Auricchio, L.; Tufano, M. . Effect of Temperature on the Shift of Pseudomonas Fluorescens from an Environmental Microorganism to a Potential Human Pathogen. *Int. J. Immunopathol. Pharmacol.* **2010**, *3* (1), 227–234. https://doi.org/10.1177/039463201002300120.

(89) Ong, Y. L.; Razatos, A.; Georgiou, G.; Sharma, M. M. Adhesion Forces between E. Coli Bacteria and Biomaterial Surfaces. *Langmuir* **1999**, *15* (8), 2719–2725. https://doi.org/10.1021/la981104e.

(90) Miller, D. J.; Araújo, P. A.; Correia, P. B.; Ramsey, M. M.; Kruithof, J. C.; van Loosdrecht, M. C. M. M.; Freeman, B. D.; Paul, D. R.; Whiteley, M.; Vrouwenvelder, J. S.; Araujo, P. A.; Correia, P. B.; Ramsey, M. M.; Kruithof, J. C.; van Loosdrecht, M. C. M. M.; Freeman, B. D.; Paul, D. R.; Whiteley, M.; Vrouwenvelder, J. S. Short-Term Adhesion and Long-Term Biofouling Testing of Polydopamine and Poly(Ethylene Glycol) Surface Modifications of Membranes and Feed Spacers for Biofouling Control. *Water Res.* **2012**, *46* (12), 3737–3753. https://doi.org/10.1016/j.watres.2012.03.058.

(91) Howe, K. J.; Clark, M. M. Fouling of Microfiltration and Ultrafiltration Membranes by Natural Waters. *Environ. Sci. Technol.* **2002**, *36* (16), 3571–3576. https://doi.org/10.1021/es025587r.

(92) Chamberlain, A. H. L. The Role of Adsorbed Layers in Bacterial Adhesion. In *Biofilms - Science and Technology*; Springer Netherlands: Dordrecht, 1992; pp 59–67. https://doi.org/10.1007/978-94-011-1824-8_6.

(93) Palmer, J.; Flint, S.; Brooks, J. Bacterial Cell Attachment, the Beginning of a Biofilm. *J. Ind. Microbiol. Biotechnol.* **2007**, *34* (9), 577–588. https://doi.org/10.1007/s10295-007-0234-4.

(94) Yuan, B.; Pham, M.; Nguyen, T. H. Deposition Kinetics of Bacteriophage MS2 on a Silica Surface Coated with Natural Organic Matter in a Radial Stagnation Point Flow Cell. *Environ. Sci. Technol.* **2008**, *42* (20), 7628–7633. https://doi.org/10.1021/es801003s.
(95) de Kerchove, A. J.; Weroński, P.; Elimelech, M. Adhesion of Nonmotile Pseudomonas Aeruginosa on "Soft" Polyelectrolyte Layer in a Radial Stagnation Point Flow System: Measurements and Model Predictions. *Langmuir* **2007**, *23* (24), 12301–12308. https://doi.org/10.1021/la701936x.
(96) Marshall, K. C.; Stout, R.; Mitchell, R. Selective Sorption of Bacteria from Seawater. *Can. J. Microbiol.* **1971**, *17* (11), 1413–1416. https://doi.org/10.1139/m71-225.
(97) Liu, Y.; Janjaroen, D.; Kuhlenschmidt, M. S.; Kuhlenschmidt, T. B.; Nguyen, T. H. Deposition of Cryptosporidium Parvum Oocysts on Natural Organic Matter Surfaces: Microscopic Evidence for Secondary Minimum Deposition in a Radial Stagnation Point Flow Cell. *Langmuir* **2009**, *25* (3), 1594–1605. https://doi.org/10.1021/la803202h.
(98) Parent, M. E.; Velegol, D. E. Coli Adhesion to Silica in the Presence of Humic Acid. *Colloids Surfaces B Biointerfaces* **2004**, *39* (1–2), 45–51. https://doi.org/10.1016/j.colsurfb.2004.08.020.
(99) Yang, H.; Kim, H.; Tong, M. Influence of Humic Acid on the Transport Behavior of Bacteria in Quartz Sand. *Colloids Surfaces B Biointerfaces* **2012**, *91*, 122–129. https://doi.org/10.1016/j.colsurfb.2011.10.058.
(100) Fein, J. B.; Boily, J.-F.; Güçlü, K.; Kaulbach, E. Experimental Study of Humic Acid Adsorption onto Bacteria and Al-Oxide Mineral Surfaces. *Chem. Geol.* **1999**, *162* (1), 33–45. https://doi.org/10.1016/S0009-2541(99)00075-3.
(101) Gaboriaud, F.; Dufrêne, Y. F. Atomic Force Microscopy of Microbial Cells: Application to Nanomechanical Properties, Surface Forces and Molecular Recognition Forces. *Colloids Surfaces B Biointerfaces* **2007**, *54* (1), 10–19. https://doi.org/10.1016/j.colsurfb.2006.09.014.
(102) Francius, G.; Alsteens, D.; Dupres, V.; Lebeer, S.; De Keersmaecker, S.; Vanderleyden, J.; Gruber, H. J.; Dufrêne, Y. F. Stretching Polysaccharides on Live Cells Using Single Molecule Force Spectroscopy. *Nat. Protoc.* **2009**, *4* (6), 939–946. https://doi.org/10.1038/nprot.2009.65.
(103) Dufrêne, Y. F. Sticky Microbes: Forces in Microbial Cell Adhesion. *Trends Microbiol.* **2015**, *23* (6), 376–382. https://doi.org/10.1016/j.tim.2015.01.011.
(104) Hinsa, S. M.; Espinosa-Urgel, M.; Ramos, J. L.; O'Toole, G. A. Transition from Reversible to Irreversible Attachment during Biofilm Formation by Pseudomonas Fluorescens WCS365 Requires an ABC Transporter and a Large Secreted Protein. *Mol. Microbiol.* **2003**, *49* (4), 905–918. https://doi.org/10.1046/j.1365-2958.2003.03615.x.
(105) Tolker-Nielsen, T.; Molin, S. The Biofilm Lifestyle of Pseudomonas. *Pseudomonas, V1*; Ramos, J.-L., Ed.; Kluwer Academic/Plenum Publishers, 2004; pp 547–571.
(106) Malheiro, J.; Araújo, P.; Machado, I.; Lemos, M.; Mergulhão, F.; Melo, L.; Simões, M. The Effects of Selected Brominated and Chlorinated Chemicals on Pseudomonas Fluorescens Planktonic Cells and Flow-Generated Biofilms. *J. Food Process. Preserv.* **2016**, *40* (2), 316–328. https://doi.org/10.1111/jfpp.12609.
(107) Pereira, M. O.; Vieira, M. J. Effects of the Interactions between Glutaraldehyde and

the Polymeric Matrix on the Efficacy of the Biocide against Pseudomonas Fluorescens Biofilms. *Biofouling* **2001**, *17* (2), 93–101. https://doi.org/10.1080/08927010109378469.

(108) Mulder, M. Preparation of Synthetic Membranes. In *Basic Principles of Membrane Technology*; Springer Netherlands: Dordrecht, 1996; pp 71–156. https://doi.org/10.1007/978-94-009-1766-8.

(109) Elomari, M.; Coroler, L.; Izard, D.; Leclerc, H. A Numerical Taxonomic Study of Fluorescent Pseudomonas Strains Isolated from Natural Mineral Waters. *J. Appl. Bacteriol.* **1995**, *78* (1), 71–81. https://doi.org/10.1111/j.1365-2672.1995.tb01676.x.

(110) Picot, L.; Abdelmoula, S. M.; Merieau, A.; Leroux, P.; Cazin, L.; Orange, N.; Feuilloley, M. G. . Pseudomonas Fluorescens as a Potential Pathogen: Adherence to Nerve Cells. *Microbes Infect.* **2001**, *3* (12), 985–995. https://doi.org/10.1016/S1286-4579(01)01462-9.

(111) Ivanov, I. E.; Boyd, C. D.; Newell, P. D.; Schwartz, M. E.; Turnbull, L.; Johnson, M. S.; Whitchurch, C. B.; O'Toole, G. A.; Camesano, T. A. Atomic Force and Super-Resolution Microscopy Support a Role for LapA as a Cell-Surface Biofilm Adhesin of Pseudomonas Fluorescens. *Res. Microbiol.* **2012**, *163* (9–10), 685–691. https://doi.org/10.1016/j.resmic.2012.10.001.

(112) Tamber, S.; Hancock, R. E. W. The Outer Membranes of Pseudomonas. *Pseudomonas, V1*; Ramos, J.-L., Ed.; Kluwer Academic/Plenum Publishers, 2004; pp 575–601.

(113) Dasgupta, N.; Arora, S.; Ramphal, R. The Flagellar System of Pseudomonas Aeruginosa. *Pseudomonas, V1*; Kluwer Academic/Plenum Publishers, 2004; pp 675–698.

(114) Isaacson, R. E. Pilus Adhesins. In *Bacterial Adhesion Mechanisms and Physiological Significance*; Savage, D. C., Fletcher, M., Eds.; Plenum Press: Boston, MA, 1985; pp 307–336.

(115) Vesper, S. J. Production of Pili (Fimbriae) by Pseudomonas Fluorescens and Correlation with Attachment to Corn Roots. *Appl. Environ. Microbiol.* **1987**, *53* (7), 1397–1405.

(116) Kim, D.; Jung, S.; Sohn, J.; Kim, H.; Lee, S. Biocide Application for Controlling Biofouling of SWRO Membranes - an Overview. *Desalination* **2009**, *238* (1–3), 43–52. https://doi.org/10.1016/j.desal.2008.01.034.

(117) Herzberg, M.; Elimelech, M. Biofouling of Reverse Osmosis Membranes: Role of Biofilm-Enhanced Osmotic Pressure. *J. Memb. Sci.* **2007**, *295* (1–2), 11–20. https://doi.org/10.1016/j.memsci.2007.02.024.

(118) Thewes, N.; Loskill, P.; Jung, P.; Peisker, H.; Bischoff, M.; Herrmann, M.; Jacobs, K. Hydrophobic Interaction Governs Unspecific Adhesion of Staphylococci: A Single Cell Force Spectroscopy Study. *Beilstein J. Nanotechnol.* **2014**, *5*, 1501–1512. https://doi.org/10.3762/bjnano.5.163.

(119) Kang, S.; Elimelech, M. Bioinspired Single Bacterial Cell Force Spectroscopy. *Langmuir* **2009**, *25* (17), 9656–9659. https://doi.org/10.1021/la902247w.

(120) Tang, L.; Livi, K. J. T.; Chen, K. L. Polysulfone Membranes Modified with Bioinspired Polydopamine and Silver Nanoparticles Formed in Situ To Mitigate Biofouling. *Environ. Sci. Technol. Lett.* **2015**, *2* (3), 59–65. https://doi.org/10.1021/acs.estlett.5b00008.

(121) McCloskey, B. D.; Park, H. B.; Ju, H.; Rowe, B. W.; Miller, D. J.; Chun, B. J.; Kin, K.; Freeman, B. D.; Bum Park, H.; Ju, H.; Rowe, B. W.; Miller, D. J.; Jae Chun, B.; Kin, K.; Freeman, B. D. Influence of Polydopamine Deposition Conditions on Pure Water Flux and Foulant Adhesion Resistance of Reverse Osmosis, Ultrafiltration, and Microfiltration Membranes. *Polymer (Guildf).* **2010**, *51* (15), 3472–3485. https://doi.org/10.1016/j.polymer.2010.05.008.
(122) Wei, Q.; Zhang, F.; Li, J.; Li, B.; Zhao, C. Oxidant-Induced Dopamine Polymerization for Multifunctional Coatings. *Polym. Chem.* **2010**, *1* (9), 1430. https://doi.org/10.1039/c0py00215a.
(123) van der Leeden, M. C. Are Conformational Changes, Induced by Osmotic Pressure Variations, the Underlying Mechanism of Controlling the Adhesive Activity of Mussel Adhesive Proteins? *Langmuir* **2005**, *21* (24), 11373–11379. https://doi.org/10.1021/la0515468.
(124) Lee, H.; Scherer, N. F.; Messersmith, P. B. Single-Molecule Mechanics of Mussel Adhesion. *Proc. Natl. Acad. Sci.* **2006**, *103* (35), 12999–13003. https://doi.org/10.1073/pnas.0605552103.
(125) Lee, H.; Rho, J.; Messersmith, P. B. Facile Conjugation of Biomolecules onto Surfaces via Mussel Adhesive Protein Inspired Coatings. *Adv. Mater.* **2009**, *21* (4), 431–434. https://doi.org/10.1002/adma.200801222.
(126) Dreyer, D. R.; Miller, D. J.; Freeman, B. D.; Paul, D. R.; Bielawski, C. W. Elucidating the Structure of Poly(Dopamine). *Langmuir* **2012**, *28* (15), 6428–6435. https://doi.org/10.1021/la204831b.
(127) Ding, Y.; Weng, L.-T.; Yang, M.; Yang, Z.; Lu, X.; Huang, N.; Leng, Y. Insights into the Aggregation/Deposition and Structure of a Polydopamine Film. *Langmuir* **2014**, *30* (41), 12258–12269. https://doi.org/10.1021/la5026608.
(128) Liebscher, J.; Mrówczyński, R.; Scheidt, H. A.; Filip, C.; Hădade, N. D.; Turcu, R.; Bende, A.; Beck, S. Structure of Polydopamine: A Never-Ending Story? *Langmuir* **2013**, *29* (33), 10539–10548. https://doi.org/10.1021/la4020288.
(129) Hutter, J. L.; Bechhoefer, J. Calibration of Atomic-Force Microscope Tips. *Rev. Sci. Instrum.* **1993**, *64* (7), 1868–1873.
(130) Senden, T. J. Force Microscopy and Surface Interactions. *Curr. Opin. Colloid Interface Sci.* **2001**, *6* (2), 95–101. https://doi.org/10.1016/S1359-0294(01)00067-X.
(131) Zangmeister, R. A.; Morris, T. A.; Tarlov, M. J. Characterization of Polydopamine Thin Films Deposited at Short Times by Autoxidation of Dopamine. *Langmuir* **2013**, *29* (27), 8619–8628. https://doi.org/10.1021/la400587j.
(132) Waite, J. H. Surface Chemistry: Mussel Power. *Nat. Mater.* **2008**, *7* (1), 8–9. https://doi.org/10.1038/nmat2087.
(133) Jiang, J.; Zhu, L. L.; Zhu, L. L.; Zhu, B.; Xu, Y. Surface Characteristics of a Self-Polymerized Dopamine Coating Deposited on Hydrophobic Polymer Films. *Langmuir* **2011**, *27* (23), 14180–14187. https://doi.org/10.1021/la202877k.
(134) Lee, N.; Amy, G.; Croué, J. P.; Buisson, H. Identification and Understanding of Fouling in Low-Pressure Membrane (MF/UF) Filtration by Natural Organic Matter (NOM). *Water Res.* **2004**, *38* (20), 4511–4523. https://doi.org/10.1016/j.watres.2004.08.013.
(135) Cho, J.; Amy, G.; Pellegrino, J.; Yoon, Y. Characterization of Clean and Natural

Organic Matter (NOM) Fouled NF and UF Membranes, and Foulants Characterization. *Desalination* **1998**, *118* (1–3), 101–108. https://doi.org/10.1016/S0011-9164(98)00100-3.
(136) Jermann, D.; Pronk, W.; Meylan, S.; Boller, M. Interplay of Different NOM Fouling Mechanisms during Ultrafiltration for Drinking Water Production. *Water Res.* **2007**, *41* (8), 1713–1722. https://doi.org/10.1016/j.watres.2006.12.030.
(137) Zularisam, A. W. W.; Ismail, A. F. F.; Salim, R. Behaviours of Natural Organic Matter in Membrane Filtration for Surface Water Treatment — a Review. *Desalination* **2006**, *194* (1–3), 211–231. https://doi.org/10.1016/j.desal.2005.10.030.
(138) Meritt, K.; An, Y. H. Factors Influencing Bacterial Adhesion. In *Handbook of Bacterial Adhesion Principles, Methods, and Applications*; An, Y. H., Friedman, R. J., Eds.; Humana Press Inc.: Totowa, NJ, 2000; pp 53–72.
(139) Zhao, W.; Yang, S.; Huang, Q.; Cai, P. Bacterial Cell Surface Properties: Role of Loosely Bound Extracellular Polymeric Substances (LB-EPS). *Colloids Surfaces B Biointerfaces* **2015**, *128*, 600–607. https://doi.org/10.1016/j.colsurfb.2015.03.017.
(140) Zhao, W.; Walker, S. L.; Huang, Q.; Cai, P. Adhesion of Bacterial Pathogens to Soil Colloidal Particles: Influences of Cell Type, Natural Organic Matter, and Solution Chemistry. *Water Res.* **2014**, *53*, 35–46. https://doi.org/10.1016/j.watres.2014.01.009.
(141) Li, J.; McLandsborough, L. . The Effects of the Surface Charge and Hydrophobicity of Escherichia Coli on Its Adhesion to Beef Muscle. *Int. J. Food Microbiol.* **1999**, *53* (2), 185–193. https://doi.org/10.1016/S0168-1605(99)00159-2.
(142) Hoek, E. M. V; Bhattacharjee, S.; Elimelech, M. Effect of Membrane Surface Roughness on Colloid−Membrane DLVO Interactions. *Langmuir* **2003**, *19* (11), 4836–4847. https://doi.org/10.1021/la027083c.
(143) Boussu, K.; Van der Bruggen, B.; Volodin, A.; Snauwaert, J.; Van Haesendonck, C.; Vandecasteele, C. Roughness and Hydrophobicity Studies of Nanofiltration Membranes Using Different Modes of AFM. *J. Colloid Interface Sci.* **2005**, *286* (2), 632–638. https://doi.org/10.1016/j.jcis.2005.01.095.
(144) Mehta, A.; Zydney, A. L. Permeability and Selectivity Analysis for Ultrafiltration Membranes. *J. Memb. Sci.* **2005**, *249* (1–2), 245–249. https://doi.org/10.1016/j.memsci.2004.09.040.
(145) Kweon, J. H.; Lawler, D. F. Evaluating Precipitative Softening as a Pretreatment for Ultrafiltration of a Natural Water. *Environ. Eng. Sci.* **2002**, *19* (6), 531–544. https://doi.org/10.1089/109287502320963481.
(146) McLoughlin, S. Y.; Kastantin, M.; Schwartz, D. K.; Kaar, J. L. Single-Molecule Resolution of Protein Structure and Interfacial Dynamics on Biomaterial Surfaces. *Proc. Natl. Acad. Sci.* **2013**, *110* (48), 19396–19401. https://doi.org/10.1073/pnas.1311761110.
(147) Hinsa, S. M.; O'Toole, G. A. Mechanisms of Adhesion by Pseudomonas. *Pseudomonas, V1*; Kluwer Academic/Plenum Publishers, 2004; pp 699–720.
(148) Touhami, A.; Jericho, M. H.; Boyd, J. M.; Beveridge, T. J. Nanoscale Characterization and Determination of Adhesion Forces of Pseudomonas Aeruginosa Pili by Using Atomic Force Microscopy. *J. Bacteriol.* **2005**, *188* (2), 370–377. https://doi.org/10.1128/JB.188.2.370-377.2006.
(149) Docter, D.; Westmeier, D.; Markiewicz, M.; Stolte, S.; Knauer, S. K.; Stauber, R.

H. The Nanoparticle Biomolecule Corona: Lessons Learned - Challenge Accepted? *Chem. Soc. Rev.* **2015**, *44* (17), 6094–6121. https://doi.org/10.1039/c5cs00217f.
(150) Merritt, K.; An, Y. H. Factors Influencing Bacterial Adhesion. In *Handbook of Bacterial Adhesion Principles, Methods, and Applications*; An, Y. H., Friedman, R. J., Eds.; Humana Press Inc., 2000; pp 53–72.
(151) Meadows, P. Y.; Bemis, J. E.; Walker, G. C. Single-Molecule Force Spectroscopy of Isolated and Aggregated Fibronectin Proteins on Negatively Charged Surfaces in Aqueous Liquids. *Langmuir* **2003**, *19* (23), 9566–9572. https://doi.org/10.1021/la035217w.
(152) Dexter, S. C. Influence of Substratum Critical Surface Tension on Bacterial Adhesion—in Situ Studies. *J. Colloid Interface Sci.* **1979**, *70* (2), 346–354. https://doi.org/10.1016/0021-9797(79)90038-9.
(153) Ahn, W. Y.; Kalinichev, A. G.; Clark, M. M. Effects of Background Cations on the Fouling of Polyethersulfone Membranes by Natural Organic Matter: Experimental and Molecular Modeling Study. *J. Memb. Sci.* **2008**, *309* (1–2), 128–140. https://doi.org/10.1016/j.memsci.2007.10.023.
(154) Laîné, J.-M.; Hagstrom, J. P.; Clark, M. M.; Mallevialle, J. Effects of Ultrafiltration Membrane Composition. *J. Am. Water Works Assoc.* **1989**, *81* (11), 61–67.
(155) Pablos, C.; van Grieken, R.; Marugán, J.; Chowdhury, I.; Walker, S. L. Study of Bacterial Adhesion onto Immobilized TiO2: Effect on the Photocatalytic Activity for Disinfection Applications. *Catal. Today* **2013**, *209*, 140–146. https://doi.org/10.1016/j.cattod.2012.12.010.
(156) Koh, L.; Ahn, W.; Clark, M. Selective Adsorption of Natural Organic Foulants by Polysulfone Colloids: Effect on Ultrafiltration Fouling. *J. Memb. Sci.* **2006**, *281* (1–2), 472–479. https://doi.org/10.1016/j.memsci.2006.04.030.
(157) van Loosdrecht, M. C. M.; Norde, W.; Lyklema, J.; Zehnder, A. J. B. Hydrophobic and Electrostatic Parameters in Bacterial Adhesion. *Aquat. Sci.* **1990**, *52* (1), 103–114. https://doi.org/10.1007/BF00878244.
(158) Müller, D. J.; Dufrêne, Y. F. Atomic Force Microscopy as a Multifunctional Molecular Toolbox in Nanobiotechnology. *Nat. Nanotechnol.* **2008**, *3* (5), 261–269. https://doi.org/10.1038/nnano.2008.100.
(159) Israelachvili, J. N. *Intermolecular and Surface Forces with Applications to Colloidal and Biological Systems*; Academic Press: Orlando, 1985.
(160) Oberhauser, A. F.; Marszalek, P. E.; Erickson, H. P.; Fernandez, J. M. The Molecular Elasticity of the Extracellular Matrix Protein Tenascin. *Nature* **1998**, *393* (6681), 181–185. https://doi.org/10.1038/30270.
(161) Rief, M.; Gautel, M.; Oesterhelt, F.; Fernandez, J. M.; Gaub, H. E. Reversible Unfolding of Individual Titin Immunoglobulin Domains by AFM. *Science (80-.).* **1997**, *276* (5315), 1109–1112. https://doi.org/10.1126/science.276.5315.1109.
(162) Stirnemann, G.; Giganti, D.; Fernandez, J. M.; Berne, B. J. Elasticity, Structure, and Relaxation of Extended Proteins under Force. *Proc. Natl. Acad. Sci.* **2013**, *110* (10), 3847–3852. https://doi.org/10.1073/pnas.1300596110.
(163) Abu-Lail, N. I.; Camesano, T. A. Elasticity of Pseudomonas Putida KT2442 Surface Polymers Probed with Single-Molecule Force Microscopy. *Langmuir* **2002**, *18* (10), 4071–4081. https://doi.org/10.1021/la015695b.
(164) Flory, P. J. Statistical Mechanics of Chain Molecules. In *Statistical Mechanics of*

Chain Molecules; Flory, P. J., Ed.; Hanser Publishers, 1989; pp 401–403.
(165) Touhami, A.; Alexander, M.; Kurylowicz, M.; Gram, C.; Corredig, M.; Dutcher, J. R. Probing Protein Conformations at the Oil Droplet–Water Interface Using Single-Molecule Force Spectroscopy. *Soft Matter* **2011**, *7* (21), 10274. https://doi.org/10.1039/c1sm06284k.
(166) Saleh, O. A. Perspective: Single Polymer Mechanics across the Force Regimes. *J. Chem. Phys.* **2015**, *142* (19), 194902. https://doi.org/10.1063/1.4921348.
(167) Walther, K. A.; Grater, F.; Dougan, L.; Badilla, C. L.; Berne, B. J.; Fernandez, J. M. Signatures of Hydrophobic Collapse in Extended Proteins Captured with Force Spectroscopy. *Proc. Natl. Acad. Sci.* **2007**, *104* (19), 7916–7921. https://doi.org/10.1073/pnas.0702179104.
(168) Dee, K. C.; Puleo, D. A.; Bizios, R. *An Introduction to Tissue-Biomaterial Interactions*, First.; John Wiley & Sons: Hoboken, NJ, 2002.
(169) Koehler, J. A.; Ulbricht, M.; Belfort, G. Intermolecular Forces between a Protein and a Hydrophilic Modified Polysulfone Film with Relevance to Filtration. *Langmuir* **2000**, *16* (26), 10419–10427. https://doi.org/10.1021/la000593r.
(170) Ptitsyn, O. B. Molten Globule and Protein Folding. *Adv. Protein Chem.* **1995**, *47*, 83–229. https://doi.org/10.1016/S0065-3233(08)60546-X.
(171) Müller, D. J.; Helenius, J.; Alsteens, D.; Dufrêne, Y. F. Force Probing Surfaces of Living Cells to Molecular Resolution. *Nat. Chem. Biol.* **2009**, *5* (6), 383–390. https://doi.org/10.1038/nchembio.181.
(172) Li, H.; Linke, W. A.; Oberhauser, A. F.; Carrion-Vazquez, M.; Kerkvliet, J. G.; Lu, H.; Marszalek, P. E.; Fernandez, J. M. Reverse Engineering of the Giant Muscle Protein Titin. *Nature* **2002**, *418* (6901), 998–1002. https://doi.org/10.1038/nature00938.
(173) Xu, L.-C.; Siedlecki, C. A. Effects of Surface Wettability and Contact Time on Protein Adhesion to Biomaterial Surfaces. *Biomaterials* **2007**, *28* (22), 3273–3283. https://doi.org/10.1016/j.biomaterials.2007.03.032.
(174) Kim, J.; Somorjai, G. A. Molecular Packing of Lysozyme, Fibrinogen, and Bovine Serum Albumin on Hydrophilic and Hydrophobic Surfaces Studied by Infrared−Visible Sum Frequency Generation and Fluorescence Microscopy. *J. Am. Chem. Soc.* **2003**, *125* (10), 3150–3158. https://doi.org/10.1021/ja028987n.
(175) Oberhauser, A. F.; Badilla-Fernandez, C.; Carrion-Vazquez, M.; Fernandez, J. M. The Mechanical Hierarchies of Fibronectin Observed with Single-Molecule AFM. *J. Mol. Biol.* **2002**, *319* (2), 433–447. https://doi.org/10.1016/S0022-2836(02)00306-6.
(176) Filloux, A.; de Bentzmann, S.; Aurouze, M.; Lazdunski, A.; Vallet, I.; de Bentzmann, S. Aurouze, M.; Lazdunski, A.; Vallet, I. Fimbrial Genes in Pseudomonas Aeruginosa and Pseudomonas Putida. *Pseudomonas, V1*; Ramos, J. L., Ed.; Kluwer Academic/Plenum Publishers, 2004; pp 721–748.
(177) Whitechurch, C. B. Biogenesis and Function of Type IV Pili in Pseudomonas Species. *Pseudomonas, V4*; Ramos, J.-L., Levesque, R. C., Eds.; Springer Netherlands, 2006; pp 139–188.
(178) Ye, G.; Lee, J.; Perreault, F.; Elimelech, M. Controlled Architecture of Dual-Functional Block Copolymer Brushes on Thin-Film Composite Membranes for Integrated “Defending” and “Attacking” Strategies against Biofouling. *ACS Appl.*

Mater. Interfaces **2015**, *7* (41), 23069–23079. https://doi.org/10.1021/acsami.5b06647.
(179) Novoselov, K. S.; Geim, A. K.; Morozov, S. V.; Jiang, D.; Zhang, Y.; Dubonos, S. V.; Grigorieva, I. V.; Firsov, A. A. Electric Field in Atomically Thin Carbon Films. *Science (80-.).* **2004**. https://doi.org/10.1126/science.1102896.
(180) Alvarez, P. J. J.; Chan, C. K.; Elimelech, M.; Halas, N. J.; Villagrán, D. Emerging Opportunities for Nanotechnology to Enhance Water Security. *Nat. Nanotechnol.* **2018**, *13* (8), 634–641. https://doi.org/10.1038/s41565-018-0203-2.
(181) Zhu, Y.; Murali, S.; Cai, W.; Li, X.; Suk, J. W.; Potts, J. R.; Ruoff, R. S. Graphene and Graphene Oxide: Synthesis, Properties, and Applications. *Adv. Mater.* **2010**, *22* (35), 3906–3924. https://doi.org/10.1002/adma.201001068.
(182) Joshi, R. K.; Carbone, P.; Wang, F. C.; Kravets, V. G.; Su, Y.; Grigorieva, I. V.; Wu, H. A.; Geim, A. K.; Nair, R. R. Precise and Ultrafast Molecular Sieving through Graphene Oxide Membranes. *Science (80-.).* **2014**, *343* (6172), 752–754. https://doi.org/10.1126/science.1245711.
(183) O'Hern, S. C.; Boutilier, M. S. H.; Idrobo, J. C.; Song, Y.; Kong, J.; Laoui, T.; Atieh, M.; Karnik, R. Selective Ionic Transport through Tunable Subnanometer Pores in Single-Layer Graphene Membranes. *Nano Lett.* **2014**, *14* (3), 1234–1241. https://doi.org/10.1021/nl404118f.
(184) Hu, M.; Mi, B. Enabling Graphene Oxide Nanosheets as Water Separation Membranes. *Environ. Sci. Technol.* **2013**, *47* (8), 3715–3723. https://doi.org/10.1021/es400571g.
(185) Yousefi, N.; Lu, X.; Elimelech, M.; Tufenkji, N. Environmental Performance of Graphene-Based 3D Macrostructures. *Nat. Nanotechnol.* **2019**, *14* (2), 107–119. https://doi.org/10.1038/s41565-018-0325-6.
(186) Yang, Y.; Zhao, R.; Zhang, T.; Zhao, K.; Xiao, P.; Ma, Y.; Ajayan, P. M.; Shi, G.; Chen, Y. Graphene-Based Standalone Solar Energy Converter for Water Desalination and Purification. *ACS Nano* **2018**, *12* (1), 829–835. https://doi.org/10.1021/acsnano.7b08196.
(187) Perreault, F.; Fonseca De Faria, A.; Elimelech, M. Environmental Applications of Graphene-Based Nanomaterials. *Chem. Soc. Rev.* **2015**, *44* (16), 5861–5896. https://doi.org/10.1039/c5cs00021a.
(188) Sanchez, V. C.; Jachak, A.; Hurt, R. H.; Kane, A. B. Biological Interactions of Graphene-Family Nanomaterials: An Interdisciplinary Review. *Chem. Res. Toxicol.* **2012**, *25* (1), 15–34. https://doi.org/10.1021/tx200339h.
(189) Chen, J.; Peng, H.; Wang, X.; Shao, F.; Yuan, Z.; Han, H. Graphene Oxide Exhibits Broad-Spectrum Antimicrobial Activity against Bacterial Phytopathogens and Fungal Conidia by Intertwining and Membrane Perturbation. *Nanoscale* **2014**, *6* (3), 1879–1889. https://doi.org/10.1039/C3NR04941H.
(190) Hu, W.; Peng, C.; Luo, W.; Lv, M.; Li, X.; Li, D.; Huang, Q.; Fan, C. Graphene-Based Antibacterial Paper. *ACS Nano* **2010**, *4* (7), 4317–4323. https://doi.org/10.1021/nn101097v.
(191) Perreault, F.; de Faria, A. F.; Nejati, S.; Elimelech, M. Antimicrobial Properties of Graphene Oxide Nanosheets: Why Size Matters. *ACS Nano* **2015**, *9* (7), 7226–7236. https://doi.org/10.1021/acsnano.5b02067.
(192) Gurunathan, S.; Han, J. W.; Dayem, A. A.; Eppakayala, V.; Kim, J. H. Oxidative

Stress-Mediated Antibacterial Activity of Graphene Oxide and Reduced Graphene Oxide in Pseudomonas Aeruginosa. *Int. J. Nanomedicine* **2012**, *7*, 5901–5914. https://doi.org/10.2147/IJN.S37397.

(193) Chae, H. R.; Lee, J.; Lee, C. H.; Kim, I. C.; Park, P. K. Graphene Oxide-Embedded Thin-Film Composite Reverse Osmosis Membrane with High Flux, Anti-Biofouling, and Chlorine Resistance. *J. Memb. Sci.* **2015**, *483*, 128–135. https://doi.org/10.1016/j.memsci.2015.02.045.

(194) Ali, M. E. A.; Wang, L.; Wang, X.; Feng, X. Thin Film Composite Membranes Embedded with Graphene Oxide for Water Desalination. *Desalination* **2016**, *386*, 67–76. https://doi.org/10.1016/j.desal.2016.02.034.

(195) Lu, X.; Feng, X.; Zhang, X.; Chukwu, M. N.; Osuji, C. O.; Elimelech, M. Fabrication of a Desalination Membrane with Enhanced Microbial Resistance through Vertical Alignment of Graphene Oxide. **2018**. https://doi.org/10.1021/acs.estlett.8b00364.

(196) Perreault, F.; Tousley, M. E.; Elimelech, M. Thin-Film Composite Polyamide Membranes Functionalized with Biocidal Graphene Oxide Nanosheets. *Environ. Sci. Technol. Lett.* **2013**.

(197) Perreault, F.; Jaramillo, H.; Xie, M.; Ude, M.; Nghiem, L. D.; Elimelech, M. Biofouling Mitigation in Forward Osmosis Using Graphene Oxide Functionalized Thin-Film Composite Membranes. *Environ. Sci. Technol.* **2016**, *50* (11), 5840–5848. https://doi.org/10.1021/acs.est.5b06364.

(198) Dufrene, Y. F. Sticky Microbes: Forces in Microbial Cell Adhesion. *Trends Microbiol.* **2015**, *23* (6), 376–382. https://doi.org/10.1016/j.tim.2015.01.011.

(199) Xue, J.; BinAhmed, S.; Wang, Z.; Karp, N. G.; Stottrup, B. L.; Romero-Vargas Castrillón, S. Bacterial Adhesion to Graphene Oxide (GO)-Functionalized Interfaces Is Determined by Hydrophobicity and GO Sheet Spatial Orientation. *Environ. Sci. Technol. Lett.* **2018**, *5* (1), 14–19. https://doi.org/10.1021/acs.estlett.7b00509.

(200) Rice, D.; Barrios, A. C.; Xiao, Z.; Bogler, A.; Bar-Zeev, E.; Perreault, F. Development of Anti-Biofouling Feed Spacers to Improve Performance of Reverse Osmosis Modules. *Water Res.* **2018**, *145*, 599–607. https://doi.org/10.1016/j.watres.2018.08.068.

(201) Wang, H.; Brown, H. R. Self-Initiated Photopolymerization and Photografting of Acrylic Monomers. *Macromol. Rapid Commun.* **2004**. https://doi.org/10.1002/marc.200400010.

(202) Deng, J.; Wang, L.; Liu, L.; Yang, W. Developments and New Applications of UV-Induced Surface Graft Polymerizations. *Prog. Polym. Sci.* **2009**. https://doi.org/10.1016/j.progpolymsci.2008.06.002.

(203) Van der Bruggen, B. Chemical Modification of Polyethersulfone Nanofiltration Membranes: A Review. *J. Appl. Polym. Sci.* **2009**, *114* (1), 630–642. https://doi.org/10.1002/app.30578.

(204) Igbinigun, E.; Fennell, Y.; Malaisamy, R.; Jones, K. L.; Morris, V. Graphene Oxide Functionalized Polyethersulfone Membrane to Reduce Organic Fouling. *J. Memb. Sci.* **2016**. https://doi.org/10.1016/j.memsci.2016.05.024.

(205) Homayoonfal, M.; Akbari, A.; Mehrnia, M. R. Preparation of Polysulfone Nanofiltration Membranes by UV-Assisted Grafting Polymerization for Water

Softening. *Desalination* **2010**. https://doi.org/10.1016/j.desal.2010.06.062.
(206) Li, D.; Müller, M. B.; Gilje, S.; Kaner, R. B.; Wallace, G. G. Processable Aqueous Dispersions of Graphene Nanosheets. *Nat. Nanotechnol.* **2008**, *3* (2), 101–105. https://doi.org/10.1038/nnano.2007.451.
(207) Kudin, K. N.; Ozbas, B.; Schniepp, H. C.; Prud'homme, R. K.; Aksay, I. A.; Car, R. Raman Spectra of Graphite Oxide and Functionalized Graphene Sheets. *Nano Lett.* **2008**, *8* (1), 36–41. https://doi.org/10.1021/nl071822y.
(208) Grabarek, Z.; Gergely, J. Zero-Length Crosslinking Procedure with the Use of Active Esters. *Anal. Biochem.* **1990**, *185* (1), 131–135. https://doi.org/10.1016/0003-2697(90)90267-D.
(209) Walker, S. L.; Bhattacharjee, S.; Hoek, E. M. V.; Elimelech, M. A Novel Asymmetric Clamping Cell for Measuring Streaming Potential of Flat Surfaces. *Langmuir* **2002**, *18* (6), 2193–2198. https://doi.org/10.1021/la011284j.
(210) Ma, H.; Davis, R. H.; Bowman, C. N. Novel Sequential Photoinduced Living Graft Polymerization. *Macromolecules* **2000**, *33* (2), 331–335. https://doi.org/10.1021/ma990821s.
(211) Klaysom, C.; Ladewig, B. P.; Lu, G. Q. M.; Wang, L. Preparation and Characterization of Sulfonated Polyethersulfone for Cation-Exchange Membranes. *J. Memb. Sci.* **2011**, *368* (1–2), 48–53. https://doi.org/10.1016/j.memsci.2010.11.006.
(212) Pretsch, E.; Bühlmann, P.; Affolter, C. *Structure Determination of Organic Compounds*, Third Ed.; Springer, 2000. https://doi.org/10.1111/j.1471-0528.2007.01499.x.
(213) Wang, L.; Song, X.; Wang, T.; Wang, S.; Wang, Z.; Gao, C. Fabrication and Characterization of Polyethersulfone/Carbon Nanotubes (PES/CNTs) Based Mixed Matrix Membranes (MMMs) for Nanofiltration Application. *Appl. Surf. Sci.* **2015**, *330*, 118–125. https://doi.org/10.1016/j.apsusc.2014.12.183.
(214) Evans, P. J.; Bird, M. R.; Pihlajamäki, A.; Nyström, M. The Influence of Hydrophobicity, Roughness and Charge upon Ultrafiltration Membranes for Black Tea Liquor Clarification. *J. Memb. Sci.* **2008**, *313* (1–2), 250–262. https://doi.org/10.1016/j.memsci.2008.01.010.
(215) Weis, A.; Bird, M. R.; Nyström, M.; Wright, C. The Influence of Morphology, Hydrophobicity and Charge upon the Long-Term Performance of Ultrafiltration Membranes Fouled with Spent Sulphite Liquor. *Desalination* **2005**, *175* (1 SPEC. ISS.), 73–85. https://doi.org/10.1016/j.desal.2004.09.024.
(216) Susanto, H.; Ulbricht, M. Characteristics, Performance and Stability of Polyethersulfone Ultrafiltration Membranes Prepared by Phase Separation Method Using Different Macromolecular Additives. *J. Memb. Sci.* **2009**, *327* (1–2), 125–135. https://doi.org/10.1016/j.memsci.2008.11.025.
(217) Park, N.; Kwon, B.; Kim, I. S.; Cho, J. Biofouling Potential of Various NF Membranes with Respect to Bacteria and Their Soluble Microbial Products (SMP): Characterizations, Flux Decline, and Transport Parameters. *J. Memb. Sci.* **2005**, *258* (1–2), 43–54. https://doi.org/10.1016/j.memsci.2005.02.025.
(218) Pasmore, M.; Todd, P.; Smith, S.; Baker, D.; Silverstein, J. A.; Coons, D.; Bowman, C. N. Effects of Ultrafiltration Membrane Surface Properties on Pseudomonas Aeruginosa Biofilm Initiation for the Purpose of Reducing Biofouling. *J. Memb. Sci.*

2001, *194* (1), 15–32. https://doi.org/10.1016/S0376-7388(01)00468-9.
(219) Vrijenhoek, E. M.; Hong, S.; Elimelech, M. Influence of Membrane Surface Properties on Initial Rate of Colloidal Fouling of Reverse Osmosis and Nanofiltration Membranes. *J. Memb. Sci.* **2001**, *188* (1), 115–128. https://doi.org/10.1016/S0376-7388(01)00376-3.
(220) Elimelech, M.; Zhu, X.; Childress, A. E.; Hong, S. Role of Membrane Surface Morphology in Colloidal Fouling of Cellulose Acetate and Composite Aromatic Polyamide Reverse Osmosis Membranes. *J. Memb. Sci.* **1997**, *127* (1), 101–109. https://doi.org/10.1016/S0376-7388(96)00351-1.
(221) Wu, T.; Gong, P.; Szleifer, I.; Vlček, P.; Šubr, V.; Genzer, J. Behavior of Surface-Anchored Poly(Acrylic Acid) Brushes with Grafting Density Gradients on Solid Substrates: 1. Experiment. *Macromolecules* **2007**, *40* (24), 8756–8764. https://doi.org/10.1021/ma0710176.
(222) Ronen, A.; Duan, W.; Wheeldon, I.; Walker, S.; Jassby, D. Microbial Attachment Inhibition through Low-Voltage Electrochemical Reactions on Electrically Conducting Membranes. *Environ. Sci. Technol.* **2015**, *49* (21), 12741–12750. https://doi.org/10.1021/acs.est.5b01281.
(223) Dasgupta, N.; Arora, S. K.; Ramphal, R. The Flagellar System of Pseudomonas Aeruginosa BT - Pseudomonas: Volume 1 Genomics, Life Style and Molecular Architecture; Ramos, J.-L., Ed.; Springer US: Boston, MA, 2004; pp 675–698. https://doi.org/10.1007/978-1-4419-9086-0_22.
(224) Pasche, S.; Textor, M.; Meagher, L.; Spencer, N. D.; Griesser, H. J. Relationship between Interfacial Forces Measured by Colloid-Probe Atomic Force Microscopy and Protein Resistance of Poly(Ethylene Glycol)-Grafted Poly(L-Lysine) Adlayers on Niobia Surfaces. *Langmuir* **2005**, *21* (14), 6508–6520. https://doi.org/10.1021/la050386x.
(225) Gon, S.; Kumar, K. N.; Nüsslein, K.; Santore, M. M. How Bacteria Adhere to Brushy PEG Surfaces: Clinging to Flaws and Compressing the Brush. *Macromolecules* **2012**, *45* (20), 8373–8381. https://doi.org/10.1021/ma300981r.
(226) Erickson, K.; Erni, R.; Lee, Z.; Alem, N.; Gannett, W.; Zettl, A. Determination of the Local Chemical Structure of Graphene Oxide and Reduced Graphene Oxide. *Adv. Mater.* **2010**, *22* (40), 4467–4472. https://doi.org/10.1002/adma.201000732.
(227) Cote, L. J.; Kim, J.; Tung, V. C.; Luo, J.; Kim, F.; Huang, J. Graphene Oxide as Surfactant Sheets. *Pure Appl. Chem* **2010**, *83* (1), 95–110. https://doi.org/10.1351/PAC-CON-10-10-25.
(228) Kim, J.; Cote, L. J.; Kim, F.; Yuan, W.; Shull, K. R.; Huang, J. Graphene Oxide Sheets at Interfaces. *J. Am. Chem. Soc.* **2010**, *132* (23), 8180–8186. https://doi.org/10.1021/ja102777p.
(229) Liu, Z.; Robinson, J. T.; Sun, X.; Dai, H. PEGylated Nanographene Oxide for Delivery of Water-Insoluble Cancer Drugs. *J. Am. Chem. Soc.* **2008**, *130* (33), 10876–10877. https://doi.org/10.1021/ja803688x.
(230) Rief, M.; Gautel, M.; Oesterhelt, F.; Fernandez, J. M.; Gaub, H. E. Reversible Unfolding of Individual Titin Immunoglobulin Domains by AFM. *Science (80-.).* **1997**, *276* (5315), 1109–1112. https://doi.org/10.1126/science.276.5315.1109.
(231) Li, H.; Liu, B.; Zhang, X.; Gao, C.; Shen, J.; Zou, G. Single-Molecule Force Spectroscopy on Poly(Acrylic Acid) by AFM. *Langmuir* **1999**, *15* (6), 2120–2124.

https://doi.org/10.1021/la9800304.
(232) Carrion-Vazquez, M.; Oberhauser, A. F.; Fowler, S. B.; Marszalek, P. E.; Broedel, S. E.; Clarke, J.; Fernandez, J. M. Mechanical and Chemical Unfolding of a Single Protein: A Comparison. *Proc. Natl. Acad. Sci. U. S. A.* **1999**, *96* (7), 3694–3699.
(233) Filloux, A.; de Bentzmann, S. Aurouze, M.; Lazdunski, A.; Vallet, I. Fimbrial Genes in Pseudomonas Aeruginosa and Pseudomonas Putida. In *Pseudomonas*; Ramos, J. L., Ed.; 2004; pp 721–748.
(234) Akhavan, O.; Ghaderi, E. Toxicity of Graphene and Graphene Oxide Nanowalls against Bacteria. *ACS Nano* **2010**, *4* (10), 5731–5736. https://doi.org/10.1021/nn101390x.
(235) Oki, T.; Kanae, S. Global Hydrological Cycles and World Water Resources. *Science (80-.).* **2006**, *313* (5790), 1068–1072. https://doi.org/10.1126/science.1128845.
(236) Gullinkala, T.; Escobar, I. C. Membranes for Water Treatment Applications – An Overview. In *ACS Symposium Series*; 2011; pp 155–170. https://doi.org/10.1021/bk-2011-1078.ch010.
(237) Doederer, K.; Farré, M. J.; Pidou, M.; Weinberg, H. S.; Gernjak, W. Rejection of Disinfection By-Products by RO and NF Membranes: Influence of Solute Properties and Operational Parameters. *J. Memb. Sci.* **2014**, *467*, 195–205. https://doi.org/10.1016/j.memsci.2014.05.029.
(238) Wu, J.; Contreras, A. E.; Li, Q. Studying the Impact of RO Membrane Surface Functional Groups on Alginate Fouling in Seawater Desalination. *J. Memb. Sci.* **2014**, *458*, 120–127. https://doi.org/10.1016/j.memsci.2014.01.056.
(239) Varin, K. J.; Lin, N. H.; Cohen, Y. Biofouling and Cleaning Effectiveness of Surface Nanostructured Reverse Osmosis Membranes. *J. Memb. Sci.* **2013**, *446*, 472–481. https://doi.org/10.1016/j.memsci.2013.06.064.
(240) Xu, P.; Drewes, J. E.; Kim, T.-U.; Bellona, C.; Amy, G. Effect of Membrane Fouling on Transport of Organic Contaminants in NF/RO Membrane Applications. *J. Memb. Sci.* **2006**, *279* (1–2), 165–175. https://doi.org/10.1016/j.memsci.2005.12.001.
(241) Zou, L.; Vidalis, I.; Steele, D.; Michelmore, A.; Low, S. P.; Verberk, J. Q. J. C. Surface Hydrophilic Modification of RO Membranes by Plasma Polymerization for Low Organic Fouling. *J. Memb. Sci.* **2011**, *369* (1–2), 420–428. https://doi.org/10.1016/j.memsci.2010.12.023.
(242) Ghanbari, M.; Emadzadeh, D.; Lau, W. J.; Matsuura, T.; Ismail, A. F. Synthesis and Characterization of Novel Thin Film Nanocomposite Reverse Osmosis Membranes with Improved Organic Fouling Properties for Water Desalination. *RSC Adv.* **2015**, *5* (27), 21268–21276. https://doi.org/10.1039/c4ra16177g.
(243) Katsoufidou, K.; Yiantsios, S. G.; Karabelas, A. J. An Experimental Study of UF Membrane Fouling by Humic Acid and Sodium Alginate Solutions: The Effect of Backwashing on Flux Recovery. *Desalination* **2008**, *220* (1–3), 214–227. https://doi.org/10.1016/j.desal.2007.02.038.
(244) Jones, K. L.; O'Melia, C. R. Ultrafiltration of Protein and Humic Substances: Effect of Solution Chemistry on Fouling and Flux Decline. *J. Memb. Sci.* **2001**, *193* (2), 163–173. https://doi.org/10.1016/S0376-7388(01)00492-6.
(245) Baek, Y.; Yu, J.; Kim, S.-H.; Lee, S.; Yoon, J. Effect of Surface Properties of Reverse Osmosis Membranes on Biofouling Occurrence under Filtration Conditions. *J. Memb. Sci.* **2011**, *382* (1–2), 91–99.

https://doi.org/10.1016/j.memsci.2011.07.049.
(246) Suwarno, S. R.; Hanada, S.; Chong, T. H.; Goto, S.; Henmi, M.; Fane, A. G. The Effect of Different Surface Conditioning Layers on Bacterial Adhesion on Reverse Osmosis Membranes. *Desalination* **2016**, *387*, 1–13. https://doi.org/10.1016/j.desal.2016.02.029.
(247) Kim, S.; Lee, S.; Lee, E.; Sarper, S.; Kim, C. H.; Cho, J. Enhanced or Reduced Concentration Polarization by Membrane Fouling in Seawater Reverse Osmosis (SWRO) Processes. *Desalination* **2009**, *247* (1–3), 162–168. https://doi.org/10.1016/j.desal.2008.12.021.
(248) John, V. C.; Coles, S. L.; Abozed, A. I. Seasonal Cycles of Temperature, Salinity and Water Masses of the Western Arabian Gulf. *Oceanol. Acta* **1990**, *13* (3), 273–282.
(249) Schaep, J.; Van Der Bruggen, B.; Uytterhoeven, S.; Croux, R.; Vandecasteele, C.; Wilms, D.; Van Houtte, E.; Vanlerberghe, F. Remvoal of Hardness from Groundwater by Nanofiltration. *Desalination* **1998**, *119* (1–3), 295–301. https://doi.org/10.1016/S0011-9164(98)00172-6.
(250) Francis, M. J. J.; Pashley, R. M. M. The Effects of Feed Water Temperature and Dissolved Gases on Permeate Flow Rate and Permeate Conductivity in a Pilot Scale Reverse Osmosis Desalination Unit. *Desalin. Water Treat.* **2011**, *36* (1–3), 363–373. https://doi.org/10.5004/dwt.2011.2511.
(251) Al-Mutaz, I. S.; Al-Ghunaimi, M. A. Performance of Reverse Osmosis Units at High Temperatures. In *IDA World Congress on Desalination and Water Reuse*; 2001.
(252) Wilf, M.; Bartels, C. Optimization of Seawater RO Systems Design. *Desalination* **2005**, *173* (1), 1–12. https://doi.org/10.1016/j.desal.2004.06.206.
(253) Ormanci-Acar, T.; Celebi, F.; Keskin, B.; Mutlu-Salmanlı, O.; Agtas, M.; Turken, T.; Tufani, A.; Imer, D. Y.; Ince, G. O.; Demir, T. U.; Menceloglu, Y. Z.; Unal, S.; Koyuncu, I. Fabrication and Characterization of Temperature and PH Resistant Thin Film Nanocomposite Membranes Embedded with Halloysite Nanotubes for Dye Rejection. *Desalination* **2018**, *429*, 20–32. https://doi.org/10.1016/j.desal.2017.12.005.
(254) Sharma, R. R.; Chellam, S. Temperature Effects on the Morphology of Porous Thin Film Composite Nanofiltration Membranes. *Environ. Sci. Technol.* **2005**, *39* (13), 5022–5030. https://doi.org/10.1021/es0501363.
(255) Listiarini, K.; Chun, W.; Sun, D. D.; Leckie, J. O. Fouling Mechanism and Resistance Analyses of Systems Containing Sodium Alginate, Calcium, Alum and Their Combination in Dead-End Fouling of Nanofiltration Membranes. *J. Memb. Sci.* **2009**, *344* (1–2), 244–251. https://doi.org/10.1016/j.memsci.2009.08.010.
(256) Boyd, A.; Chakrabarty, A. M. Pseudomonas Aeruginosa Biofilms: Role of the Alginate Exopolysaccharide. *J. Ind. Microbiol.* **1995**, *15* (3), 162–168.
(257) Bellona, C.; Heil, D.; Yu, C.; Fu, P.; Drewes, J. E. The Pros and Cons of Using Nanofiltration in Lieu of Reverse Osmosis for Indirect Potable Reuse Applications. *Sep. Purif. Technol.* **2012**, *85*, 69–76. https://doi.org/10.1016/j.seppur.2011.09.046.
(258) Surawanvijit, S.; Rahardianto, A.; Cohen, Y. An Integrated Approach for Characterization of Polyamide Reverse Osmosis Membrane Degradation Due to Exposure to Free Chlorine. *J. Memb. Sci.* **2016**, *510*, 164–173. https://doi.org/10.1016/j.memsci.2016.02.044.

(259) Ci, S. X.; Huynh, T. H.; Louie, L. W.; Yang, A.; Beals, B. J.; Ron, N.; Tsang, W.-G.; Soon-Shiong, P.; Desai, N. P. Molecular Mass Distribution of Sodium Alginate by High-Performance Size-Exclusion Chromatography. *J. Chromatogr. A* **1999**, *864* (2), 199–210. https://doi.org/10.1016/S0021-9673(99)01029-8.
(260) Ye, Y.; Le Clech, P.; Chen, V.; Fane, A. G.; Jefferson, B. Fouling Mechanisms of Alginate Solutions as Model Extracellular Polymeric Substances. *Desalination* **2005**, *175* (1), 7–20. https://doi.org/10.1016/j.desal.2004.09.019.
(261) Matin, A.; Shafi, H.; Wang, M.; Khan, Z.; Gleason, K.; Rahman, F. Reverse Osmosis Membranes Surface-Modified Using an Initiated Chemical Vapor Deposition Technique Show Resistance to Alginate Fouling under Cross-Flow Conditions: Filtration & Subsequent Characterization. *Desalination* **2016**, *379*, 108–117. https://doi.org/10.1016/j.desal.2015.11.003.
(262) Katsoufidou, K.; Yiantsios, S. G.; Karabelas, A. J. Experimental Study of Ultrafiltration Membrane Fouling by Sodium Alginate and Flux Recovery by Backwashing. *J. Memb. Sci.* **2007**, *300* (1–2), 137–146. https://doi.org/10.1016/j.memsci.2007.05.017.
(263) Lu, X.; Romero-Vargas Castrillón, S.; Shaffer, D. L.; Ma, J.; Elimelech, M. In Situ Surface Chemical Modification of Thin-Film Composite Forward Osmosis Membranes for Enhanced Organic Fouling Resistance. *Environ. Sci. Technol.* **2013**, *47* (21), 12219–12228. https://doi.org/10.1021/es403179m.
(264) Ang, W. S.; Yip, N. Y.; Tiraferri, A.; Elimelech, M. Chemical Cleaning of RO Membranes Fouled by Wastewater Effluent: Achieving Higher Efficiency with Dual-Step Cleaning. *J. Memb. Sci.* **2011**, *382* (1–2), 100–106. https://doi.org/10.1016/j.memsci.2011.07.047.
(265) Tiraferri, A.; Kang, Y.; Giannelis, E. P.; Elimelech, M. Superhydrophilic Thin-Film Composite Forward Osmosis Membranes for Organic Fouling Control: Fouling Behavior and Antifouling Mechanisms. *Environ. Sci. Technol.* **2012**, *46* (20), 11135–11144. https://doi.org/10.1021/es3028617.
(266) Bartels, C. R.; Wilf, M.; Andes, K.; Iong, J. Design Considerations for Wastewater Treatment by Reverse Osmosis. *Water Sci. Technol.* **2005**, *51* (6–7), 473–482. https://doi.org/10.2166/wst.2005.0670.
(267) Khan, M. T.; Busch, M.; Molina, V. G.; Emwas, A.-H.; Aubry, C.; Croue, J.-P. How Different Is the Composition of the Fouling Layer of Wastewater Reuse and Seawater Desalination RO Membranes? *Water Res.* **2014**, *59*, 271–282. https://doi.org/10.1016/j.watres.2014.04.020.
(268) Kim, H.-C.; Dempsey, B. A. Comparison of Two Fractionation Strategies for Characterization of Wastewater Effluent Organic Matter and Diagnosis of Membrane Fouling. *Water Res.* **2012**, *46* (11), 3714–3722. https://doi.org/https://doi.org/10.1016/j.watres.2012.04.025.
(269) Li, Q.; Elimelech, M. Organic Fouling and Chemical Cleaning of Nanofiltration Membranes: Measurements and Mechanisms. *Environ. Sci. Technol.* **2004**, *38* (17), 4683–4693. https://doi.org/10.1021/es0354162.
(270) Behrens, S. H.; Christl, D. I.; Emmerzael, R.; Schurtenberger, P.; Borkovec, M. Charging and Aggregation Properties of Carboxyl Latex Particles: Experiments versus DLVO Theory. *Langmuir* **2000**, *16* (6), 2566–2575. https://doi.org/10.1021/la991154z.

(271) Zhang, X. H.; Quinn, A.; Ducker, W. A. Nanobubbles at the Interface between Water and a Hydrophobic Solid. *Langmuir* **2008**, *24* (9), 4756–4764. https://doi.org/10.1021/la703475q.
(272) Lo, Y.-S.; Simons, J.; Beebe, T. P. Temperature Dependence of the Biotin-Avidin Bond-Rupture Force Studied by Atomic Force Microscopy. *J. Phys. Chem. B* **2002**, *106* (38), 9847–9852. https://doi.org/10.1021/jp020863+.
(273) Heinz, W. F.; Hoh, J. H. Getting Physical with Your Chemistry: Mechanically Investigating Local Structure and Properties of Surfaces with the Atomic Force Microscope. *J. Chem. Educ.* **2005**, *82* (5), 695–703. https://doi.org/10.1021/ed082p695.
(274) Heinz, W. F.; Hoh, J. H. Spatially Resolved Force Spectroscopy of Biological Surfaces Using the Atomic Force Microscope. *Trends Biotechnol.* **1999**, *17* (4), 143–150. https://doi.org/10.1016/S0167-7799(99)01304-9.
(275) Erts, D.; Lõhmus, A.; Lõhmus, R.; Olin, H.; Pokropivny, A. V; Ryen, L.; Svensson, K. Force Interactions and Adhesion of Gold Contacts Using a Combined Atomic Force Microscope and Transmission Electron Microscope. *Appl. Surf. Sci.* **2002**, *188* (3–4), 460–466. https://doi.org/https://doi.org/10.1016/S0169-4332(01)00933-3.
(276) Butt, H.-J.; Cappella, B.; Kappl, M. Force Measurements with the Atomic Force Microscope: Technique, Interpretation and Applications. *Surf. Sci. Rep.* **2005**, *59* (1), 1–152. https://doi.org/https://doi.org/10.1016/j.surfrep.2005.08.003.
(277) Ozaydin-Ince, G.; Matin, A.; Khan, Z.; Zaidi, S. M. M. J.; Gleason, K. K. Surface Modification of Reverse Osmosis Desalination Membranes by Thin-Film Coatings Deposited by Initiated Chemical Vapor Deposition. *Thin Solid Films* **2013**, *539*, 181–187. https://doi.org/10.1016/j.tsf.2013.04.133.
(278) Li, Q.; Pan, X.; Qu, Z.; Zhao, X.; Jin, Y.; Dai, H.; Yang, B.; Wang, X. Understanding the Dependence of Contact Angles of Commercially RO Membranes on External Conditions and Surface Features. *Desalination* **2013**, *309*, 38–45. https://doi.org/10.1016/j.desal.2012.09.007.
(279) Akin, O.; Temelli, F. Probing the Hydrophobicity of Commercial Reverse Osmosis Membranes Produced by Interfacial Polymerization Using Contact Angle, XPS, FTIR, FE-SEM and AFM. *Desalination* **2011**, *278* (1–3), 387–396. https://doi.org/10.1016/j.desal.2011.05.053.
(280) Andrade, J. D.; Smith, L. M.; Gregonis, D. E. The Contact Angle and Interface Energetics. In *Surface and Interfacial Aspects of Biomedical Polymers*; Springer US: Boston, MA, 1985; Vol. 1, pp 249–292. https://doi.org/10.1007/978-1-4684-8610-0_7.
(281) Diaz, M. E.; Savage, M. D.; Cerro, R. L. The Effect of Temperature on Contact Angles and Wetting Transitions for N-Alkanes on PTFE. *J. Colloid Interface Sci.* **2017**, *503*, 159–167. https://doi.org/10.1016/j.jcis.2017.05.003.
(282) Yang, J.; Lee, S.; Lee, E.; Lee, J.; Hong, S. Effect of Solution Chemistry on the Surface Property of Reverse Osmosis Membranes under Seawater Conditions. *Desalination* **2009**, *247* (1–3), 148–161. https://doi.org/10.1016/j.desal.2008.12.020.
(283) Tu, K. L.; Chivas, A. R.; Nghiem, L. D. Effects of Chemical Preservation on Flux and Solute Rejection by Reverse Osmosis Membranes. *J. Memb. Sci.* **2014**, *472*, 202–209. https://doi.org/10.1016/j.memsci.2014.08.052.

(284) Zisman, W. A. Relation of the Equilibrium Contact Angle to Liquid and Solid Constitution. In *Contact Angle, Wettability, and Adhesion*; 1964; pp 1–51. https://doi.org/10.1021/ba-1964-0043.ch001.
(285) Petke, D. F.; Ray, R. B. Temperature Dependence of Contact Angles of Liquids on Polymeric Solids. *J. Colloid Interface Sci.* **1969**, *31* (2), 216–227.
(286) Nilsson, M.; Trägårdh, G.; Östergren, K. The Influence of PH, Salt and Temperature on Nanofiltration Performance. *J. Memb. Sci.* **2008**, *312* (1–2), 97–106. https://doi.org/10.1016/j.memsci.2007.12.059.
(287) Kudin, K. N.; Car, R. Why Are Water-Hydrophobic Interfaces Charged? *J. Am. Chem. Soc.* **2008**, *130* (12), 3915–3919. https://doi.org/10.1021/ja077205t.
(288) Seo, Y.; Jhe, W. Atomic Force Microscopy and Spectroscopy. *Reports Prog. Phys.* **2008**, *71* (1), 016101. https://doi.org/10.1088/0034-4885/71/1/016101.
(289) Kocun, M.; Grandbois, M.; Cuccia, L. A. Single Molecule Atomic Force Microscopy and Force Spectroscopy of Chitosan. *Colloids Surfaces B Biointerfaces* **2011**, *82* (2), 470–476. https://doi.org/10.1016/j.colsurfb.2010.10.004.
(290) Dallin, B. C.; Yeon, H.; Ostwalt, A. R.; Abbott, N. L.; Van Lehn, R. C. Molecular Order Affects Interfacial Water Structure and Temperature-Dependent Hydrophobic Interactions between Nonpolar Self-Assembled Monolayers. *Langmuir* **2019**, *35* (6), 2078–2088. https://doi.org/10.1021/acs.langmuir.8b03287.
(291) Stock, P.; Utzig, T.; Valtiner, M. Direct and Quantitative AFM Measurements of the Concentration and Temperature Dependence of the Hydrophobic Force Law at Nanoscopic Contacts. *J. Colloid Interface Sci.* **2015**, *446*, 244–251. https://doi.org/10.1016/j.jcis.2015.01.032.
(292) Huang, D. M.; Chandler, D. Temperature and Length Scale Dependence of Hydrophobic Effects and Their Possible Implications for Protein Folding. *Proc. Natl. Acad. Sci.* **2000**, *97* (15), 8324–8327. https://doi.org/10.1073/pnas.120176397.
(293) Elimelech, M.; Childress, A. E. *Zeta Potential of Reverse Osmosis Membranes: Implications for Membrane Performance*; 1996.
(294) Mehdizadeh, H.; Dickson, J. M.; Eriksson, P. K. Temperature Effects on the Performance of Thin-Film Composite, Aromatic Polyamide Membranes. *Ind. Eng. Chem. Res.* **1989**, *28* (6), 814–824. https://doi.org/10.1021/ie00090a025.
(295) Madaeni, S. S.; Mansourpanah, Y. Chemical Cleaning of Reverse Osmosis Membranes Fouled by Whey. *Desalination* **2004**, *161* (1), 13–24. https://doi.org/https://doi.org/10.1016/S0011-9164(04)90036-7.
(296) Karan, S.; Jiang, Z.; Livingston, A. G. Sub-10 Nm Polyamide Nanofilms with Ultrafast Solvent Transport for Molecular Separation. *Science (80-.).* **2015**, *348* (6241), 1347–1351. https://doi.org/10.1126/science.aaa5058.
(297) Fujioka, T.; Oshima, N.; Suzuki, R.; Price, W. E.; Nghiem, L. D. Probing the Internal Structure of Reverse Osmosis Membranes by Positron Annihilation Spectroscopy: Gaining More Insight into the Transport of Water and Small Solutes. *Journal of Membrane Science*. 2015, pp 106–118. https://doi.org/10.1016/j.memsci.2015.02.007.
(298) Liu, J.; Huang, T.; Ji, R.; Wang, Z.; Tang, C. Y.; Leckie, J. O. Stochastic Collision-Attachment-Based Monte Carlo Simulation of Colloidal Fouling: Transition from Foulant-Clean-Membrane Interaction to Foulant-Fouled-Membrane Interaction. *Environ. Sci. Technol.* **2020**, *54* (19), 12703–12712.

https://doi.org/10.1021/acs.est.0c04165.
(299) Henis, J. M. S.; Tripodi, M. K. Composite Hollow Fiber Membranes for Gas Separation: The Resistance Model Approach. *J. Memb. Sci.* **1981**, *8* (3), 233–246. https://doi.org/10.1016/S0376-7388(00)82312-1.
(300) Sagle, A. C.; Van Wagner, E. M.; Ju, H.; McCloskey, B. D.; Freeman, B. D.; Sharma, M. M. PEG-Coated Reverse Osmosis Membranes: Desalination Properties and Fouling Resistance. *J. Memb. Sci.* **2009**, *340* (1–2), 92–108. https://doi.org/10.1016/j.memsci.2009.05.013.
(301) Ang, W. S.; Tiraferri, A.; Chen, K. L.; Elimelech, M. Fouling and Cleaning of RO Membranes Fouled by Mixtures of Organic Foulants Simulating Wastewater Effluent. *J. Memb. Sci.* **2011**, *376* (1–2), 196–206. https://doi.org/10.1016/j.memsci.2011.04.020.
(302) Torres, M. L.; Fernandez, J. M.; Dellatorre, F. G.; Cortizo, A. M.; Oberti, T. G. Purification of Alginate Improves Its Biocompatibility and Eliminates Cytotoxicity in Matrix for Bone Tissue Engineering. *Algal Res.* **2019**, *40*, 101499. https://doi.org/10.1016/j.algal.2019.101499.
(303) Miller, D. J.; Paul, D. R.; Freeman, B. D. An Improved Method for Surface Modification of Porous Water Purification Membranes. *Polymer (Guildf).* **2014**, *55* (6), 1375–1383. https://doi.org/10.1016/j.polymer.2014.01.046.
(304) Walker, S. L.; Bhattacharjee, S.; Hoek, E. M. V. V.; Elimelech, M. A Novel Asymmetric Clamping Cell for Measuring Streaming Potential of Flat Surfaces. *Langmuir* **2002**, *18* (6), 2193–2198. https://doi.org/10.1021/la011284j.
(305) Adout, A.; Kang, S.; Asatekin, A.; Mayes, A. M.; Elimelech, M. Ultrafiltration Membranes Incorporating Amphiphilic Comb Copolymer Additives Prevent Irreversible Adhesion of Bacteria. *Environ. Sci. Technol.* **2010**, *44* (7), 2406–2411. https://doi.org/10.1021/es902908g.
(306) Bouchoux, A.; Roux-de Balmann, H.; Lutin, F. Investigation of Nanofiltration as a Purification Step for Lactic Acid Production Processes Based on Conventional and Bipolar Electrodialysis Operations. *Sep. Purif. Technol.* **2006**, *52* (2), 266–273. https://doi.org/10.1016/j.seppur.2006.05.011.
(307) Do, V. T.; Tang, C. Y.; Reinhard, M.; Leckie, J. O. Effects of Hypochlorous Acid Exposure on the Rejection of Salt, Polyethylene Glycols, Boron and Arsenic(V) by Nanofiltration and Reverse Osmosis Membranes. *Water Res.* **2012**, *46* (16), 5217–5223. https://doi.org/10.1016/j.watres.2012.06.044.
(308) Fujioka, T.; Khan, S. J.; McDonald, J. A.; Roux, A.; Poussade, Y.; Drewes, J. E.; Nghiem, L. D. N-Nitrosamine Rejection by Reverse Osmosis: Effects of Membrane Exposure to Chemical Cleaning Reagents. *Desalination* **2014**, *343*, 60–66. https://doi.org/10.1016/j.desal.2013.10.032.
(309) *Standard Methods for the Examination of Water and Wastewater*, 22nd ed.; Rice, E. W., Baird, R. B., Eaton, A. D., Clesceri, L. S., Eds.; American Public Health Association, American Water Works Association, Water Environment Federation, 2012.
(310) Goren, S. L. The Hydrodynamic Force Resisting the Approach of a Sphere to a Plane Permeable Wall. *Colloid Interface Sci.* **1979**, *69* (1), 78–85.
(311) Kang, S.; Subramani, A.; Hoek, E.; Deshusses, M.; Matsumoto, M. Direct Observation of Biofouling in Cross-Flow Microfiltration: Mechanisms of

Deposition and Release. *J. Memb. Sci.* **2004**, *244* (1–2), 151–165. https://doi.org/10.1016/j.memsci.2004.07.011.

Appendix A: Supporting Information for Chapter 2

Membrane Fabrication and Surface Modification

Membrane Fabrication Ultrafiltration (UF) membranes were prepared by non-solvent induced phase inversion; 10 g of polyvinylpyrrolidone (PVP, average MW 50-58 Da, K29-32, Acros Organics) were dissolved in 75 g of 1-methyl-2-pyrrolidinone (NMP, anhydrous, 99.5%, Sigma-Aldrich) at 60 °C for two hours, followed by addition of 15 g of polysulfone (PSF, average Mn ~22,000, beads, Sigma-Aldrich) under stirring at 80 °C. The dope solution was stored overnight in a desiccator to remove any trapped air bubbles. To cast the membranes, a polyethylene terephthalate (PET) non-woven fabric was attached to a glass plate (dimensions 24 × 16 cm^2) using water proof tape (Fisher Scientific). The PET fabric was pre-wetted with NMP, and a Kimwipe (KIMTECH, Kimberly-Clark) was used to evenly distribute and remove excess NMP. A doctor blade (Gardco) was set to a gate height of 0.25 mm and used to apply the dope solution as a film over the PET support. The cast membrane was immediately immersed in a 2-L ultrapure water (18.2 MΩ-cm, Barnstead) coagulation bath for 10 minutes, followed by storage in a 4-L ultrapure water bath for 1 hour. The membranes were then cut into small coupons (~100 cm^2) and stored in ultrapure water at 5-7 °C.

Surface Functionalization with Polydopamine When dopamine (3,4-dihydroxyphenylalanine, DOPA) is buffered to an alkaline pH under aerobic conditions, it forms a supramolecular aggregate known as polydopamine (PDA), that deposits as self-adherent hydrophilic film on the surface of a wide range of organic and inorganic materials[49,73]. PDA has been extensively studied in membrane surface modification for

organic fouling (e.g., oil-in-water emulsions) control[1,49,73,90,121,303]. In this work, we investigate the potential of PDA in mitigating bioadhesion forces. Before PDA deposition, the fabricated UF membrane was clamped between a polypropylene backing and a polypropylene frame with an approximate volume of 30 mL. A DOPA solution was prepared at a concentration of 4 g of DOPA per liter of Trizma buffer (10 mM, BioReagent, Sigma Aldrich), adjusted to pH 8.5 with 1 M NaOH. The DOPA solution was immediately transferred to the frame to initiate PDA deposition on the UF membrane active layer. Deposition was allowed to proceed for 15 minutes in an open-air shaker (MaxQ 2000 Shaker, Thermo Scientific) at ~60 rpm, followed by rinsing with ultrapure water. This procedure was repeated thrice. Coated membranes were stored in ultrapure water at 5-7 °C. We refer to PDA-coated polysulfone UF membranes as PSF-PDA, while the unmodified polysulfone control membranes are designated PSF membranes.

Surface Conditioning with Natural Organic Matter (NOM) Upper Mississippi River NOM (International Humic Substances Society, St. Paul, MN) was used as a model foulant. NOM was dissolved at a concentration of 10 ppm in a solution containing 156.4 mM KCl and 0.5 mM $CaCl_2$. The ionic strength and pH of the prepared solution (158 mM and pH 7.2-7.4) were adjusted to closely approximate those of PBS, to perform experiments under comparable conditions. NOM was deposited as a conditioning film on PSF and PSF-PDA membranes via filtration. Using a stirred filtration cell (Amicon 8010, Millipore), 30 mL of ultrapure water were filtered through the membrane coupons (25 mm in diameter), followed by 100 mL of 10 ppm NOM solution. The transmembrane pressure differential was set to 50 psi. The NOM film was deposited immediately before each experiment.

Membrane Characterization

Contact Angle Membrane surface hydrophilicity was characterized by contact angle goniometry using the sessile drop method. The membranes were dried overnight in a desiccator before measurements. A 1.5 μL DI water drop was placed on the surface of the membrane using a syringe mounted on the goniometer (MCA-3, Kyowa Interface Science Co., Japan), and allowed to equilibrate for 10 seconds before acquiring a digital image. The contact angle was determined from the digital images using a proprietary software; at least 9 different drops were applied to 2 different samples of each membrane type. Contact angle measurements are presented in **Figure 2. 1.**

Zeta Potential The zeta potential of the membrane surfaces was determined from streaming potential measurements using an electrokinetic analyzer (SurPASS, Anton Paar). Two 10 × 20 mm^2 membrane coupons were attached to sample holders of an adjustable gap cell using double-sided tape. Streaming potential measurements were determined in a 1 mM KCl solution over the pH range 4 to 10. The zeta potential was computed from the streaming potential using the Smoluchowski-Helmholtz equation[25,304]. The results are presented in **Figure A. 4**. Two samples were characterized for each membrane type. A validation run was conducted before all experiments using a PVDF sample of known isoelectric point; in all cases, the isoelectric point of PVDF was found to be between 3.7 and 4.3, in agreement with the specifications of the manufacturer.

Surface Roughness Surface roughness was measured using an atomic force microscope (MFP-3D-Bio, Asylum Research) operated in AC mode using Tap300Al-G cantilevers (*k*

= 40 N/m, resonance frequency 300 kHz, Budget Sensors). Images (1 × 1 μm^2) were collected at 0.5 Hz over 5 randomly chosen spots on each membrane type. The root-mean-square (RMS) roughness was obtained from each image. Representative images are presented in **Figure A. 6**.

Permeability Pure water permeability was measured using a stirred ultrafiltration cell (Amicon 8010, Millipore). A 25-mm circular membrane coupon was cut and mounted on the base of the stirred cell. Before permeability measurements, a 30-mL aliquot of ultrapure water was filtered at 50 psi. Flux measurements were then performed at 10, 20, 30, 40, and 50 psi. The permeability was calculated from the slope of the linear fit of flux versus pressure. Coupons from three different membranes of each type were characterized. Results are presented in **Figure A. 7**.

Bacterial Culture Preparation and Growth Conditions

Pseudomonas fluorescens (ATCC 13525) was received in freeze-dried form, transferred to 6 mL of autoclaved Luria broth (LB broth (Miller), Sigma-Aldrich), and incubated for 2 hours at 30 ºC before streaking agar plates. Cell colonies were grown by overnight incubation of the streaked agar plates at 30 °C. To prepare cell suspensions, a bacterial colony was transferred with a sterilized pipette tip to a flask containing 50 mL LB, followed by overnight incubation at 30 °C and 125 RPM shaking speed. Next, the overnight culture was diluted 1:25 in 50 mL LB broth and incubated at 30 °C and 175 RPM for ~3 hours. Cells in mid-exponential growth phase ($OD_{600\ nm} \approx 0.4$ - 0.6) were harvested, centrifuged at 5000g for 1 minute, and suspended in PBS buffer, pH 7.4, by vortexing. This step was

repeated thrice. All materials and reagents used in cell culture were autoclaved (SterilElite24^{TM}, Fisher Scientific) before use.

Batch Bacterial Deposition Experiments

Bacterial deposition experiments were conducted following the method proposed by Adout et al.[305] A *P. fluorescens* bacterial culture was prepared and suspended in PBS as described above. Membrane coupons (~1 × 1 cm^2) were then incubated at room temperature in 4 mL of bacterial suspension in an incubator with shaking speed ~30 rpm for 1 hour. The coupons were gently rinsed with PBS to remove unattached bacteria. The number of adhered bacteria was determined by confocal microscopy. Each membrane coupon was mounted on a glass slide and ~50 μL of Live/Dead assay and 150 μL of PBS were added over the membrane before sealing the coverslip. An inverted confocal microscope (FV1000, Olympus) was used to image ten 100 × 100 μm^2 randomly selected scan areas on each membrane type. The total number of adhered cells (live and dead) was identified using Olympus FluoView software. The results are presented in **Figure A. 19**.

Representative Force Curve

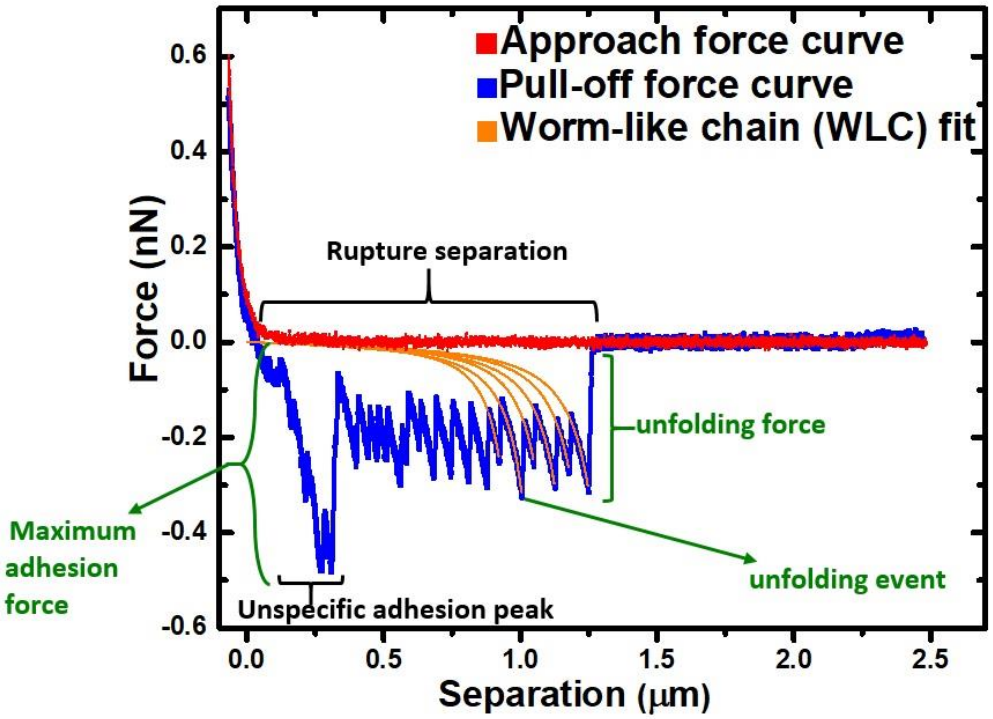

Figure A. 1. Sample force curve showing definitions of maximum adhesion force, rupture separation, and unfolding force used in the paper; the orange curve shows the WLC model fit to the sawtooth-like discontinuities, characteristic of macromolecule unfolding.

Fourier Transform Infrared Spectroscopy (FTIR)

FTIR analysis was performed on pristine and NOM-conditioned PSF and PSF-PDA membranes using a Thermo Scientific Nicolet iS50 FT-IR spectrometer. To prepare the samples for analysis, the NOM film was deposited on PSF and PSF-PDA membranes (cf. Supporting Text; Appendix A); pristine and NOM-conditioned membranes were immersed in PBS and NOM solution, respectively, for one hour. Afterwards, membranes were desiccator-dried for two hours prior to FTIR analysis. The results are presented in **Figure A. 3** and **Figure A. 3**.

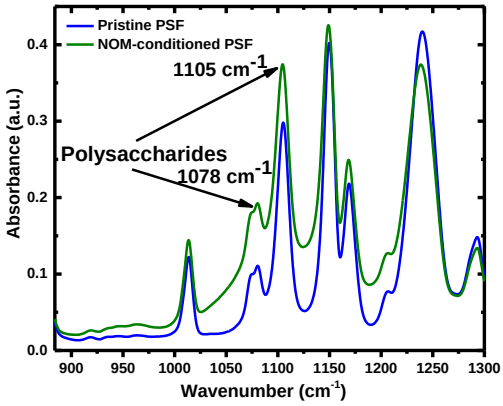

Figure A. 2. FTIR spectra of pristine and NOM-conditioned PSF membranes.

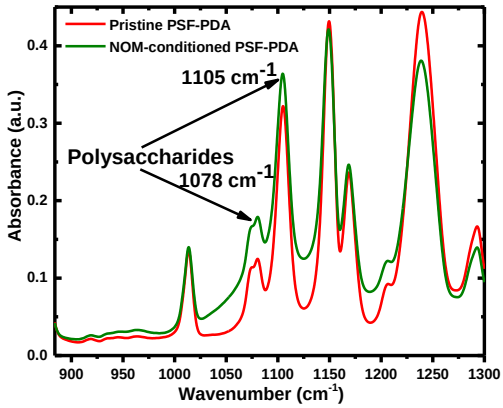

Figure A. 3. FTIR spectra of pristine and NOM-conditioned PSF-PDA membranes.

Zeta Potential of UF Membranes

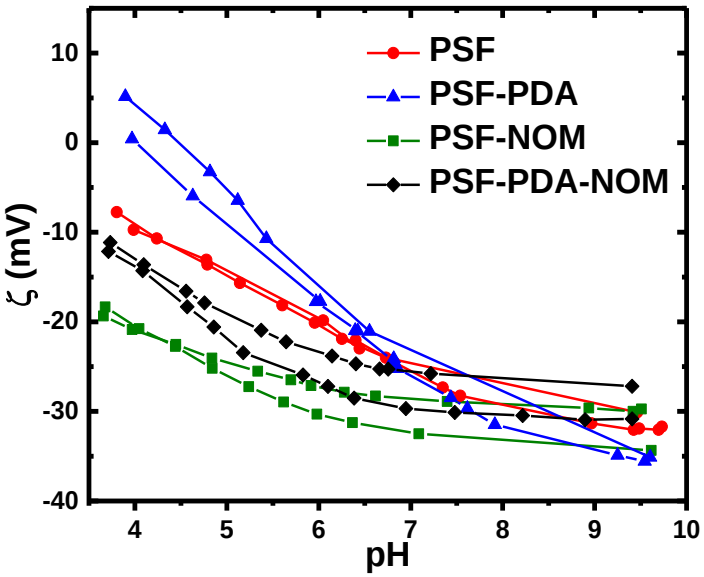

Figure A. 4. Zeta potential of PSF, PSF-PDA, and NOM-conditioned PSF and PSF-PDA membranes over the pH range 4-10. Experiments were performed in a 1 mM KCl background electrolyte. Results are shown for two samples of each membrane type.

Zeta Potential of Bacterial Cells

Zeta potential measurements of *P. fluorescens* (ATCC 13525) cells suspended in PBS and NOM solution (pH 7.2-7.4) are shown in **Figure A. 5**. as a function of the ionic strength. PBS and 10 mg/L NOM solution (supplemented with 156.4 mM KCl and 0.5 mM $CaCl_2$) were diluted to the ionic strength indicated in the abscissa. Measurements were performed using a Stabino particle charge instrument. **Figure A. 5**. also shows the zeta potential measurements of PBS and NOM solution dilutions (without cells) as control measurements.

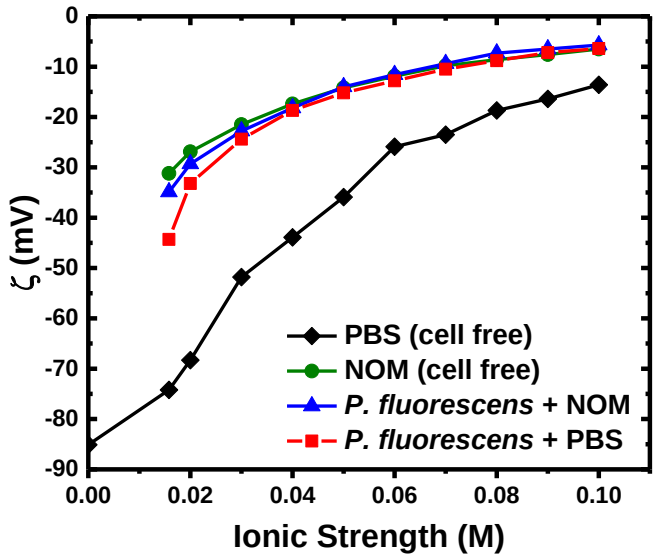

Figure A. 5. Zeta potential measurements of *P. fluorescens* cells at different dilutions of PBS (pH 7.2-7.4) and NOM solution prepared as mentioned in Appendix A. Cell-free control measurements were performed in the same dilutions of PBS and 10-mg/L NOM solution.

Surface Roughness

A B

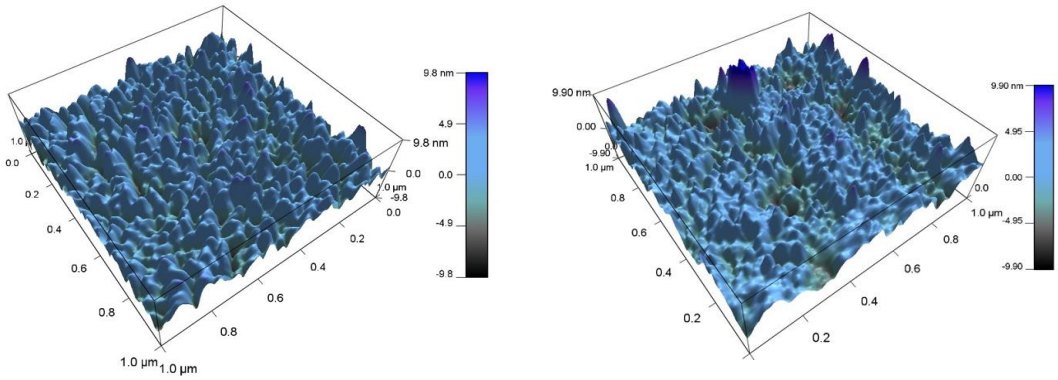

Figure A. 6. AFM surface roughness of (A) PSF (2.45 ± 0.32 nm) and (B) PSF-PDA (3.74 ± 1.44 nm) membranes.

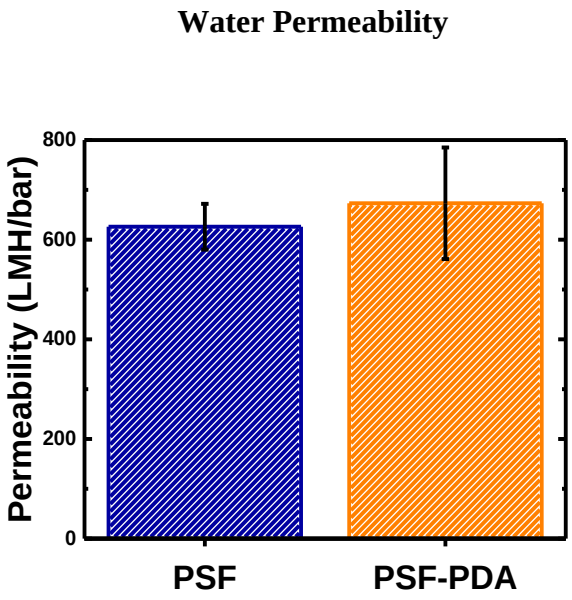

Figure A. 7. Water permeability coefficient of PSF and PSF-PDA membranes. The results shown are averages of 3 membrane coupons of each type (LMH: L m^{-2} h^{-1}). Error bars denote one standard deviation.

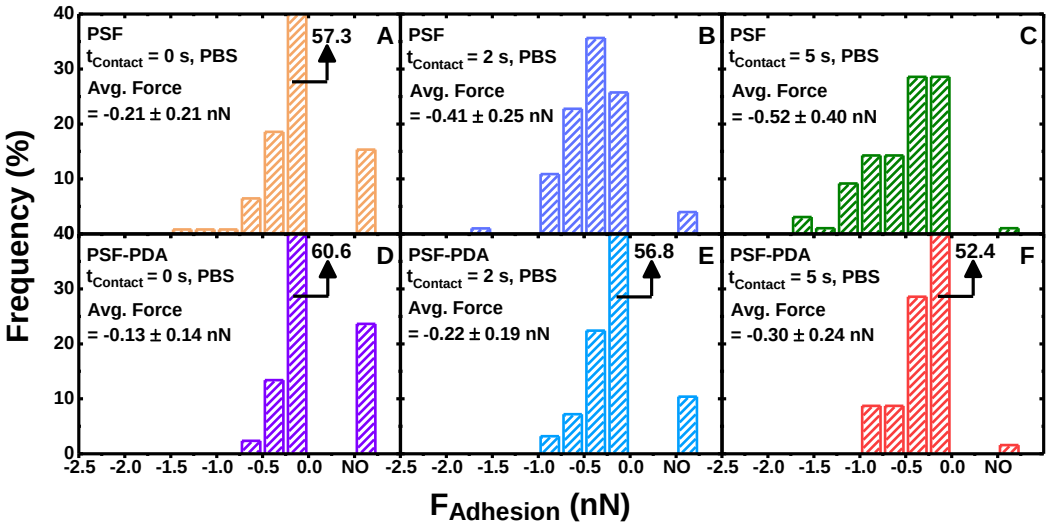

Figure A. 8. Distribution of maximum adhesion forces of a single *P. fluorescens* cell on: (A-C) polysulfone membranes (PSF); (D-F) polydopamine-coated polysulfone (PSF-PDA) membranes. Cell-substrate adhesion forces were measured at different contact times ($t_{Contact}$), denoted in the inset alongside the histogram average and standard deviation. Forces tallied under the "NO" column correspond to weak adhesion events with maximum $|F_{Adhesion}| < 38$ pN; these weak adhesive forces were of the same order as the thermal noise observed in the disengaged cantilever. Forces counted under "NO" were set equal to 0 nN in the calculation of the averages shown in the inset and Figure 2 (A). Measurements were performed in PBS buffer (pH 7.4). The number of force curves, n, measured with c different bacterial probes for each histogram is: (A) n = 124, c = 6; (B) n = 101, c = 5; (C) n = 98, c = 5; (D) n = 127, c = 6; (E) n = 125, c = 6; (F) n = 126, c = 6.

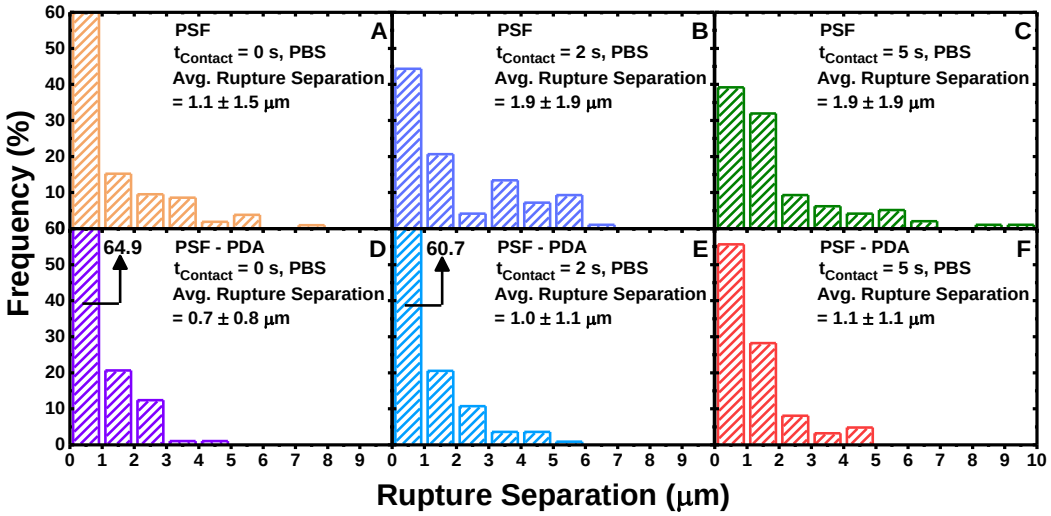

Figure A. 9. Distribution of rupture separation (distance from the membrane surface at which adhesion forces vanish) for a single *P. fluorescens* cell on: (A-C) polysulfone (PSF) membranes; (D-F) polydopamine-coated polysulfone (PSF-PDA) membranes. Measurements were performed at different contact times ($t_{Contact}$), denoted in the inset alongside the histogram average and standard deviation. The experimental conditions and sample sizes are as per **Figure A. 8**.

Cell-Free Control Measurements

Control measurements of the adhesion force between a tipless (cell-free) wPDA-coated cantilever and PSF or PSF-PDA membranes were collected for $t_{Contact}$ = 5 s. A total of 120 force curves were collected over each membrane type (12 different locations; 10 force curves per location). As shown in **Figure A. 10**. - **Figure A. 12**., control wPDA measurements differed significantly from those performed with a bacterial probe. The mean adhesion force of control measurements was ~ -1 nN (**Figure A. 10**. - **Figure A. 12**), compared to -0.52 nN and -0.30 nN for bacterial probes interacting with PSF and PSF-PDA membranes at $t_{Contact}$ = 5 s, respectively. Similarly, interactions between the cantilever and the surfaces exhibited significantly shorter rupture separations (**Figure A. 13** - **Figure A. 15**) compared to those of the bacterial probe.

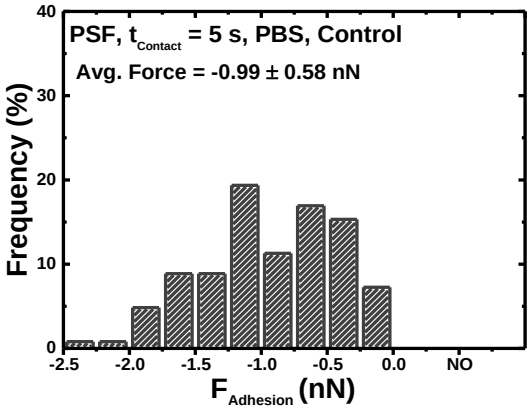

Figure A. 10. Distribution of maximum adhesion forces between a (control) wPDA-coated cantilever and a PSF membrane in PBS buffer, pH 7.4 (force speed 400 nm/s; 600 pN trigger force; $t_{Contact}$ = 5 s).

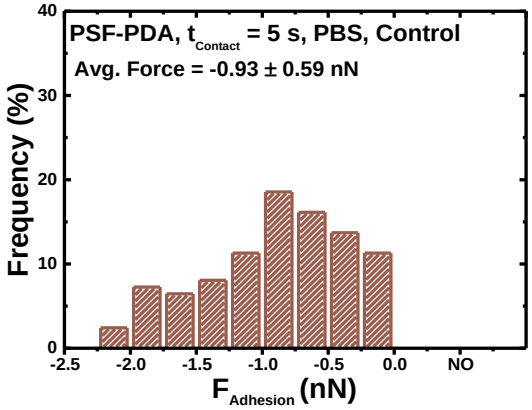

Figure A. 11. Distribution of maximum adhesion forces between a (control) wPDA-coated cantilever and PSF-PDA membranes in PBS buffer, pH 7.4. Experimental conditions as in the caption of **Figure A. 10**.

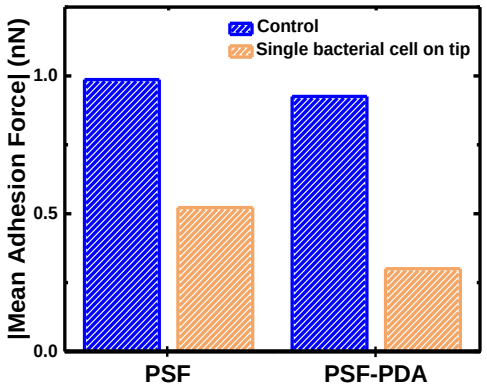

Figure A. 12. Comparison of the average maximum adhesion force determined with (control) wPDA-coated cantilevers and single *P. fluorescens* bacterial cells on PSF and PSF-PDA membranes. Experimental conditions are indicated in the caption of **Figure A. 10**.

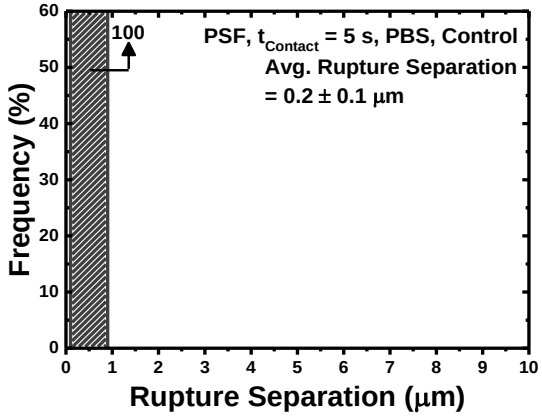

Figure A. 13. Distribution of rupture separation for interaction between a (control) wPDA-coated cantilever and PSF membranes. Experimental conditions as in the caption of **Figure A. 10**.

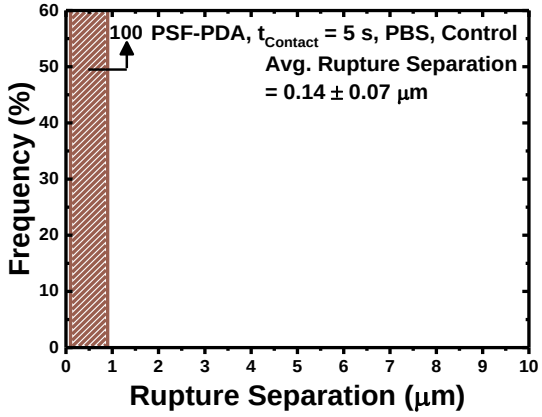

Figure A. 14. Distribution of rupture separation for interaction between a (control) wPDA-coated cantilever and PSF-PDA membranes. Experimental conditions as in the caption of **Figure A. 10**.

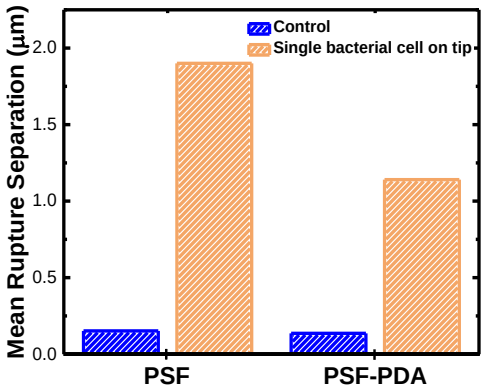

Figure A. 15. Comparison of the average rupture separation determined with (control) wPDA-coated cantilevers and single *P. fluorescens* bacterial cells on PSF and PSF-PDA membranes. Experimental conditions are indicated in the caption of **Figure A. 10**.

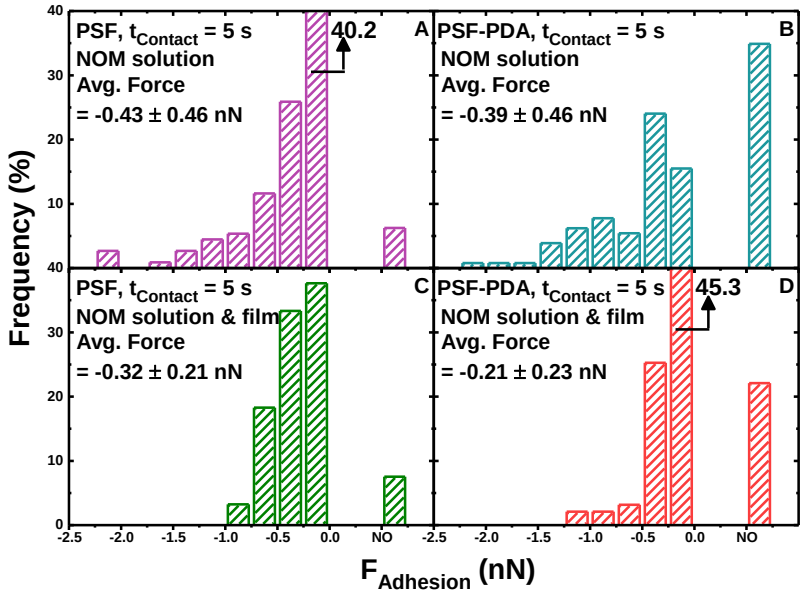

Figure A. 16. Distribution of maximum adhesion forces of a single *P. fluorescens* cell on polysulfone membranes (PSF, A and C) and polydopamine-coated polysulfone membranes (PSF-PDA, B and D). All experiments were conducted in aqueous solution containing 10 ppm NOM, ionic strength 158 mM, pH 7.2-7.4. Panels C and D show experiments wherein an NOM conditioning film was deposited on the membranes. All experiments were performed at force speed 400 nm/s, 600 pN trigger force, and contact time 5 s. Forces counted under "NO" (corresponding to $|F_{\text{Adhesion}}| < 38$ pN) were set equal to 0 nN in the computation of the averages shown in the inset and Figure 3 (A). The number of force curves, n, measured with c different

bacterial probes for each histogram is: (A) n = 112, c = 4; (B) n = 129, c = 3; (C) n = 93, c = 3; (D) n = 95, c = 3.

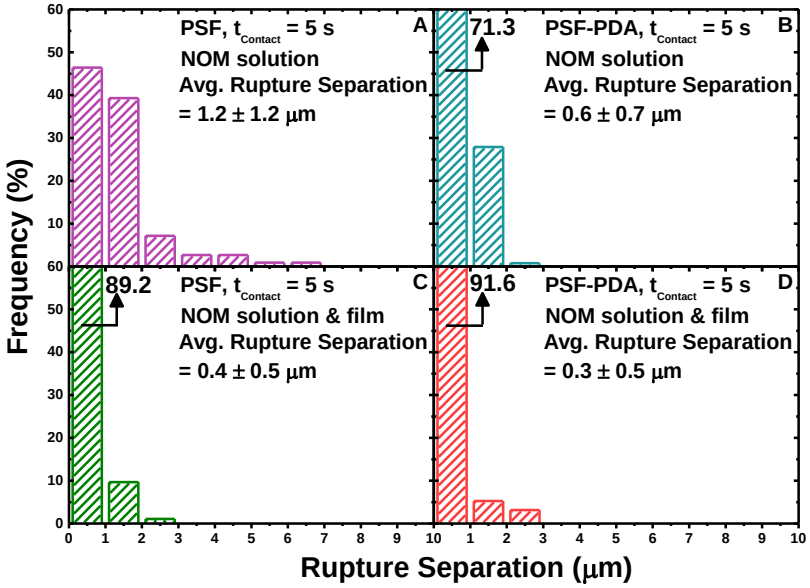

Figure A. 17. Distribution of rupture separation (distance from the membrane surface at which adhesion forces vanish) for a single *P. fluorescens* cell on polysulfone membranes (PSF, A and C) and polydopamine-coated polysulfone membranes (PSF-PDA, B and D). All experiments were conducted in aqueous NOM solution containing 10 ppm NOM, ionic strength 158 mM, pH 7.2-7.4. NOM conditioning film was deposited on membranes corresponding to experiments of panels C and D. The experimental conditions and sample sizes are as per **Figure A. 16**.

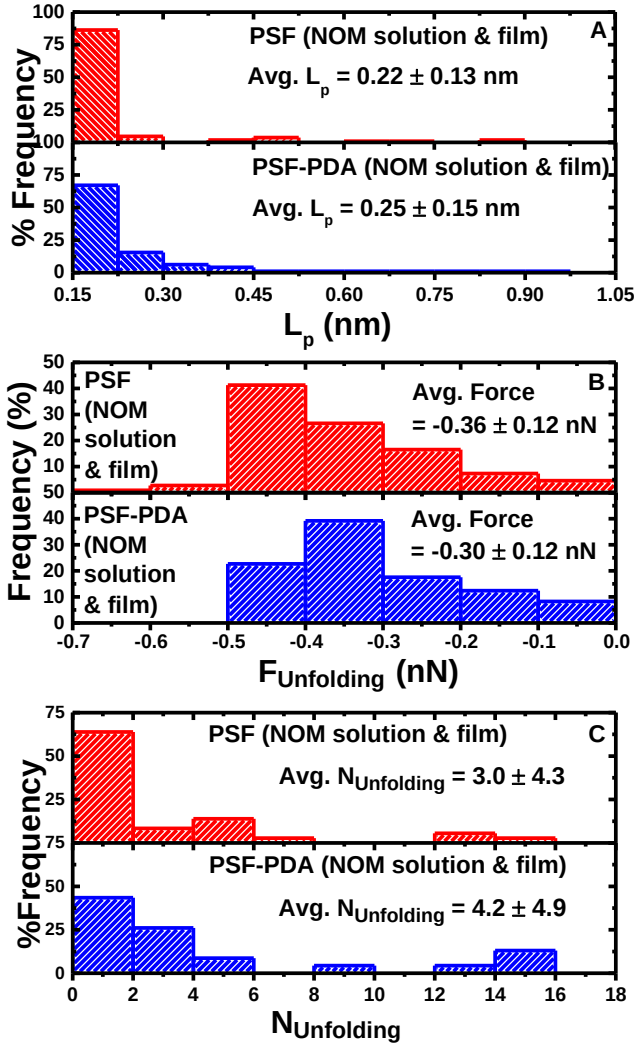

Figure A. 18. (A) Distribution of best-fit persistence length values (L_p), obtained from WLC model fits to the pull-off force curve of single P. fluorescens cells on NOM-coated membranes. (B) Distribution of the unfolding forces on NOM-coated membranes ($F_{Unfolding}$, the force measured at the sawtooth peak, cf. **Figure A. 1.**), defined as the force necessary to unwind a macromolecular domain. (C) Distribution of the number of unfolding events observed on NOM-coated membranes ($N_{Unfolding}$, the number of sawtooth-like peaks per cell pull-off). The mean of each histogram is shown in the inset. Data were collected with single bacterial cells over NOM-coated PSF membranes (upper panel in A, B and C) and NOM-coated PSF-PDA membranes, at $t_{Contact}$ = 5 s. The solution chemistry was 10 ppm NOM, ionic strength 158 mM, pH 7.2-7.4. The histograms reflect 109 WLC fits to sawtooth-like unfolding events, identified in 36 retraction force curves over PSF membranes; and 97 sawtooth-like unfolding events observed in 23 retraction force curves over PSF-PDA membranes.

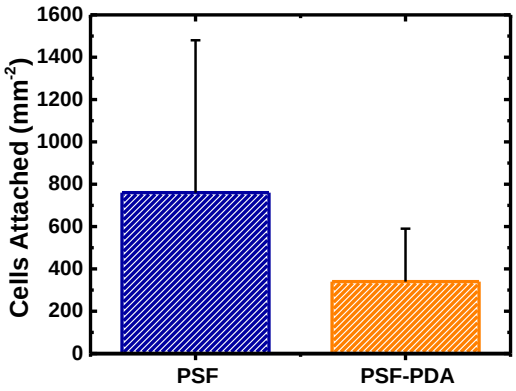

Figure A. 19. Average number of cells adhered on each membrane type, determined via bacterial deposition experiments. Ten randomly selected 100 × 100 μm^2 regions were scanned, and the total number of adhered cells was determined by live/dead staining (p = 0.11, two-sided, unpaired t-test).

Appendix B: Supporting Information for Chapter 3

Membrane Characterization

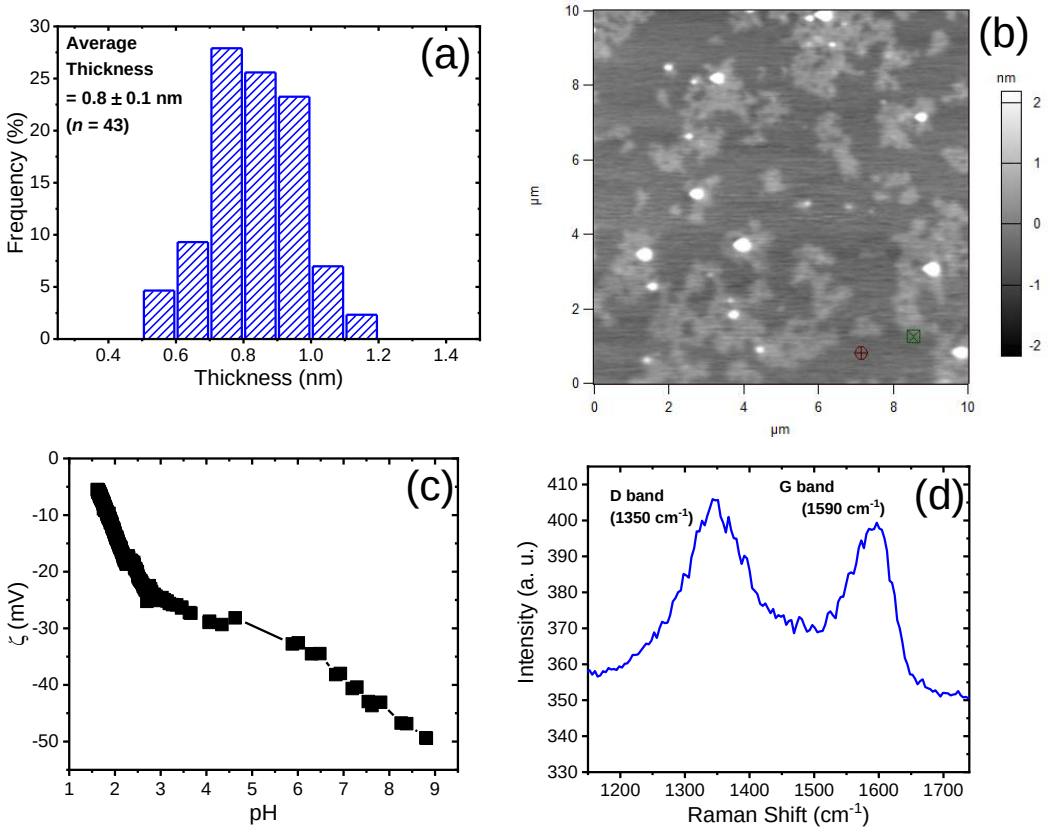

Figure B. 1. Characterization of graphene oxide (GO) nanosheets: (a) distribution of nanosheet thickness determined by AC mode AFM in air using an AC160TS-R3 Si cantilever (Olympus) with nominal spring constant 26 N m^{-1} and resonance frequency 300 Hz; (b) representative AFM image of GO nanosheets deposited on a Si substrate; (c) ζ-Potential of GO in aqueous dispersion at a concentration of 250 µg mL^{-1}, determined with a Stabino zeta potential analyzer; (d) Raman spectrum of GO nanosheets deposited on a silicon wafer.

Bacterial Culture Preparation and Deposition Assay

Bacterial Deposition Assay To complement our AFM results, we carried out a bacterial deposition assay to evaluate the bioadhesion propensity of the substrates. The assay entails exposure of the membrane surfaces to a *P. fluorescens* suspension under agitation, followed by colony counting from irreversibly adhered cells.[196] *P. fluorescens* ATCC 13525 was cultured overnight in 50 mL of autoclaved LB broth at 30 °C in an incubator (ThermoScientific MAXQ4450) under stirring (125 rpm). Bacterial suspensions were diluted 1:25 in autoclaved LB broth, and incubated for a further three hours at 175 rpm and 30 °C. Cells were harvested in mid-exponential phase ($OD_{600\ nm} \approx 0.6$) and centrifuged thrice at 5000g (for 1 min), re-suspending the pellet after each centrifugation in 1 mL PBS (pH 7.4). After the final re-suspension, 1-cm^2 substrate coupons were placed at the bottom of scintillation vials and each was immersed in 1 mL of the bacterial suspension, such that the entire coupon was fully covered by the liquid. The scintillation vials were then placed in the incubator (ThermoScientific MAXQ4450) at 30 °C under 175 rpm agitation. After 1 hour, substrates were removed from the suspension, gently rinsed with PBS, and placed in 10 mL of fresh PBS in 50-mL falcon tubes. Following bath sonication for 10 minutes, the resulting suspension was diluted 1:100, and a 50-µL aliquot of the dilution was smeared over an agar plate with a sterilized glass rod. After incubation overnight at 30 °C, the colonies were counted. This experiment was repeated two additional times for each substrate type for a total of three replicates.

The results of the bacterial deposition assay are presented in **Figure B. 2.**, showing the number of colony forming units (CFU) normalized by the PES control. Adhesion is significantly mitigated on PES-GO substrates, with the number of colonies on the PES-GO

surface being 8.1% of the control PES following a 1-h exposure ($p < 0.05$, one-sided unpaired *t*-test).

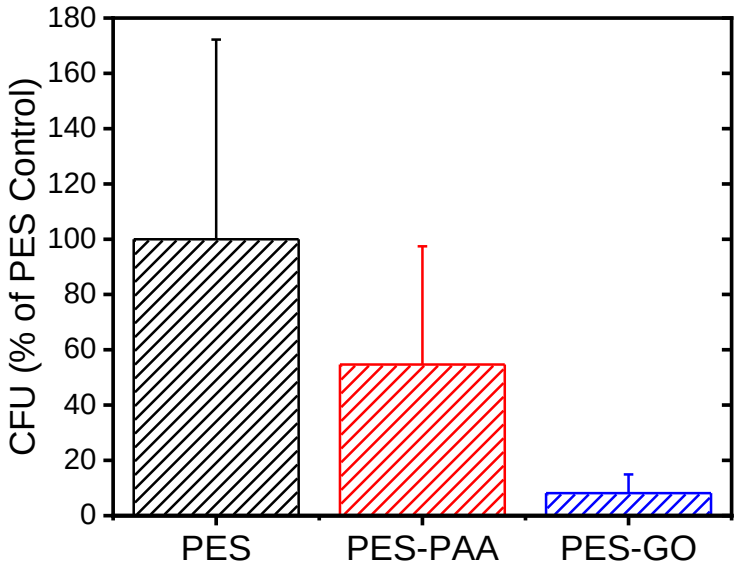

Figure B. 2. Bacterial deposition assay of pristine PES, poly(acrylic acid) (PAA)-modified PES (PES-PAA), and GO-modified PES (PES-GO) substrates. Colony-forming units (CFU) are shown as % of the PES control. Error bars denote the standard deviation of three experiments.

It is important to note that the CFU data in **Figure B. 2.** are possibly influenced by the cytotoxicity of GO.[191,192,196,234] Thus, the precipitous drop in CFU count on PES-GO compared to PES and PES-PAA may be due to a combination of lower adhesion and GO's biocidal activity. However, the relative contributions to the CFU count of adhesion mitigation (due to the interfacial properties of PES-GO) and biocidal activity cannot be disentangled with this simple colony counting assay, and thus would require further investigation.

Membrane Transport Properties

Characterization of Membrane Transport Properties The water permeability coefficient (A) of the membranes was determined in a laboratory-scale filtration apparatus equipped with a crossflow cell (CF042D, Sterlitech, with active membrane area, A_m, of 42.1 cm^2), pump (HydraCell M-03S, Wanner Engineering), and temperature-controlled stainless steel feed reservoir. Membranes were compacted with a distilled water feed for 24 hours at a transmembrane pressure difference (Δp) of 50 psi and crossflow velocity of 0.08 m s^{-1}. Following compaction, measurements of the steady-state permeate flow rate were recorded every second for 1 hour at Δp = 50 psi and 20 °C with a digital flow meter (SLI, Sensirion). The average permeate flow rate, Q_p, was used to compute the water permeability coefficient from $A = Q_p/(A_m \Delta p)$. For control polyethersulfone (PES) membranes, the flux through the membranes was determined by weighing the permeate, since the permeate flow rate exceeded the maximum flow rate measurable with the digital flow meter. Four poly(acrylic acid)-modified (PES-PAA), four GO-modified (PES-GO) and two control PES membranes were characterized.

Effect of Surface Functionalization on Water Permeability and Ion Rejection Surface modification of the PES membranes resulted in additional hydraulic resistance that decreased the water permeability coefficient (A). For pristine PES we find A = 102.1 ± 3.5 L m^{-2} h^{-1} bar^{-1}. On the other hand, for PES-PAA membranes (prepared by acrylic acid polymerization with 10-s UV exposure), we find A = 9.0 ± 1.8 L m^{-2} h^{-1} bar^{-1}, while for PES-GO, A = 7.0 ± 0.7 L m^{-2} h^{-1} bar^{-1}, i.e., the covalently bonded GO layer further decreases water permeability. We also determined the Na_2SO_4 rejection coefficient (R) at Δp = 50 psi

(feed concentration = 10 mM) for the functionalized membranes using a conductivity probe, finding R = 21.4% and 42.7% for PES-GO and PES-PAA, respectively. The A coefficient and ion rejection of PES-PAA and PES-GO materials are similar to those of nanofiltration membranes.[306,307] Additional experiments with PES-PAA membranes prepared with 20-60 sec UV irradiation resulted in steep loss in water permeability (results not shown), due to the formation of a dense PAA layer (observe the prominent carboxyl band at 1700 cm^{-1} when the irradiation time was ≥ 20 s, **Figure 3. 2.**).

Representative Force Curve

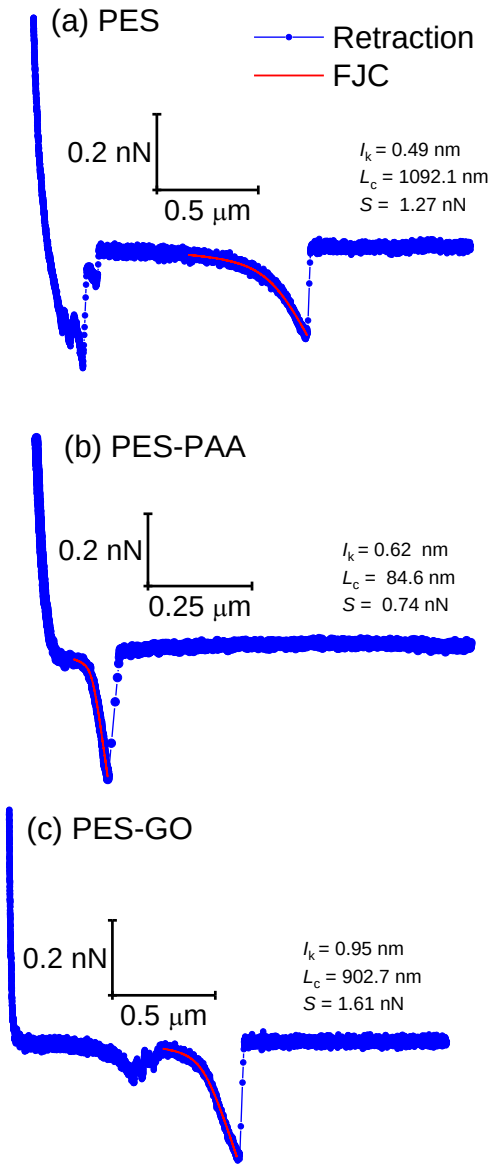

Figure B. 3. Representative retraction force (F)-elongation (z) curves for different membrane substrates (see caption) recorded with *P. fluorescens* bacterial probes. The data show fits of the extended freely-jointed chain (FJC) model, given by $z(F) = L_c\left[\coth\left(\frac{FI_k}{k_BT}\right) - \frac{k_BT}{FI_k}\right]\left(1 + \frac{F}{S}\right)$, where L_c is the contour length, I_k is the Kuhn length, and S is the stretch modulus of the polymer; k_B and T = 298.15 K are Boltzmann's constant and absolute temperature, respectively. Best-fit values of L_c, I_k and S are given in the caption. Due to the thermal noise underlying the measurements (≈ 30 pN), the fitted region of the force-extension curves was smoothed using a locally weighted least-squares smoothing algorithm (loess) implemented in Origin 2018 (Northampton, MA). FJC parameters were obtained by non-linear regression of the smoothed data using the function nlinfit in Matlab R2018a (MathWorks, Natick, MA).

Appendix C: Supporting Information for Chapter 4

Reverse osmosis setup, membrane transport properties and fouling experiments

Reverse osmosis setup We conducted fouling experiments in a laboratory-scale membrane filtration system comprising a crossflow cell (CF042D, Sterlitech, Kent, WA) with 42-cm^2 active membrane area and a 20-L stainless steel feed tank. The feed temperature was set by a portable chiller (6500 series, Polyscience) equipped with a heat exchange coil immersed in the feed tank. A high-pressure pump (HydraCell M-03S, Wanner Engineering, Minneapolis, MN) circulated the feed solution. The permeate flowrate was recorded with a digital flow meter (SLI-2000, Sensirion, Stäfa, Switzerland) and logged to a computer every 0.2 s then used to calculate permeate flux. The system was operated in closed-loop mode, recyling the permeate and retentate streams to the feed tank.

Determination of water permeability coefficient Membranes were compacted with an ultrapure (UP) water (18.2 MΩ-cm, Barnstead) feed at 500-580 psi and 25 ˚C until a steady-state permeate flux was observed (typically within ~60 hours). Next, the transmembrane pressure difference was adjusted so that the permeate flux was 20 ± 1 L m^{-2} h^{-1} (LMH), typical of wastewater reclamation by RO,[12,308] at 15.8 cm s^{-1} crossflow velocity. At this stage, the water permeability coefficient at 25 °C ($A_{w,25}$) was calculated. Next, the chiller settings were adjusted to maintain the feed at the desired temperature, T = 27, 35, or 40 ˚C, and the pressure difference ($\Delta p_{w,T}$) was reduced to maintain a pure water flux of $J_{w,T}$ = 20 ± 1 LMH at the corresonding temperature T. The system was run overnight

to reach steady-state operation at T, after which the water permeability coefficient at T ($A_{w,T}$) was calculated using $A_{w,T} = J_{w,T}/ \Delta p_{w,T}$.

Fouling experiments To begin the fouling experiment, the pure water feed was replaced with foulant-free synthetic wastewater (SWW) with the following composition: 0.45 mM KH_2PO_4, 0.935 mM NH_4Cl, 0.5 mM $CaCl_2$, 0.5 mM $NaHCO_3$, 9.20 mM NaCl, and 0.61 mM $MgSO_4$.[117,265] This synthetic wastewater recipe is representative of secondary effluent in certain wastewater treatment plants in California. The system was again allowed to reach steady state at feed temperature T = 27, 35, or 40 ˚C and a baseline permeate flux J = 20 ± 1 LMH. The conductivity of feed and permeate was measured using a conductivity meter with automatic temperature compensation (WD-35604-00, Con 6+ Meter, Oakton) to determine conductivity rejection.[117] Finally, the synthetic wastewater feed was supplemented with sodium alginate (SA) foulant solution to initiate the accelerated fouling experiment at an alginate feed concentration of 250 mg L^{-1} while recording the permetate flow for 24 hours. Feed and permeate samples were collected 2 and 24 hours after the addition of alginate to determine conductivity and total organic carbon (TOC) TOC rejection. TOC was measured using a Sievers 900 portable TOC analyzer (GE Analytical Instruments, Boulder, CO) that uses the 5310C national environmental methods index (NEMI) standard method.[309] The feed was diluted 20x before analysis while the permeate was analyzed without dilution.

Fouling of Reverse Osmosis Membranes for CML experiments To perform CML experiments over a fouled membrane, an alginate layer was deposited on a pristine

membrane using a dead-end filtration cell (Amicon stirred cell 8010, Millipore). To this end, 3 mL of synthetic wastewater (SWW) prepared as described in section 4.3.2, supplemented with 50 ppm sodium was filtered through the membrane at 60 psi for 45 minutes.

Characterization of membrane interfacial properties

Contact angle The wettability of pristine ESPA2 membranes as a function of temperature was evaluated in terms of water contact angle measurements using the sessile drop method. Desiccator-dried membrane coupons were attached to a glass slide using two-sided tape (Scotch®, 3M). A goniometer (DSA30S, Krüss) equipped with a temperature-controlled chamber (TC30) and temperature-controlled liquid dispenser (TC 3212) was used to measure the contact angle of 2-µL water droplets deposited on the membrane substrate. Right and left angles were determined from digital images using the proprietary ADVANCE software of the instrument for a total of 20 contact angle measurements at each temperature. Measurements were collected at least 15 minutes after both the chamber and UP water reached the set-point temperature (T = 27, 35, and 40 ºC). Right and left side contact angles were immediately recorded after the 2 µL water drop was deposited.

Roughness The nanoscale surface roughness of pristine membranes was measured by tapping mode AFM in aqueous solution using an atomic force microscope (MFP-3D-Bio, Asylum Research) equipped with a temperature-controlled fluid cell. AFM scanning was performed in foulant-free synthetic wastewater (I = 14.7 mM, see section S.2) at 27, 35, and 40 ºC using SNL-10 probes (cantilever "C", nominal k = 0.24 N/m, f = 56 kHz, Bruker). The temperature of the fluid cell was increased from ambient to the target temperature T =

27, 35, or 40 °C (± 0.2 °C) at a rate of 1 ºC/min. After allowing the AFM to equilibrate at the target temperature for at least an hour, the cantilever resonance frequency was calibrated. Three 5 × 5 μm^2 scans were collected at each temperature (27, 35, or 40 °C) at a 0.25 Hz scan rate, after which the root-mean-square (RMS) roughness (R_{RMS}) of 5 random 1 × 1 μm^2 subareas on each image were computed for a total of 15 R_{RMS} values.

Surface charge An electrokinetic analyzer (SurPASS, Anton Paar) was used to measure the streaming potential of ESPA2 membranes in a 1 mM KCl background electrolyte solution. Two 10 × 20 mm^2 membrane coupons were attached to sample holders of an adjustable gap cell. The electrolyte solution was maintained at a constant temperature (monitored using a thermocouple connected to the electrokinetic analyzer) by placing the solution on a heating stir plate. The zeta potential was calculated from the streaming potential using the Smoluchowski-Helmholtz equation. Prior to the measurements, an instrument validation run was carried out using a cotton cloth (~ 4 × 4 cm^2) following a protocol provided by the manufacturer. Streaming potential data were collected over the pH range 4-10 by addition of aliquots of 0.05 mM NaOH or HCl. Additional details of zeta potential measurements can be found in our previous work.[72,74,199] Streaming potential measurements were carried out at 27 °C and 35 °C only, as the maximum operating temperature of the instrument is 40 °C.

Calculation of permeate drag force

The approach loading force (also known as trigger force) exerted on the colloidal probe during AFM force measurements was set to a value representative of the drag force (F_D) exerted on a colloidal particle during membrane filtration. The permeate drag force (F_D) was calculated following the analysis by Goren[310], where the resistance to the approach of a sphere is affected by the permeability of the membrane (considered as a permeable wall). Goren's analysis[310] leads to the following expression for the permeate drag force,

$$F_D = -6\pi\mu a_p J \Phi_H \qquad \text{(C.1)}$$

where F_D is the permeate drag force (N), and the negative sign indicates that the force is normal to and directed toward the surface of the membrane[311]; μ is the dynamic viscosity of water (kg m^{-1} s^{-1}); a_p is the colloidal probe radius (m); J is the permeate water flux (m s^{-1}); and Φ_H is a hydrodynamic correction factor to Stokes drag force.[310,311]

The hydrodynamic resistance to the particle motion toward the membrane decreases with increasing permeability. When the particle is in contact with the permeable wall, the hydrodynamic correction factor is given by Goren[310],

$$\Phi_H = \left(\frac{2R_m a_p}{3}\right)^{\frac{1}{2}} \qquad \text{(C.2)}$$

where $R_m = \frac{\Delta p}{\mu J}$ is the membrane hydraulic resistance (m^{-1}), and Δp is the transmembrane pressure difference (Pa),

The value of R_m of ESPA2 RO membranes was determined experimentally in a laboratory-scale crossflow RO setup operating at a pure water flux $J = 20 \pm 1$ LMH and 25 ˚C. Three

membrane specimens were thus characterized. Flux and corresponding transmembrane pressure values are shown in **Table C. 1.** R_m was calculated for each membrane specimen; the resulting values were within the range of typical RO resistance values (5×10^{13} - 1×10^{15} m^{-1}).[67] Using a_p = 2 μm (the radius of the CML particle), Φ_H was calculated using equation C.2 and used to find the drag force from C.1.

Table C. 2. Experimentally determined pure water flux (J), calculated membrane resistance (R_m) and permeate drag force (F_D).

Δp (bar)	J_w (LMH)	R_m (m^{-1})	Hydrodynamic Correction Factor Φ_H	F_D (nN)
4.34	20.1	8.73×10^{13}	1.08×10^{4}	2.02
4.83	20.0	9.77×10^{13}	1.14×10^{4}	2.13
4.27	19.6	8.81×10^{13}	1.08×10^{4}	1.98
Average				2.04

Supporting Results

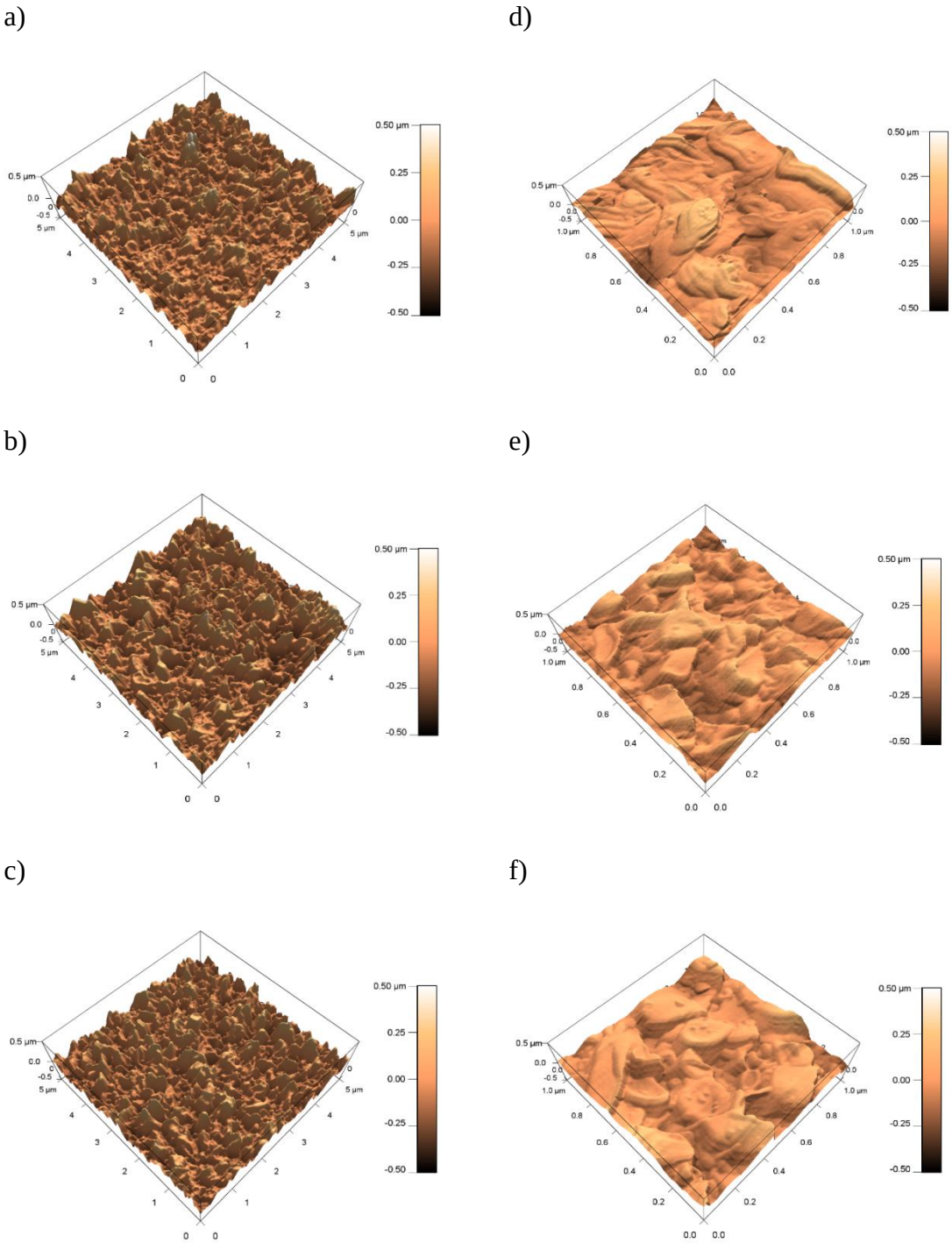

Figure C. 1. AC-mode AFM images of pristine ESPA2 membranes scanned in foulant-free synthetic wastewater (pH 7.4; I = 14.7 mM) at 27 °C (a, d), 35 °C (b, e), and 40 °C (c, f). Left column: 5 × 5 μm^2 scan area. Right column: 1 × 1 μm^2 scan area.

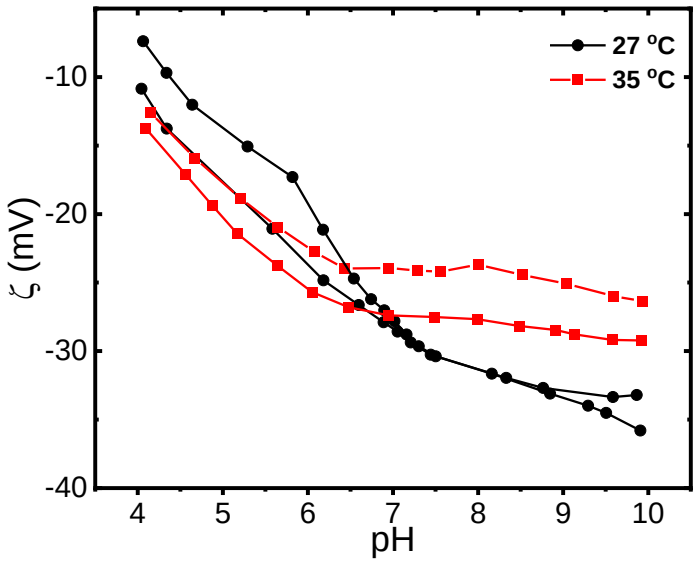

Figure C. 2. Zeta potential measurements of pristine ESPA2 membranes at 27 °C and 35 °C using 1 mM KCl solution.

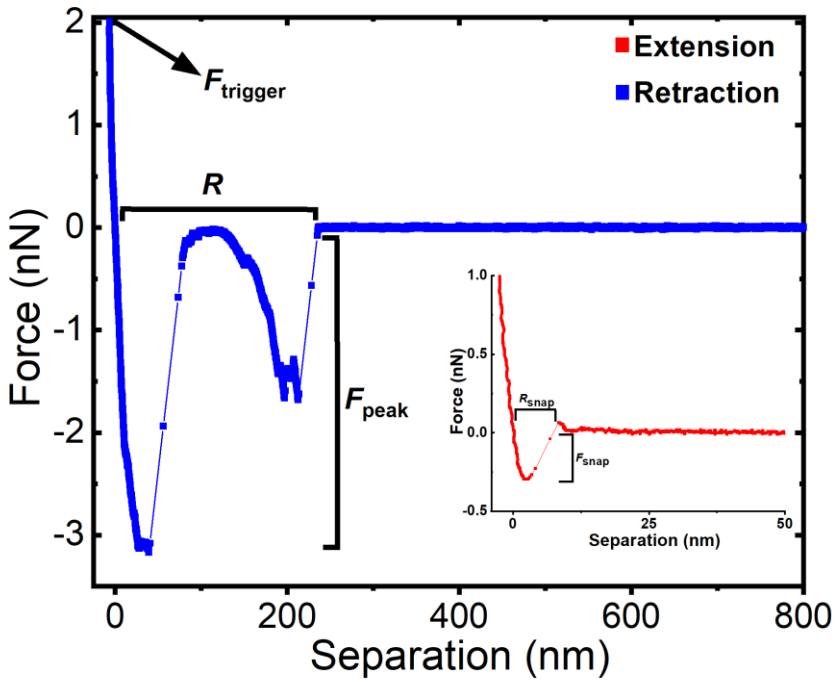

Figure C. 3. Representative retraction force curve and approach force curve (shown in the inset) of a CML colloidal probe on an ESPA2 pristine membrane at 27 °C. Data were collected in synthetic wastewater supplemented with 20 mg L^{-1} sodium alginate ($t_{contact}$ = 5 s; $F_{trigger}$ = 2 nN; pH 7.4; I = 14.7 mM). The curve shows the definition of the peak adhesion force (F_{peak}), snap-in force (F_{snap}), trigger force ($F_{trigger}$), rupture separation (R), and snap-in separation (R_{snap}).

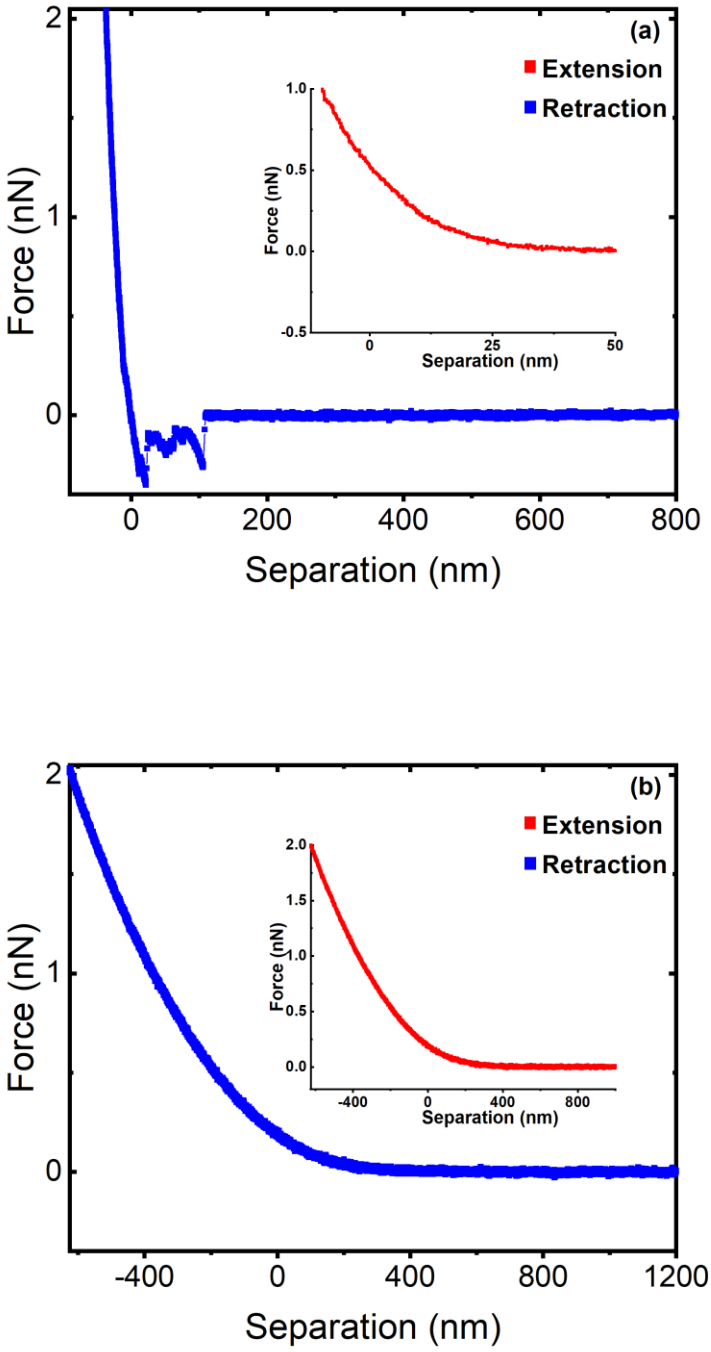

Figure C. 4. Representative retraction force curve and approach force curve (shown in the inset) of a CML colloidal probe on an alginate-fouled ESPA2 membrane at 27 °C. Data were collected in synthetic wastewater supplemented with 20 mg L^{-1} sodium alginate ($t_{contact}$ = 5 s; $F_{trigger}$ = 2 nN; pH 7.4; I = 14.7 mM).

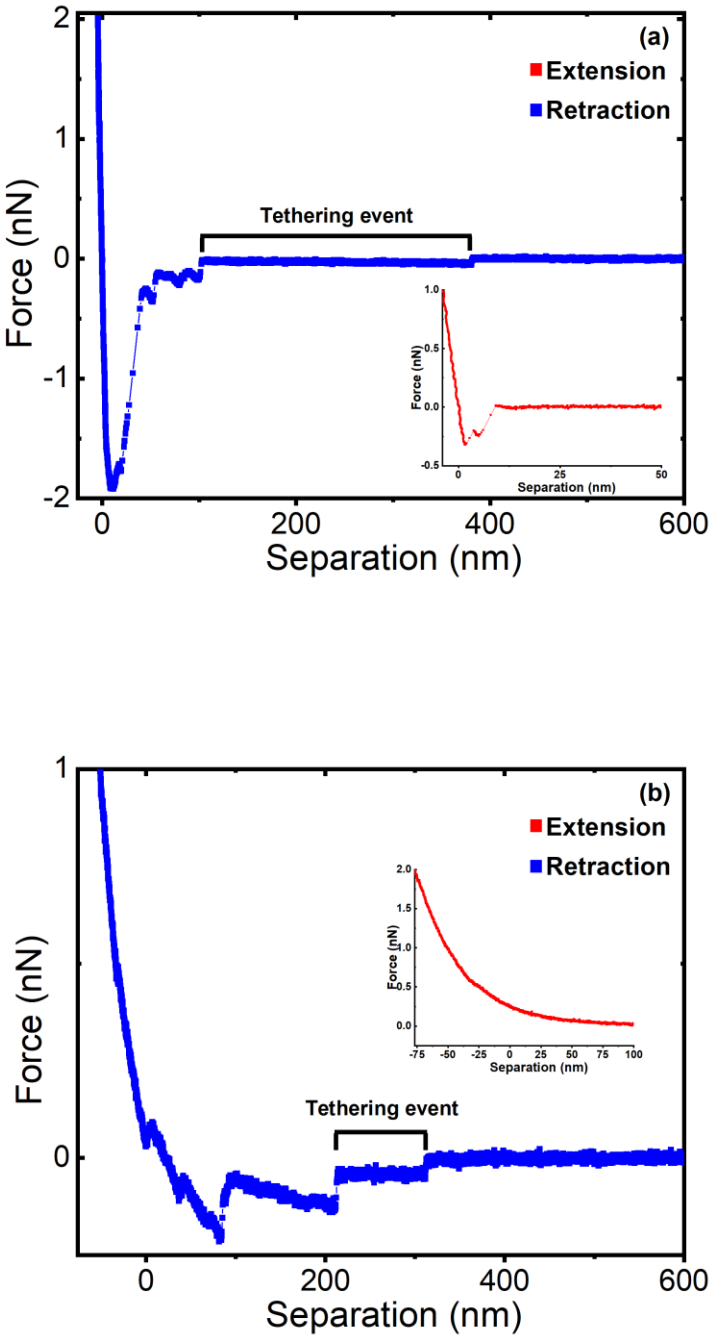

Figure C. 5. Representative retraction force curve exhibiting a tethering event during adhesion of a CML colloidal probe at 27 °C on an ESPA2 (a) pristine and (b) alginate-fouled membrane (approach force curve shown in the inset). Data were collected in synthetic wastewater supplemented with 20 mg L^{-1} sodium alginate ($t_{contact}$ = 5 s; $F_{trigger}$ = 2 nN; pH 7.4; I = 14.7 mM).

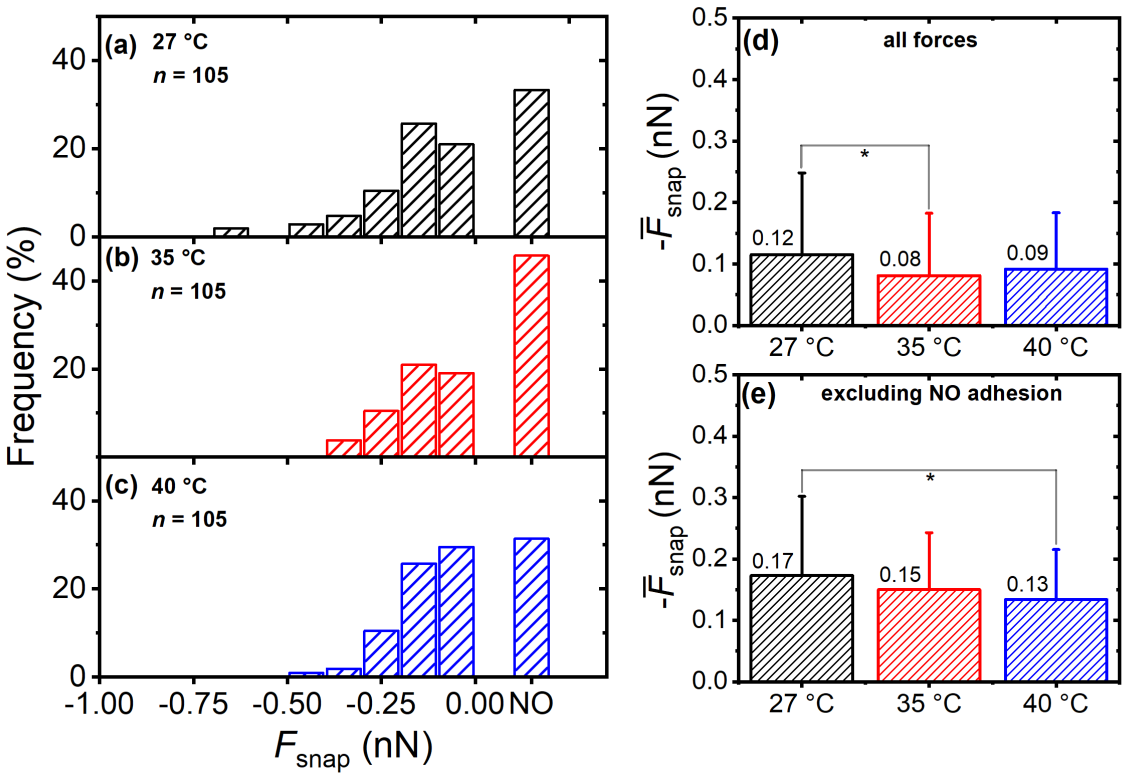

Figure C. 6. (a-c) Distribution of snap-in forces during adhesion of a CML colloidal probe to pristine ESPA2 membranes for each indicated temperature (given in the inset along with the number of force measurements, *n*). Force curves in which snap-in events were not detected are tallied as the "NO" column. (d) Average snap-in force ($\bar{F}_{\text{snap}}$) at each temperature calculated from (a-c) including the non-adhesive (i.e., purely repulsive approach) events as $\bar{F}_{\text{snap}} = 0$ (* denotes statistical significance with $p < 0.05$). (e) Average snap-in force ($\bar{F}_{\text{snap}}$) at each temperature calculated from (a-c) excluding the non-adhesive events (* denotes statistical significance with $p < 0.05$). Error bars denote one standard deviation. Data were collected in synthetic wastewater supplemented with 20 mg L^{-1} sodium alginate (t_{contact} = 5 s; F_{trigger} = 2 nN; pH 7.4; I = 14.7 mM).

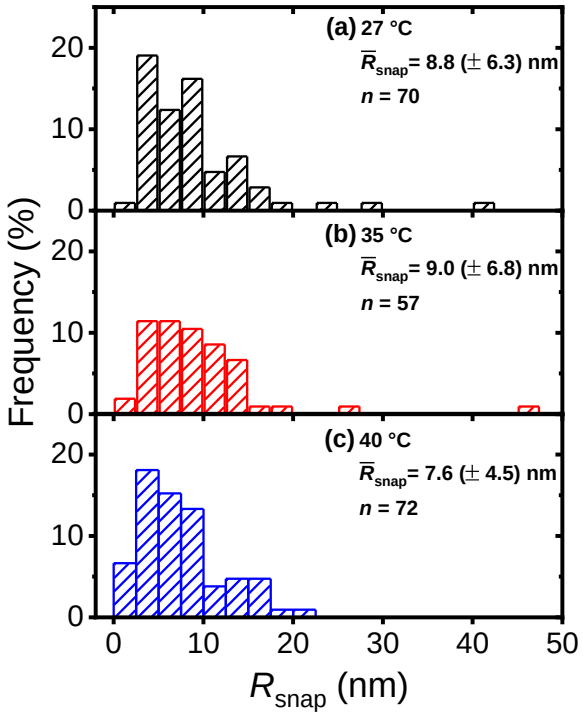

Figure C. 7. Distribution of snap-in distances (R_{snap}) during adhesion of a CML colloidal probe to pristine ESPA2 membranes. Data were collected in synthetic wastewater supplemented with 20 mg L^{-1} sodium alginate at each indicated temperature (given in the inset along with the number of measurements (n) and average snap-in distance $\bar{R}_{snap}$ (± standard deviation)). Other experimental details: $t_{contact}$ = 5 s; $F_{trigger}$ = 2 nN; pH 7.4; I =14.7 mM. Average snap-in distances are similar at all temperatures (p > 0.05 for all pairwise comparisons).

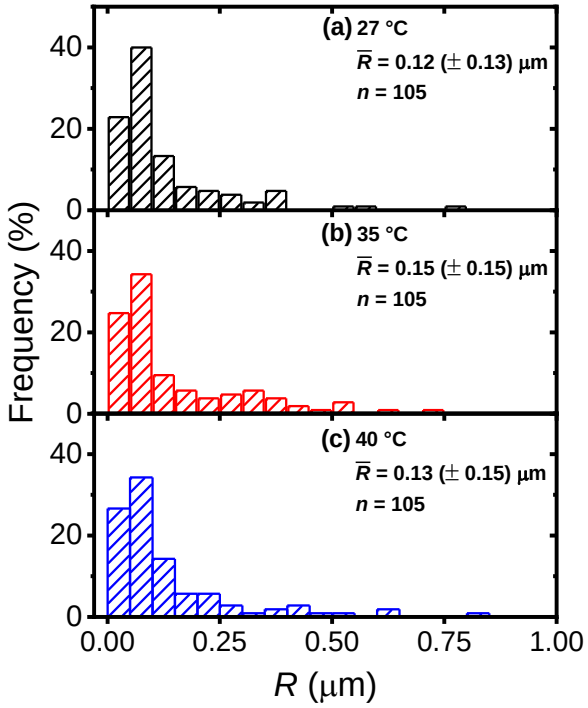

Figure C. 8. Distribution of rupture separations (R) during adhesion of a CML colloidal probe to pristine ESPA2 membranes. Data were collected in synthetic wastewater supplemented with 20 mg L^{-1} sodium alginate at each indicated temperature (given in the inset along with the number of measurements (n) and average rupture separation $\bar{R}$ (± standard deviation)). Other experimental details: $t_{contact}$ = 5 s; $F_{trigger}$ = 2 nN; pH 7.4; I =14.7 mM. Average rupture separations are similar at all temperatures ($p > 0.05$ for all pairwise comparisons).

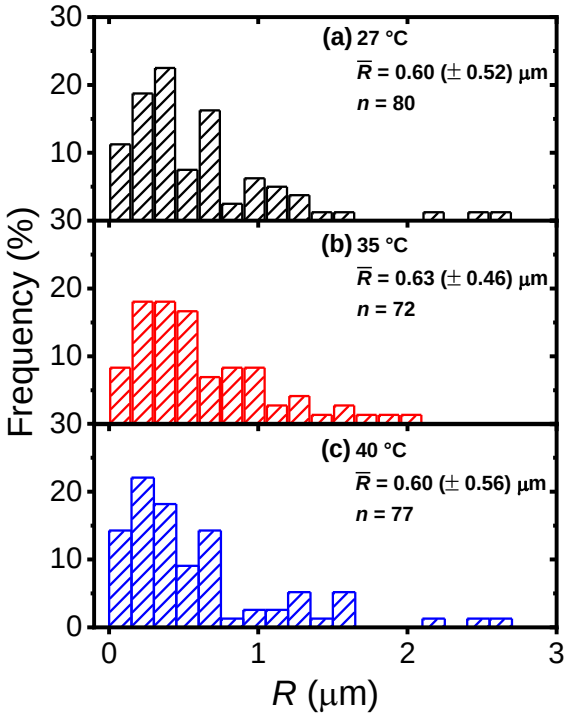

Figure C. 9. Distribution of rupture separations (R) during adhesion of a CML colloidal probe to fouled ESPA2 membranes. Data were collected in synthetic wastewater supplemented with 20 ppm sodium alginate at each indicated temperature (given in the inset along with the number of measurements (n) and average rupture separation $\bar{R}$ (± standard deviation)). Other experimental details: $t_{contact}$ = 5 s; $F_{trigger}$ = 2 nN; pH 7.4; I =14.7 mM. Average rupture separations are similar at all temperatures ($p > 0.05$ for all pairwise comparisons).